UNIVERSITY OF SOUTHAMPTON

FACULTY OF ENGINEERING, SCIENCE & MATHEMATICS

School of Engineering Sciences

Calculation of Steady-State Ship Wave Patterns Using a General Rankine Source Method

by

Özgür Diken

Thesis for the degree of Doctor of Philosophy

December 2006

aileme

UNIVERSITY OF SOUTHAMPTON

ABSTRACT

FACULTY OF ENGINEERING, SCIENCE & MATHEMATICS

SCHOOL OF ENGINEERING SCIENCES

Doctor of Philosophy

CALCULATION OF STEADY-STATE SHIP WAVE PATTERNS USING A GENERAL RANKINE SOURCE METHOD

by Özgür Diken

A general time-domain method is introduced that is capable of solving both steady and unsteady fluid flow around realistic hull forms. An indirect boundary-integral method is formulated by distributing Rankine point sources outside the fluid domain. In the present formulation both the free surface and rigid boundary conditions are applied at instantaneous positions of the boundaries. Boundary surfaces are represented with B-splines in parametric space and collocation points are re-distributed every time step on the boundaries surrounding the fluid domain.

The required computational effort is reduced considerably by using desingularised Rankine point sources and constraining the horizontal movements of the free surface nodes. The numerical simulation may thus be executed on a personal computer in a short amount of time, making this method a realistic alternative to traditional model tests performed in towing tanks.

By way of example, the present method is applied to solve the two-dimensional flow around a circular cylinder submerged in an infinite fluid and the three-dimensional steady flow around a Wigley hull and a Series 60 hull travelling in an initially undisturbed free surface. The sensitivity of the results to various chosen numerical parameters is also investigated.

CONTENTS

ACKNOWLEDGMENTS ..... **- 10 -**

NOMENCLATURE ..... **- 11 -**

1. INTRODUCTION ..... **- 14 -**

1.1 Background ..... - 14 -

1.2 Aims and Structure of Thesis ..... - 20 -

2. GENERAL REVIEW OF RANKINE SOURCE METHODS ..... **- 22 -**

2.1 Linear Rankine Source Methods ..... - 25 -

2.1.1 Linear Steady Methods ..... - 25 -

2.1.2 Linear Unified Methods ..... - 27 -

2.2 Nonlinear Rankine Source Methods ..... - 29 -

2.2.1 Nonlinear Steady Methods ..... - 29 -

2.2.2 Nonlinear Unified Methods ..... - 32 -

2.3 Conclusions ..... - 33 -

3. MATHEMATICAL MODEL ..... **- 36 -**

3.1 Initial Boundary Value Problem ..... - 40 -

3.1.1 Initial Conditions ..... - 40 -

3.1.2 Boundary Conditions ..... - 41 -

4. NUMERICAL SOLUTION ..... **- 44 -**

4.1 Euler Phase ..... - 44 -

4.1.1 The Desingularised Approach ..... - 46 -

4.2 Lagrange Phase ..... - 48 -

4.3 Numerical Scheme ..... - 48 -

4.3.1 Flow Simulation – Euler Phase ..... - 49 -

4.3.2 Flow Simulation – Lagrange Phase ..... - 51 -

5. DISCRETISATION OF BOUNDARY SURFACES ..... - 53 -

5.1 Geometric Description of the Wigley Hull ..... - 53 -

5.2 Free Surface Representation ..... - 54 -

5.3 Mathematical Representation of Arbitrarily-Shaped Hull Surfaces ..... - 58 -

5.4 Geometric Description of the Series 60 Hull ..... - 65 -

6. A SIMPLE APPLICATION OF THE RANKINE SOURCE METHOD ... - 68 -

7. SIMULATION OF THE STEADY FLOW AROUND A WIGLEY HULL ..... - 76 -

7.1 Discretisation of the Body Surface ..... - 76 -

7.2 Discretisation of the Free Surface ..... - 77 -

7.3 Solution of the Linear Equation System ..... - 80 -

7.4 Integration of the Free Surface Boundary Conditions ..... - 83 -

7.5 Sensitivity to Numerical Parameters ..... - 83 -

7.6 Wave Profile along the Wigley Hull ..... - 92 -

7.7 Forces and Moments on the Hull ..... - 97 -

7.8 Sinkage and Trim ..... - 112 -

8. SIMULATION OF THE STEADY FLOW AROUND A SERIES 60 HULL ..... - 114 -

8.1 Discretisation of the Body Surface ..... - 114 -

8.2 Discretisation of the Free Surface ..... - 116 -

8.3 Integration of the Free Surface Boundary Conditions ..... - 118 -

8.4 Sensitivity to Numerical Parameters ..... - 119 -

8.5 Wave-Making Resistance of the Series 60 Hull ..... - 128 -

8.6 Data Smoothing ..... - 141 -

9. CONCLUSIONS AND FUTURE WORK ..... - 145 -

BIBLIOGRAPHY ..... - 150 -

APPENDIX ..... - 165 -

LIST OF TABLES

Table 7.1: CPU times for different grid densities ..... - 82 -
Table 7.2: Comparison of CPU times and accuracy of different solvers ..... - 82 -
Table 7.3: Numerical parameters used for *test-A* ..... - 87 -
Table 7.4: The number of Rankine sources used for *test-A* ..... - 87 -
Table 8.1: Principal dimensions of the Series 60 hull ..... - 115 -
Table 8.2: Numerical parameters used for *test-B* ..... - 122 -
Table 8.3: The number of Rankine sources used for *test-B* ..... - 122 -

LIST OF FIGURES

Figure 2.1: Hull and free surface discretisation for the Rankine panel method ..... - 23 -
Figure 2.2: Hull and free surface discretisation for the desingularised approach .... - 23 -
Figure 2.3: Hull and free surface discretisation for the raised-panel method ..... - 24 -
Figure 3.1: Control volume used for the derivation of the continuity equation in two dimensions ..... - 39 -
Figure 3.2: Hull-fixed coordinate system and the boundary surfaces ..... - 43 -
Figure 4.1: Arrangement of the Rankine sources (•) and collocation points (0) ..... - 47 -
Figure 5.1: A B-spline surface (Q) and its defining polygon net ($B_{i,j}$) ..... - 57 -
Figure 5.2: The input yacht hull for the discretisation algorithm ..... - 60 -
Figure 5.3: The input NPL hull for the discretisation algorithm ..... - 60 -
Figure 5.4: The output of the discretisation algorithm for the yacht hull ..... - 61 -
Figure 5.5: The output of the discretisation algorithm for the NPL hull ..... - 61 -
Figure 5.6: The input Wigley hull for the discretisation algorithm ..... - 62 -
Figure 5.7: The output of the discretisation algorithm for the Wigley hull ..... - 62 -
Figure 5.8: Comparison of offset values for the Wigley hull – input stations defined by 5 points ..... - 63 -
Figure 5.9: Comparison of offset values for the Wigley hull – input stations defined by 13 points ..... - 63 -
Figure 5.10: A sample cross-section ..... - 64 -
Figure 5.11: A rendered image of the Series 60 hull - $C_B = 0.60$ ..... - 67 -
Figure 5.12: Discretisation of the Series 60 hull - $C_B = 0.60$ ..... - 67 -
Figure 6.1: Two-dimensional flow around a circular cylinder ..... - 71 -
Figure 6.2: Pressure distribution over the cylinder for 10 point sources - $l_d = 0.2r$ - 71 -
Figure 6.3: Pressure distribution over the cylinder for 25 point sources - $l_d = 0.2r$ - 72 -
Figure 6.4: Pressure distribution over the cylinder for 50 point sources - $l_d = 0.2r$ - 72 -
Figure 6.5: Pressure distribution over the cylinder for 100 point sources - $l_d = 0.2r$ - 73 -

Figure 6.6: Pressure distribution over the cylinder for 10 point sources - $l_d = 0.4r$ - 73 -

Figure 6.7: Pressure distribution over the cylinder for 25 point sources - $l_d = 0.4r$ - 74 -

Figure 6.8: Pressure distribution over the cylinder for 50 point sources - $l_d = 0.4r$ - 74 -

Figure 6.9: Pressure distribution over the cylinder for 100 point sources - $l_d = 0.4r$ - 75 -

Figure 6.10: Comparison of the theory with the time-domain solution for varying desingularisation distances ..... - 75 -

Figure 7.1: Computational grid for the Wigley hull ..... - 79 -

Figure 7.2: The effect of hull desingularisation distance on the numerical solution – control point on the hull surface ..... - 87 -

Figure 7.3: The effect of free surface desingularisation distance on the numerical solution – control point on the hull surface ..... - 88 -

Figure 7.4: The effect of time-step size on the numerical solution – control point on the hull surface ..... - 88 -

Figure 7.5: The effect of hull acceleration parameter on the numerical solution – control point on the hull surface ..... - 89 -

Figure 7.6: The effect of hull desingularisation distance on the numerical solution – control point on the free surface ..... - 89 -

Figure 7.7: The effect of free surface desingularisation distance on the numerical solution – control point on the free surface ..... - 90 -

Figure 7.8: The effect of time-step size on the numerical solution – control point on the free surface ..... - 90 -

Figure 7.9: The effect of hull acceleration parameter on the numerical solution – control point on the free surface ..... - 91 -

Figure 7.10: Wave profile along the Wigley hull - $F_n = 0.25$ ..... - 94 -

Figure 7.11: Wave profile along the Wigley hull - $F_n = 0.267$ ..... - 94 -

Figure 7.12: Wave profile along the Wigley hull - $F_n = 0.289$ ..... - 95 -

Figure 7.13: Wave profile along the Wigley hull - $F_n = 0.316$ ..... - 95 -

Figure 7.14: Wave profile along the Wigley hull for the finer mesh - $F_n = 0.25$, $\Delta t = 0.01$, $\alpha = 0.11$ ..... - 96 -
Figure 7.15: Time histories of the wave elevation of a control point for two different mesh sizes - $F_n = 0.25$ ..... - 96 -
Figure 7.16: Components of the wave resistance coefficient - $F_n = 0.25$, $d_h = 0.8$, $d_{fs} = 1.0$, $\Delta t = 0.02$, $\alpha = 0.11$, 462 Rankine sources ..... - 102 -
Figure 7.17: Components of the wave resistance coefficient - $F_n = 0.25$, $d_h = 0.8$, $d_{fs} = 1.0$, $\Delta t = 0.01$, $\alpha = 0.11$, 462 Rankine sources ..... - 102 -
Figure 7.18: Components of the wave resistance coefficient - $F_n = 0.25$, $d_h = 0.2$, $d_{fs} = 0.8$, $\Delta t = 0.04$, $\alpha = 0.9$, 572 Rankine sources ..... - 103 -
Figure 7.19: Components of the wave resistance coefficient - $F_n = 0.25$, $d_h = 0.2$, $d_{fs} = 0.8$, $\Delta t = 0.04$, $\alpha = 0.9$, 902 Rankine sources ..... - 103 -
Figure 7.20: Grid-dependence of the numerical predictions for wave-making resistance of the Wigley hull at $F_n = 0.25$ ..... - 104 -
Figure 7.21: Components of the wave resistance coefficient - $F_n = 0.267$, $d_h = 0.8$, $d_{fs} = 1.0$, $\Delta t = 0.02$, $\alpha = 0.11$, 462 Rankine sources ..... - 104 -
Figure 7.22: Components of the wave resistance coefficient - $F_n = 0.267$, $d_h = 0.8$, $d_{fs} = 1.0$, $\Delta t = 0.01$, $\alpha = 0.11$, 462 Rankine sources ..... - 105 -
Figure 7.23: Components of the wave resistance coefficient - $F_n = 0.267$, $d_h = 0.2$, $d_{fs} = 0.8$, $\Delta t = 0.04$, $\alpha = 0.9$, 572 Rankine sources ..... - 105 -
Figure 7.24: Grid-dependence of the numerical predictions for wave-making resistance of the Wigley hull at $F_n = 0.267$ ..... - 106 -
Figure 7.25: Components of the wave resistance coefficient - $F_n = 0.289$, $d_h = 0.8$, $d_{fs} = 1.0$, $\Delta t = 0.02$, $\alpha = 0.11$, 462 Rankine sources ..... - 106 -

Figure 7.26: Components of the wave resistance coefficient - $F_n = 0.289$, $d_h = 0.8$, $d_{fs} = 1.0$, $\Delta t = 0.01$, $\alpha = 0.11$, 462 Rankine sources ..... - 107 -

Figure 7.27: Components of the wave resistance coefficient - $F_n = 0.289$, $d_h = 0.2$, $d_{fs} = 0.8$, $\Delta t = 0.04$, $\alpha = 0.9$, 572 Rankine sources ..... - 107 -

Figure 7.28: Components of the wave resistance coefficient - $F_n = 0.289$, $d_h = 0.2$, $d_{fs} = 0.5$, $\Delta t = 0.04$, $\alpha = 0.9$, 902 Rankine sources ..... - 108 -

Figure 7.29: Grid-dependence of the numerical predictions for wave-making resistance of the Wigley hull at $F_n = 0.289$ ..... - 108 -

Figure 7.30: Components of the wave resistance coefficient - $F_n = 0.316$, $d_h = 0.8$, $d_{fs} = 1.0$, $\Delta t = 0.02$, $\alpha = 0.11$, 462 Rankine sources ..... - 109 -

Figure 7.31: Components of the wave resistance coefficient - $F_n = 0.316$, $d_h = 0.8$, $d_{fs} = 1.0$, $\Delta t = 0.01$, $\alpha = 0.11$, 462 Rankine sources ..... - 109 -

Figure 7.32: Components of the wave resistance coefficient - $F_n = 0.316$, $d_h = 0.2$, $d_{fs} = 1.0$, $\Delta t = 0.04$, $\alpha = 0.9$, 572 Rankine sources ..... - 110 -

Figure 7.33: Components of the wave resistance coefficient - $F_n = 0.316$, $d_h = 0.2$, $d_{fs} = 1.0$, $\Delta t = 0.04$, $\alpha = 0.9$, 902 Rankine sources ..... - 110 -

Figure 7.34: Grid-dependence of the numerical predictions for wave-making resistance of the Wigley hull at $F_n = 0.316$ ..... - 111 -

Figure 7.35: Wave-making resistance of the Wigley hull ..... - 111 -

Figure 7.36: Wave resistance coefficients for the restrained and unrestrained Wigley hull - $d_h = 0.2$, $d_{fs} = 0.8$, $\Delta t = 0.02$, $\alpha = 0.11$, 462 Rankine sources ..... - 113 -

Figure 8.1: Computational grid for the Series 60 hull ..... - 117 -

Figure 8.2: The effect of hull desingularisation distance on the numerical solution – control points on the hull surface ..... - 122 -

Figure 8.3: The effect of free surface desingularisation distance on the numerical solution – control points on the hull surface ..... - 123 -

Figure 8.4: The effect of time-step size on the numerical solution – control points on the hull surface ..... - 123 -
Figure 8.5: The effect of hull acceleration parameter on the numerical solution – control points on the hull surface ..... - 124 -
Figure: 8.6: The effect of hull desingularisation distance on the numerical solution – control points on the free surface ..... - 124 -
Figure 8.7: The effect of free surface desingularisation distance on the numerical solution – control points on the free surface ..... - 125 -
Figure 8.8: The effect of time-step size on the numerical solution – control points on the free surface ..... - 125 -
Figure 8.9: The effect of hull acceleration parameter on the numerical solution – control points on the free surface ..... - 126 -
Figure 8.10: The effect of constant influence coefficient matrix on the numerical solution ..... - 126 -
Figure 8.11: The effect of the cubic spline scheme on the numerical solution ..... - 127 -
Figure 8.12: Time history of the wave resistance coefficient for different free surface meshes - $F_n = 0.25$ ..... - 132 -
Figure 8.13: Time history of the wave resistance coefficient for different free surface meshes - $F_n = 0.28$ ..... - 132 -
Figure 8.14: Time history of the wave resistance coefficient for different free surface meshes - $F_n = 0.30$ ..... - 133 -
Figure 8.15: Time history of the wave resistance coefficient for different free surface meshes - $F_n = 0.316$ ..... - 133 -
Figure 8.16: Time history of the wave resistance coefficient for different free surface meshes - $F_n = 0.32$ ..... - 134 -
Figure 8.17: Time history of the wave resistance coefficient for different free surface meshes - $F_n = 0.34$ ..... - 134 -
Figure 8.18: Time history of the wave resistance coefficient for different free surface meshes - $F_n = 0.35$ ..... - 135 -

Figure 8.19: Time history of the wave resistance coefficient for varying hull desingularisation distance - $F_n = 0.316$ ..... - 135 -

Figure 8.20: Time history of the wave resistance coefficient for varying free surface desingularisation distance - $F_n = 0.316$ ..... - 136 -

Figure 8.21: Time history of the wave resistance coefficient for varying time-step size - $F_n = 0.316$ ..... - 136 -

Figure 8.22: Time history of the wave resistance coefficient for varying hull acceleration parameter - $F_n = 0.316$ ..... - 137 -

Figure 8.23: Time history of the wave resistance coefficient for different hull acceleration functions - $F_n = 0.316$ ..... - 137 -

Figure 8.24: Time history of the wave resistance coefficient for varying side boundary position - $F_n = 0.316$ ..... - 138 -

Figure 8.25: Time history of the wave resistance coefficient for varying downstream boundary position - $F_n = 0.316$ ..... - 138 -

Figure 8.26: Time history of the wave resistance coefficient for varying upstream boundary position - $F_n = 0.316$ ..... - 139 -

Figure 8.27: Comparison of computed and measured wave resistance coefficients for Series 60 hull with $C_B = 0.60$ ..... - 140 -

Figure 8.28: Wave resistance predictions for the Series 60 hull - $C_B = 0.60$ ..... - 140 -

Figure 8.29: The effect of the data smoothing procedure on individual control points - $d_{fs} = 0.1$ ..... - 143 -

Figure 8.30: The effect of the data smoothing procedure on the wave resistance coefficient predictions - $d_{fs} = 0.1$ ..... - 143 -

Figure 8.31: The effect of the data smoothing procedure on individual control points - $d_h = 0.003$ ..... - 144 -

Figure 8.32: The effect of the data smoothing procedure on the wave resistance coefficient predictions - $d_h = 0.003$ ..... - 144 -

ACKNOWLEDGMENTS

I would like to thank all of the members of Ship Science for their help throughout my studies.

In particular, I wish to express my gratitude to Dr. D. A. Hudson, Professor P. Temarel and Dr. Shuangxing Du for their support during my stay in Southampton and their long distance assistance while I was doing the final writing up of this thesis in İstanbul. I am indebted to my supervisor Dr. Hudson for allowing me to work independently and yet being there when I need his guidance and advice.

My thanks are also due to Dr. O. Belik of Istanbul Technical University for being an ideal role model as an academician.

I am exceptionally grateful to Deniz for her endless support and encouragement. As if her mere presence was not enough, she supported me by all means possible.

Last, but certainly not least, my thanks are directed to Mum, Dad and my little sister for always being there for me in my toughest and happiest times.

NOMENCLATURE

A	Area
A_{WL}	Waterplane area
B	Breadth of the hull
$B_{i,j}$	Vertices of the defining polygon net for the B-spline surface
C_B	Block coefficient
C_p	Surface pressure coefficient
C_w	Wave-making resistance coefficient
d_{fs}	Desingularisation coefficient for the free surface
d_h	Desingularisation coefficient for the hull
D	Depth of the hull
f	Acceleration due to a volumetric force
F_n	Froude number
g	Acceleration due to gravity force
G	Green's function
I_{WL}	Moment of inertia
l_d	Desingularisation distance for the circular cylinder
l_{fs}	Desingularisation distance for the free surface
l_h	Desingularisation distance for the hull
L	Length of the hull
M	Total number of control points on the free surface
$\vec{n} = (n_1, n_2, n_3)$	Unit normal vector
N	Total number of control points in the fluid domain
$\vec{N}$	Normal vector
p	Fluid pressure

P_a	Atmospheric pressure
$P_{i,3}$	B-spline basis function in the β direction
Q	B-spline surface
r	Radius of the circular cylinder
$R_{j,3}$	B-spline basis function in the χ direction
s_c	Set of parameters in the β direction
S	Integration surface
S_B	Bottom boundary
S_c	Knot vector in the β direction
S_F	Free surface boundary
S_H	Hull boundary
S_T	Truncated boundary
t	Time
t_d	Set of parameters in the χ direction
T	Draught of the hull
T_d	Knot vector in the χ direction
u	Velocity component in the x direction
U	Ship speed
U_s	Steady forward speed of the hull
v	Velocity component in the y direction
$\vec{v}$	Prescribed velocity of the free surface nodes
$\vec{v}_h$	Velocity of a node on the hull surface
$\vec{V}_B$	Velocity of the bottom boundary
w	Velocity component in the z direction
$\vec{x} = (x, y, z)$	Displacement vector
x_{WL}	Centre of the waterplane

α	Acceleration parameter
β	Parametric value
$\vec{\gamma}_r$	Rotational displacement of the hull
$\vec{\gamma}_t$	Translational displacement of the hull
$\vec{\delta}_h$	Oscillatory displacement of the hull
η	Free surface elevation
θ	Polar distance of a control point from the coordinate axes
μ	Fluid viscosity
$\vec{\xi}$	Displacement vector for the source points
ρ	Fluid density
σ	Source strength
ϕ	Perturbation potential
Φ	Total velocity potential
χ	Parametric value

1. INTRODUCTION

1.1 Background

The physical processes that describe the behaviour of a ship in a seaway are extremely complex, yet have to be predicted as accurately as possible to meet specific design criteria such as speed, stability, seakeeping characteristics, manoeuvrability etc. For instance, in order to comply with a given speed constraint, the power requirement of the ship, which is directly related to its fuel consumption and hence its transport economy, has to be estimated beforehand with a certain precision. In practice, the hydrodynamic performance of a ship is investigated separately in still water and in waves. The former addresses the power requirement of a ship in calm water, which is generally lower than the total required power in a natural seaway.

Traditionally, hydrodynamic analyses of ship hulls are carried out in towing tanks on scaled models. Tank-testing is a costly process in terms of the required time and testing expenses. As the hull is optimised during the testing stage, several modifications have to be done on the scaled model, which often leads to reconstruction of the model and consequently the testing process is repeated a number of times.

An alternative to tank-testing, and the subject of this study, is the numerical simulation of a towing tank to evaluate hydrodynamic characteristics of ship hulls travelling in an otherwise undisturbed free surface. Several commercial codes are currently available that are capable of solving the three-dimensional nonlinear wave resistance and/or seakeeping problem (see, for example, Bertram (2000), Raven (1996), Larsson et al. (1989), Jensen et al. (1986)). However, due to the complexity of the physical problem and hence the high computational time, numerical methods can be as expensive as traditional model tests. The ones that depict the physical problem more accurately

generally require several hours of CPU time even on supercomputers, which restricts their use as a practical design tool.

A compromise between accuracy and numerical efficiency is crucial in order to establish a hydrodynamic analysis algorithm that can be a real alternative to traditional model tests performed in towing tanks. The chosen mathematical model has to be simple enough to render its solution tractable, yet represent the physical phenomenon as accurately as possible.

Several mathematical models are available that can be implemented to simulate fluid flow around ship hulls. One of these is the potential flow theory which has been used almost exclusively over the years for the solution of the steady (and unsteady) flow problem.

Potential flow theory assumes the fluid to be inviscid, hence disregards the effect of the ship's boundary layer and wake on the wave pattern. In reality, the fluid flow around a ship hull depends both on the effects of a gravitational field and the viscosity of the fluid. That is to say, viscous effects i.e. friction, formation (and possibly separation) of the boundary layer around a ship hull and the excitation of a wave pattern are all functions of the viscosity of the fluid and the gravitational forces. However, in model testing and numerical simulations, following Froude's (1868) hypothesis, the total fluid flow is divided into its components which are assumed to be independent of each other (see, for example, Brizzolara et al. (1998)). It should be reminded that methods that can account for interactions between the viscous and gravitational forces exist and are discussed at the end of this section.

The separation of the total fluid flow into its viscous and gravitational components which satisfy different scaling rules allows us to use simpler models (such as those based on potential flow) for individual components.

Michell's (1898) work on the wave-making resistance of a thin ship-shaped body is generally accepted as the starting point of computational methods. Strictly speaking, Michell established an analytical relationship between the wave-making resistance of a ship travelling in an inviscid fluid and its hull form based on perturbation analysis.

In perturbation analyses, a suitable perturbation parameter is defined and the solution is expanded about this parameter. For instance, the perturbation parameter in Michell's (Michell (1898)) thin-ship theory is the beam to length ratio and as this value approaches zero the free surface disturbance vanishes. Other possibilities are to use the draught to length ratio as the perturbation parameter, as in flat-ship theory (e.g. Tuck (1975)), or the Froude number (F_n) as in slow-ship theory (e.g. Newman (1976)) etc.

In thin-ship theory, the chosen perturbation parameter allows the linearisation of the free surface boundary conditions. The body boundary condition is transferred to the centre-plane of the ship (whereas in flat-ship theory the body boundary condition is imposed on the ship's waterplane). The integral expression given by Michell that yields the wave resistance of a hull is a first-order approximation (Peters and Stoker (1957)) and includes a function which is used to incorporate the hull geometry into the formulation. The hull geometry can either be defined analytically (see, for example, Guilloton (1951)) or approximated by a number of singularities positioned on the ship's centre-plane section as in Havelock (1925). For an extensive discussion of theoretical methods based on thin-ship theory see, for example, Lunde (1951).

Owing to the linearity of Laplace's equation (3.6), in potential flow theory, it is possible to combine elementary solutions to solve an otherwise complex problem. For this reason, singularity-distribution methods hold an important place in the development of numerical hydrodynamics. A boundary value problem can be obtained by placing fundamental singularities along the boundary surfaces. The boundary value problem is then formulated into a boundary integral problem by applying Green's second identity

to the velocity potential and using an appropriate Green's function (see, for example, Noblesse (1981)).

Numerical potential flow methods differ mainly in the chosen Green's function and hence the singularities used to satisfy Laplace's equation and the appropriate boundary conditions. The wave-source potential (see Havelock (1932)) that has been widely used over the years in ship-wave resistance calculations as a fundamental singularity is named after Kelvin (1887), who studied the characteristic patterns of transverse and diverging waves induced by a pressure point.

Kelvin sources inherently satisfy the far-field radiation condition (see equation 3.17) and a linear free surface boundary condition (also known as the Kelvin free surface condition) that is implied at the location of the undisturbed free surface. The so-called Neumann-Kelvin theory (see, for example, Baar (1987)) makes use of these Kelvin sources to formulate the wave resistance problem. The sources are distributed on the actual hull surface without imposing any restrictions on the hull geometry as opposed to the thin-ship theory in which the body surface is projected onto its centre-plane section. However, since Kelvin sources are used in the formulation, a linear free surface condition is satisfied which is imposed on the calm water surface and hence the free surface disturbance is assumed small. That is to say, the hull boundary condition is satisfied to a higher order of approximation than the free surface condition. Therefore, the Neumann-Kelvin theory is in essence inconsistent. This inconsistency is of little practical importance as demonstrated by Baar and Price (1988), whose numerical predictions based on Neumann-Kelvin theory are in qualitative agreement with experimental measurements for a variety of hull forms. However, the results are less satisfactory for full hull forms due to neglected nonlinear free surface effects.

Another alternative for the prediction of the flow around a ship hull in steady forward motion is the slender-ship theory (see, for example, Noblesse (1983)) in which the perturbation parameters are the transverse dimensions of the ship hull. It is a singular

perturbation problem as the hull reduces to a line segment in the asymptotic limit of the perturbation parameter. Similar to the Neumann-Kelvin problem, the body boundary condition is satisfied on the mean hull surface and once again a linear free surface condition is imposed on the undisturbed free surface.

Although the slender-ship theory has been successful in the unsteady ship motion problem, the same success has not been achieved in its steady counterpart. The failure of the slender-ship theory in ship-wave resistance predictions mostly lies in its foundations. The wave resistance of a hull largely depends on the difference between the pressure forces acting on the fore and aft sections of the hull. However, the slender-body assumptions are violated at the ends of the hull and this leads to poor prediction of the wave resistance. See Ogilvie (1977) for further details.

Naturally, one can also assume that the free surface disturbance vanishes as the Froude number approaches zero. In fact, that is the course of action followed in slow-ship perturbation schemes. In the limit of zero Froude number, the fluid flow resembles the flow around a double-body in a boundless fluid. Hence, slow-ship schemes are also known as double-body methods (see chapter 2 for a discussion on double-body methods).

The slow-ship linearisation results in spatially varying coefficients in the free surface boundary conditions (Raven (1996)). Consequently, it is not possible to satisfy a linear free surface condition by only distributing Kelvin sources over the hull surface. For that reason, in double-body methods, the simpler Rankine source Green's function is adopted which does not satisfy the body and the free surface boundary conditions. Accordingly, both the hull and the free surface have to be discretised.

In the discussion above, all methods that are cited linearise the boundary conditions in some sense. Generally speaking, linearisation of the boundary conditions may include simplifying the hull geometry, neglecting nonlinear terms in the boundary conditions

and transferring the conditions that are valid on the instantaneous position of the water surface to the mean position of the free surface (e.g. calm water surface) commonly by means of Taylor series expansions. An important advantage of using the Rankine source Green's function in place of Kelvin sources is the possibility of satisfying an exact nonlinear free surface boundary condition rather than the linear Kelvin condition (e.g. Wyatt (2000)).

It is also possible to incorporate the viscosity of the fluid into the mathematical formulation as in RANS (Reynolds-Averaged Navier-Stokes) and LES (Large-Eddy Simulation) solvers (see, for example, Miyata (1996), Dommermuth et al. (1998), Larsson et al. (1998)). Unlike the boundary element methods (BEMs) that are used for the solution of potential flow; RANS and LES solvers discretise not only the boundaries surrounding the fluid domain but the whole fluid domain, which increases the order of the problem by one and results in a computationally intensive formulation.

Although RANS and LES solvers depict the real physical problem better than potential flow methods, it is debatable whether a viscous fluid formulation is a necessity and the ultimate tool for engineering design purposes due to its high computing power and time requirements. The viscous effects are confined to a wake region behind the hull and a thin boundary layer around the hull as a result of the high Reynolds numbers involved in ship flows (Bulgarelli et al. (2003)). This indicates that a viscous flow model will yield far better results for local flow characteristics. However, for global flow characteristics, its superiority is questionable in terms of practicality (Scorpio (1997)). One may increase the computational efficiency of a viscous fluid formulation by treating the free surface as a rigid plane and consequently neglecting wave-making on the free surface, similar to the double-body method used in potential flow codes. Then again, this leads to a compromise between a viscous flow formulation which disregards the effect of the wave pattern on the solution and an inviscid one that can capture the nonlinearities (other than the effect of viscosity) on the free surface with the help of

appropriate boundary conditions. In this study, inviscid (potential flow) theory is favoured, as it suits better the specific aims of this thesis.

1.2 Aims and Structure of Thesis

Potential flow theory has been implemented in many different ways over the years as summarised above. A vast amount of information is available in the literature related to potential flow theory. See, for example, Inui (1962), Gadd (1968), Wehausen (1973), and Baar (1987) for an introduction to wave resistance theory including experimental and analytical approaches and comprehensive reviews of numerical methods based on potential flow theory. The emphasis in this work will be on a particular implementation of this theory, namely the Rankine source method.

The Rankine source method first appeared in the field of hydrodynamics in the late seventies (see, for example, Gadd (1976)). However, due to the limited computational power at that time, it was not accepted as a practical design tool until the last decade. Since then, it has been widely used for hydrodynamic analysis of floating bodies. A brief history and the various implementations of the Rankine source method are discussed in chapter 2 of the thesis.

The aim of this thesis is to introduce a unified method; unified in the sense that it can solve the three-dimensional nonlinear steady flow around an arbitrarily-shaped ship hull to investigate its behaviour in calm water and that it can be extended for the solution of unsteady fluid flow problems. The mathematical model that represents this continuous physical problem is discussed in chapter 3.

Since an analytical solution is not possible for this complex mathematical model, a discrete representation of the continuous physical problem is required to obtain a numerical solution. A robust and fast time-domain formulation, which is presented in

chapter 4, is chosen for the purpose of numerical simulation. The present method can be used to evaluate the steady-state ship wave pattern of an arbitrarily-shaped ship hull in a matter of two or three hours on a standalone workstation. While trying to achieve an acceptable accuracy, one of the primary concerns of this study is to simplify the problem in order to perform the simulations on a personal computer in a relatively short amount of CPU time. In recent literature, similar class of methods is limited to simple unrealistic geometries without detailed results due to high computing times. In this study, an extensive amount of results are presented for complex body geometries. A novel way of fixing the free surface nodes to the horizontal plane helped to lower the computational time considerably. This procedure has not been applied to three-dimensional geometries with forward motion before.

By way of example, the present method is applied to solve the two-dimensional flow around a circular cylinder submerged in an infinite fluid and the three-dimensional steady flow around a Wigley hull and a Series 60 hull travelling in an initially undisturbed free surface. A grid generation algorithm that is introduced to represent hull surfaces of arbitrary shapes is given in chapter 5 of the thesis. The numerical results obtained from the simulations are discussed in detail in chapters 6, 7 and 8 for the circular cylinder, Wigley hull and the Series 60 hull respectively. A detailed numerical sensitivity analysis is carried out for each ship hull to investigate the effects of variations in numerical parameters on the accuracy of the solution. Finally, in chapter 9, the findings of this study are summarised together with the original ideas introduced to the field of numerical hydrodynamics and a discussion on possible future work on the subject.

2. GENERAL REVIEW OF RANKINE SOURCE METHODS

Rankine source methods are categorised into three groups in this text according to the way the hull and the free surface are discretised. These are *Rankine panel method*, the *desingularised approach* and *raised-panel method* (see figures 2.1 to 2.3).

In a Rankine panel method, the boundaries surrounding the fluid domain are discretised with panels as the name suggests. In a first-order Rankine panel method, the boundaries are generally discretised with quadrilateral flat panels and the source strengths are kept constant over a panel. It is also possible to use higher-order panels and source distributions e.g. panels with quadratic shapes that have linearly varying source strengths (see figure 2.1).

The integration and control surfaces coincide in Rankine panel methods resulting in singular kernels, which can be avoided by moving the integration surface outside the fluid domain. In fact, that is the procedure followed in the desingularised approach. Another feature of the desingularised approach is that the boundaries are discretised with nodes instead of panels. Rankine point sources are placed around these nodes and consequently the surface integrals are replaced with simple summations (see figure 2.2).

The raised-panel method is a combination of the other two methods. Like the Rankine panel method, panels are used for discretisation of the boundary surfaces. However, the free surface source panels are placed above the free surface boundary; whereas the hull source panels are on the actual body surface (see figure 2.3).

For all the Rankine source methods mentioned above, collocation points, where the boundary conditions are imposed, are on the true boundaries.

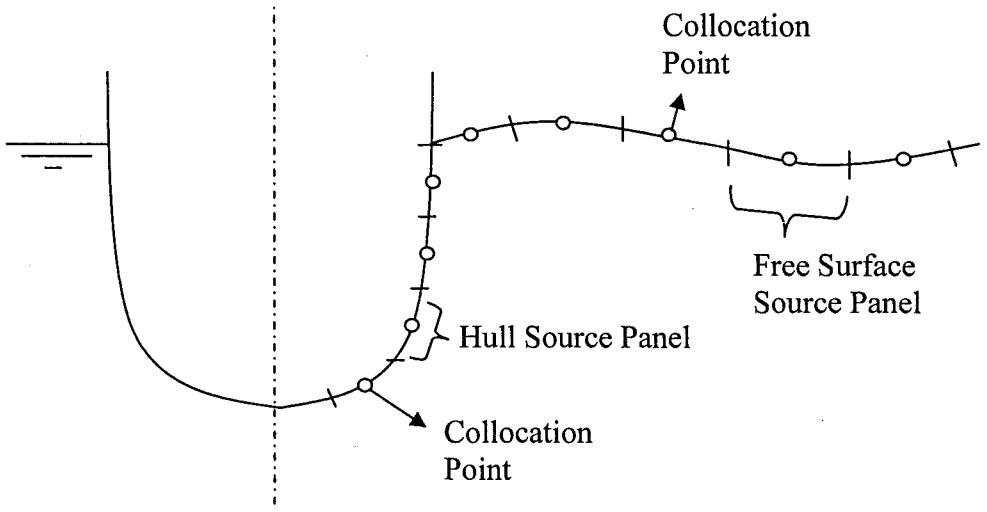

Figure 2.1: Hull and free surface discretisation for the Rankine panel method.

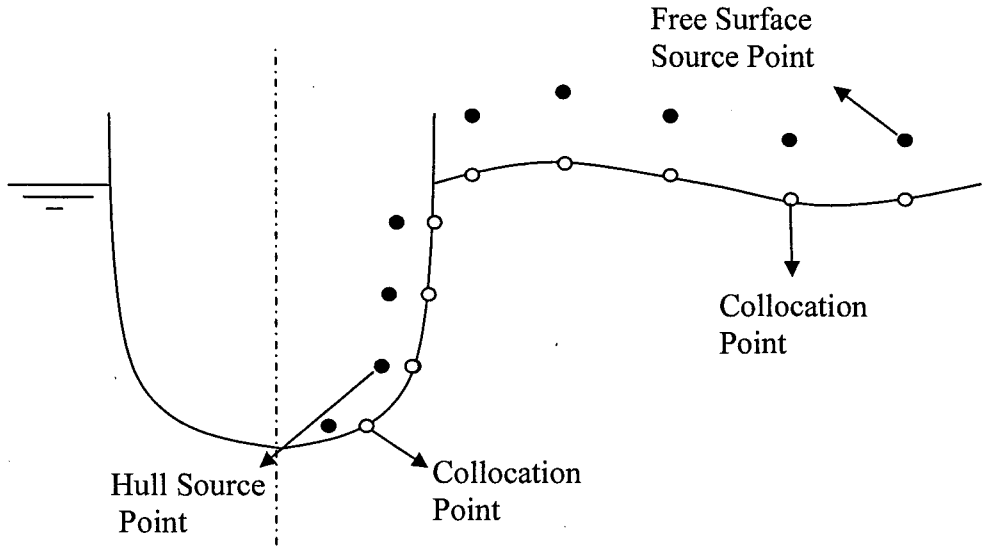

Figure 2.2: Hull and free surface discretisation for the desingularised approach.

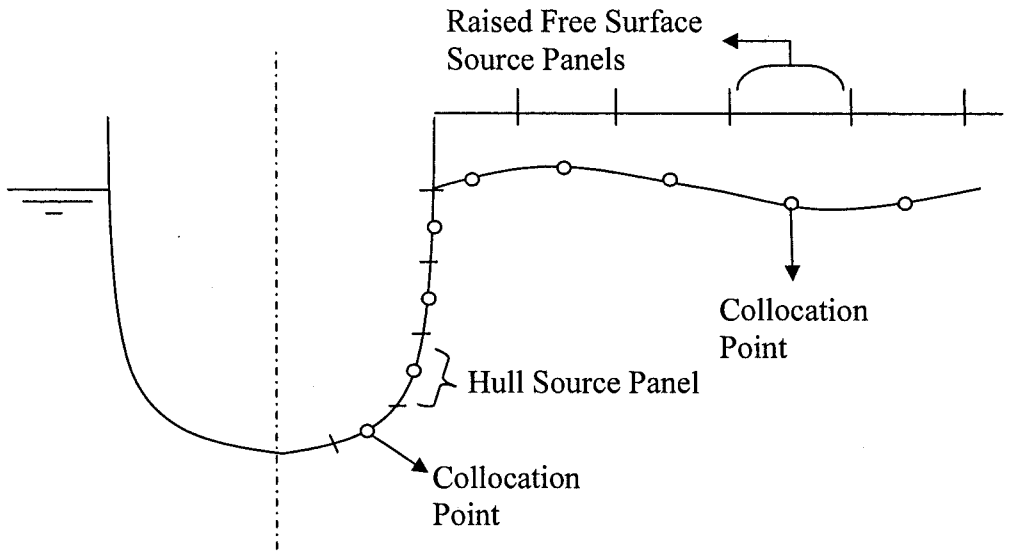

Figure 2.3: Hull and free surface discretisation for the raised-panel method.

2.1 Linear Rankine Source Methods

When the Rankine source method was introduced for the solution of the ship-wave resistance and seakeeping problem, computational restrictions forced the researchers to linearise the boundary conditions; mainly the free surface conditions, which are highly nonlinear (see, for example, Nakos (1990)). A widely used technique for this purpose is the slow-ship linearisation.

The slow-ship linearisation is based upon simplification with respect to the flow around a hull at zero Froude number, the so-called double-body flow. In a double-body method, the free surface acts as a rigid plane of symmetry and the underwater part of the hull is reflected about the calm water plane. Both the original wetted hull and its reflected image are discretised. The slow-ship linearisation results in a combined nonlinear free surface condition that has to be imposed on the instantaneous free surface. Therefore, further simplifications are necessary. For an extensive discussion on linearisation schemes, see Raven (1990).

2.1.1 Linear Steady Methods

Hydrodynamic optimisation of a ship hull is the main objective of the steady flow analysis and is a tool that is used to minimise the wave-making resistance of ships.

In a towing tank environment, resistance measurements are generally carried out in calm water to find out the required power to propel a ship at a particular speed. The effect of sea-state is then taken into account as an added resistance in waves (Lloyd (1998)). Steady Rankine source methods are used to determine the time-independent (i.e. steady) wave pattern of hulls travelling in an initially undisturbed free surface, analogous to towing tank experiments for resistance.

Gadd (1976) was the first to adopt the Rankine panel method for the solution of the steady wave resistance problem. Despite the computational restrictions of the time reasonable results are obtained for full hull forms. Although some of the nonlinearities are captured on the free surface with a combined free surface condition, the free surface boundary conditions are imposed on the still water plane. Thus, the wave elevations are assumed small. Additionally, the velocity components are extrapolated linearly between the calm water level and the instantaneous free surface.

Dawson (1977) used a technique very similar to Gadd (1976) in order to tackle the two- and three-dimensional steady flow problem. The free surface conditions are linearised in terms of the double-body flow. The main difference in Dawson's method is that no artificial smoothing was used in the numerical algorithm in contrast to Gadd (1976).

Maruo and Ogiwara (1985) established a first-order Rankine panel method based on slow-ship linearisation. Although the free surface conditions that are implemented in the numerical algorithm are claimed to be nonlinear, the boundary conditions that have to be imposed on the instantaneous position of the free surface are transferred to the mean free surface using an expansion scheme and higher order terms are omitted in this process. Therefore, the proposed method does not solve the exact nonlinear problem. An application of the method is presented for a mathematically defined hull form. An artificial reduction factor is used for the nonlinear contributions at the bow and stern of the hull due to non-convergence of the iterative scheme. The wave profile predictions show improvements over corresponding results obtained by Michell's thin-ship theory. The wave resistance computations are carried out for a range of Froude numbers between 0.183 and 0.289. Even though the predicted wave resistance coefficients exhibit the correct trend, they show large deviations from the experimental measurements. The discrepancies in the results can mainly be attributed to the assumption of a linear variation of the fluid pressure between the actual free surface and the calm water surface and to the expansion scheme used for transferring the free surface boundary conditions to the mean free surface.

Raven (1990) analysed the linearised free surface conditions implemented for the ship-wave resistance problem. Three conditions were taken into account: the Kelvin condition (see, for example, Marr and Jackson (1999)), which is a uniform-flow linearisation and Eggers' and Dawson's free surface conditions (see Eggers (1981) and Dawson (1977)) that are based on the slow-ship linearisation scheme. The Rankine panel method is used for the implementation of these three different formulations. The Kelvin and Dawson conditions predict similar wave resistance coefficients for a Wigley hull travelling at $F_n = 0.4$ since the hull has a slender form. The predictions start to diverge for fuller hull forms. On the other hand, for a tanker hull with a block coefficient of 0.82 at $F_n = 0.18$, both Eggers' and Dawson's conditions yield negative resistance values. This negative-resistance paradox is related to the fact that the boundary conditions are applied on the calm water plane instead of the instantaneous free surface. Errors due to this linearisation cause an energy flux through the calculated wave surface resulting in a negative resistance value. Raven (1990) concluded that all linearised conditions contain inconsistencies and that this underlined the necessity for a nonlinear formulation.

For other examples of linear steady Rankine source methods see Cheng (1989), Reed et al. (1990), Yasukawa (1989), Telste and Reed (1993), Nakos and Sclavounos (1994), all of which employ formulations similar to those mentioned above; however they specifically study stern flow prediction, shallow water and channel problems.

2.1.2 Linear Unified Methods

An alternative to steady methods is the unified method, by which one can model the unsteady motions of a ship in a seaway as well as the steady wave pattern of that ship. Several examples of such formulations are investigated that employ linear Rankine source methods. Nonlinear unified methods are discussed in section 2.2.2.

Nakos and Sclavounos (1990b) presented a first-order Rankine panel method for the computation of steady and time-harmonic (frequency-dependent) wave patterns and for the evaluation of hydrodynamic coefficients and motions of ships. The formulation uses linearised free surface conditions, where the double-body flow is utilised as a base disturbance. The body boundary condition is also linearised about the mean position of the wetted surface, as in most of the linear methods. The convergence properties of the quadratic spline scheme that is employed for the solution of the unknown potentials are examined in a previous study (Nakos and Sclavounos (1990a)). A comparison with experimental measurements is not available for the steady wave pattern calculations. On the other hand, the predictions for hydrodynamic coefficients and motions of a Wigley hull at $F_n = 0.3$ and a Series 60 hull at $F_n = 0.2$ compare well with the experiments and show improvements over corresponding strip-theory computations (see, for example, Korvin-Kroukovsky (1955), Korvin-Kroukovsky and Jacobs (1957), Gerritsma and Beukelman (1967), Salvesen et al. (1970)). The unsteady computations are carried out in head waves for both hulls; hence, the hydrodynamic coefficients and forces are only examined for heave and pitch motions. Kring and Sclavounos (1991) extended the same method to multi-hull configurations.

van't Veer (1997) also applied a first-order Rankine panel method to a catamaran to account for three-dimensional effects such as the interaction of the waves generated by the demi-hulls. Free surface boundary conditions are once again linearised about the double-body flow. When trim and sinkage effects are included in the formulation, discrepancies with the experiments are reduced for both the steady and the unsteady computations at $F_n = 0.6$. The steady and unsteady flow problems are solved separately by assuming the steady and unsteady velocity potentials to be independent of each other.

Takaki and Iwashita (2000) compared their experimental results with predictions obtained using three different methods: strip theory, Rankine panel method and high-speed slender-body theory (HSST), which is also known as 2½D strip theory (Faltinsen

and Zhao (1991)), since it satisfies a two-dimensional Laplace's equation and a three-dimensional linear free surface condition. The experiments were carried out for a high-speed fishing boat at varying Froude numbers up to 0.8. HSST provided more accurate results than the other methods. However, in the Rankine panel method, linear free surface boundary conditions are used and the transom stern is assumed as a dry surface, both of which may be reasons for the poor predictions of the Rankine panel method. For deeply immersed transoms at low speeds in particular, the dry surface assumption is not valid. Nevertheless, for high speeds, the flow leaves the hull tangential to the lower edge of the stern, leaving the transom dry.

2.2 Nonlinear Rankine Source Methods

The 'nonlinear' term in this discussion does not mean that the solution is obtained on a fully nonlinear basis. Rankine source methods enforce potential flow theory; hence, by definition, nonlinear viscous effects are neglected, together with wave breaking and spray effects. The effects of surface tension and propulsion devices are also disregarded. Here, the nonlinear terms represent the nonlinearities in the boundary conditions, pressure equation (e.g. velocity-squared term), incident waves and the hull-free surface interaction.

2.2.1 Nonlinear Steady Methods

Both the linear and nonlinear steady methods mentioned reach the final solution in an iterative manner. That is to say, starting with an initial approximation, the aim in these methods is to converge to a desired solution in several iterations.

Nonlinear steady methods differ from the linear ones in the implementation of the boundary conditions. In a nonlinear steady method, the boundary conditions are satisfied on the exact (wavy) free surface at the end of the iteration process in contrast to

the linear ones given in section 2.1.1, in which computations are stopped when a predefined linear condition is satisfied. The iteration process starts with an initial guess of the free surface position and the velocity distribution. In each step, the body boundary condition and linearised free surface conditions are used to evaluate the source strengths and the wave elevation. Ideally, the iteration should continue until the results converge to a fully nonlinear solution. However, in practice, a convergence criterion is usually introduced and the iteration process stops when the residual error between iterations satisfies a prescribed tolerance (Kim and Lucas (1990)).

Raven (1993, 1996) managed to solve the fully nonlinear steady flow problem by using a raised-panel method. Wave pattern and resistance predictions are undertaken for a variety of hull forms including a Wigley hull, container ship and a frigate. It is stated that the main reasons for placing the free surface panels above the fluid domain were to reduce numerical dispersion (Raven (1992)), i.e. the longitudinal shifts observed in the wave pattern and to be able to keep the free surface panels fixed for some time in order to increase numerical stability.

A previous method by Jensen et al. (1989) uses a similar formulation, in which the hull boundary is discretised with source panels as in Raven (1996). However, instead of source panels, Rankine point sources are placed above the free surface to reduce the computational time. The method is applied to a Series 60 hull form with the aim of predicting its wave-making resistance characteristics. The numerical predictions are presented up to $F_n = 0.4$ and show improvements over the corresponding Neumann-Kelvin computations. Additionally, the same algorithm is utilised for the prediction of the dynamic sinkage of a container ship in shallow water and wave-making resistance of a SWATH (Small Waterplane Area Twin Hull) form. The results for the container ship are compared with other numerical methods without any experimental validation. In the case of the SWATH form, the wave-making resistance predictions show large deviations from experimental measurements at low Froude numbers. No results could

be obtained for high Froude numbers due to non-convergence of the algorithm for this particular hull form at high speeds.

Janson and Larsson (1996) implemented a zonal approach to model the steady flow problem for the optimisation of resistance of ship hulls. The raised-panel method is adopted for the entire hull and a part of its surrounding free surface in order to model the wave-making of the ship hull. Two other methods are utilised to account for viscous resistance: The RANS method in the wake region behind the stern and a boundary layer method in the near-field of fluid/structure interaction. Even though the zonal approach captured most of the physics of the problem (especially the viscous effects, which are disregarded in potential flow methods), comparisons with experiments for a Series 60 hull ($C_B = 0.6$, $F_n = 0.316$) are relatively poor. Since three different methods are incorporated into the formulation, the reason for the discrepancies is not clear. However, the disagreement with the measurements can be attributed to neglecting nonlinear effects on wave-making that stem from the linearised free surface conditions used in the raised-panel method.

Wyatt (2000) introduced a different approach by combining the Rankine and Havelock singularities for the solution of the nonlinear steady flow problem. While discretising the wetted hull surface with first-order Rankine source panels, Wyatt positioned Rankine point sources above the free surface and used Havelock point sources along the downstream edge of the computational domain. Havelock singularities satisfy a combined linear free surface condition as opposed to the Rankine singularities, which only satisfy Laplace's equation. Hence, with the use of Havelock sources at the truncated boundaries, an explicitly stated radiation condition is not necessary to prevent wave reflection from the edges of the computational domain. In view of this fact, Havelock singularities were used in Wyatt (2000) to enforce the downstream radiation condition. For the case of a Series 60 hull at a Froude number of 0.316, the numerical algorithm overpredicts the stern wave system; whereas, for a naval combatant with a transom stern the amplitudes of both the stern and bow waves are overestimated. Wave

resistance predictions are not presented for these hull forms. The deviations from measurements can mostly be attributed to wave breaking taking place at the bow and stern of the hulls which forms a natural damping mechanism in the vicinity of these regions. Evidently, wave breaking and associated effects cannot be captured by a potential flow solver.

See Raven (1998) for a comprehensive review of nonlinear steady Rankine source methods.

2.2.2 Nonlinear Unified Methods

Maskew (1992) developed a general nonlinear Rankine panel method by using a time-domain formulation. The method uses source and doublet singularity panels on all possible boundaries e.g. ocean floor, towing tank, channel walls. The waves are introduced into the computational domain by a sinusoidal wave generator positioned at the upstream boundary. Computed results are presented for a frigate in large amplitude motion without any experimental validation.

Beck et al. (1994) used the desingularised approach to formulate the three-dimensional nonlinear potential flow problem. The wave profile of a Wigley hull advancing in calm water compares well with the measurements at $F_n = 0.25$. Both the experiments and the computations are carried out at fixed sinkage and trim. For the unsteady case, numerical predictions are presented for forced heave and pitch motions and for corresponding hydrodynamic coefficients. In a later study by Scorpio (1997), a multipole acceleration technique is implemented to reduce the computational effort. The underlying idea in multipole acceleration is to reduce the required storage, thus to increase the computational efficiency. First, Laplace's equation is solved in spherical coordinates using the method of separation of variables. Then, by using the multipole algorithm, the influence of groups of far-field sources is approximated with expansions. These

expansions replace the influence coefficient matrix. It is claimed that the multipole accelerated desingularised method reduced the storage requirement from $O(N^2)$ to $O(N)$. For details and the development of this particular desingularised algorithm, see Beck et al. (1993), Scorpio et al. (1996), Celebi and Beck (1997), Subramani et al. (1998) and Celebi (2000).

A quasi-nonlinear time-domain algorithm was developed in Massachusetts Institute of Technology (see Kring et al. (1996), Huang (1997), Huang and Sclavounos (1998)), which is an extension of the linear Rankine panel method of Kring (1994). The quasi-nonlinear formulation does not restrict the amplitude of the incoming wave system or the motions of the hull, but the perturbation potential is assumed small compared to the incident wave potential. This so-called weak-scatterer theory (Pawlowski (1992)) is justified by the slenderness of ship hulls.

A more recent study by Liu et al. (2001) investigates the development of waves on the bow of a ship hull advancing in calm water and the diffraction of regular waves by a surface-piercing vertical cylinder with the aid of a higher-order Rankine panel method. The steady-state bow wave profiles obtained by a time-domain formulation for a Wigley and a Series 60 hull at $F_n = 0.316$ agree well with experimental measurements. Xue et al. (2001) used this nonlinear Rankine panel method to study the dynamics of three-dimensional overturning breaking waves and the generation mechanism of steep crescent waves.

2.3 Conclusions

There are several possible means of employing the Rankine source method for the solution of the potential flow around a ship hull, as discussed in the preceding sections. To carry on a further study one of them has to be chosen through considering the suitability of a particular method to the aims of this study as presented in chapter 1.

In view of the limitations of the linear methods (see, for example, Raven (1990)) and the available computational power, the need for a nonlinear formulation is obvious. The objective is a unified method to solve the steady flow problem, and through proper adjustments be extended for the solution of the unsteady problem. It is not possible to use the Rankine source methods reviewed in sections 2.1.1 and 2.2.1 for this purpose, since they cannot be adapted to model unsteady flow. On the other hand, the nonlinear behaviour of a ship in a natural seaway cannot be captured adequately by a frequency-domain method, in which the total ship reaction to the seaway is deduced from the superposition of its reactions to elementary waves and the time dependence is assumed to be harmonic. Thus, a time-domain method is essential to reproduce the real physical phenomenon as accurately as possible and to simulate the transient development of the flow characteristics.

Another point to consider is the computational efficiency of the preferred method. Discretisation of the boundary surfaces and the solution of the boundary value problem take most of the computational effort. The nonlinear Rankine source methods that have been reviewed require several hours of CPU time on parallel or supercomputers. The greatest challenge is to reduce the required computing time significantly, so as to be able to apply the method on personal computers.

A major drawback of the Rankine panel method is the issue of the singularity resulting from overlapping field and source points. A proper treatment of these singularities requires complex numerical schemes (e.g. Kang and Gong (1990)). The singularity issue aside, both in the Rankine panel and raised-panel methods, the evaluation of surface integrals over boundary panels significantly increases the required computing time.

The desingularised approach is more suitable than the other two methods to the aims of this thesis as discussed below:

- The singularities are distributed outside the control surface in the desingularised approach. Therefore, the integration and control surfaces never coincide.

- The use of point sources reduces the computational effort considerably as stated by Scorpio (1997). When point sources are used instead of source panels, the necessity to evaluate surface integrals is eliminated and the integrals are replaced by simple summations (see equations 4.5 and 4.6).

- Due to desingularisation, the velocity field induced in the fluid domain is much smoother than with a usual method and is continuous in the neighbourhood of the boundaries (Raven (1996), Musker (1988, 1989)).

- A possible drawback of the desingularised approach is that its application is limited to simple geometries in the literature. However, the method can be extended to complex hull forms once an efficient geometry processor is established that is capable of representing arbitrarily-shaped hull forms.

Bearing in mind the cited advantages and shortcomings, a unified nonlinear time-domain method is adopted in this study by using the desingularised approach and its formulation is given in the following chapters.

3. MATHEMATICAL MODEL

The physics of the fluid flow around a hull can be captured by the Navier-Stokes equations together with the continuity equation, which are the statements of the physical principles of conservation of momentum and conservation of mass respectively. In a two-dimensional case (see figure 3.1) the latter states that the total mass flux has to fulfil

$$-\rho dyu + \rho dy(u + u_x dx) - \rho dxv + \rho dx(v + v_y dy) = 0, \tag{3.1}$$

where ρ is the fluid density, u and v are the velocity components in x and y directions respectively. u_x and v_y denote the partial derivatives of the velocities, e.g. $u_x = \partial u / \partial x$. Equation 3.1 simplifies to the well-known continuity equation, which states that within a control volume the amount of mass remains constant, i.e. any amount flowing into a control volume flows out of it at the same time; namely,

$$u_x + v_y = 0. \tag{3.2}$$

Given a velocity component w in the z direction, the continuity equation in three dimensions can be derived in a similar manner:

$$u_x + v_y + w_z = 0. \tag{3.3}$$

In the equations above and for the rest of the discussion, the fluid is regarded as incompressible due to the relatively low speeds observed in ship flows. Additionally, the density of the fluid is taken as a constant assuming that the density variation in the vicinity of the ship is negligible.

The conservation of momentum in the flow is satisfied by the Navier-Stokes equations given below. For the derivation of the Navier-Stokes equations from first principles, see, for example, Acheson (2000).

$$\begin{aligned}
\rho\left(u_t + uu_x + vu_y + wu_z\right) &= \rho f_1 - p_x + \mu\left(u_{xx} + u_{yy} + u_{zz}\right), \\
\rho\left(v_t + uv_x + vv_y + wv_z\right) &= \rho f_2 - p_y + \mu\left(v_{xx} + v_{yy} + v_{zz}\right), \\
\rho\left(w_t + uw_x + vw_y + ww_z\right) &= \rho f_3 - p_z + \mu\left(w_{xx} + w_{yy} + w_{zz}\right),
\end{aligned} \tag{3.4}$$

where f_i is the acceleration due to a volumetric force, p is the pressure, μ is the viscosity of the fluid and t denotes time.

Equations 3.3 and 3.4 form a system of four coupled nonlinear partial differential equations for the unknown pressure and velocity components. An analytical solution of this system is impossible for the flow around a ship hull. A numerical solution is also not possible with today's computational power due to the highly nonlinear nature of the problem. Even if such a solution might become possible in the future, its necessity is questionable for a naval architect. As stated before, the aim in this study is to find a way of obtaining a solution that would require much less computational power and would still describe the physical phenomenon as accurately as possible; hence, simplification of the problem is crucial.

For flows with a high Reynolds number, the viscous effects are confined to a thin boundary layer around the hull and to a viscous region behind the hull. Therefore, it may be assumed that global flow characteristics are not affected by the viscosity of the fluid and consequently the viscosity can be disregarded. For an inviscid fluid, the Navier-Stokes equations reduce to Euler equations:

$$\begin{aligned}
\rho\left(u_t + uu_x + vu_y + wu_z\right) &= \rho f_1 - p_x, \\
\rho\left(v_t + uv_x + vv_y + wv_z\right) &= \rho f_2 - p_y, \\
\rho\left(w_t + uw_x + vw_y + ww_z\right) &= \rho f_3 - p_z.
\end{aligned} \tag{3.5}$$

As a further simplification, the fluid flow is assumed irrotational, which again might be considered relevant outside the boundary layer and the wake region. In fact, since the rotational motion of the flow is triggered by the fluid adhering to the hull; rotational effects are already lost by assuming the fluid inviscid (nonetheless, it is possible to introduce circulation in the flow to model, for instance, lifting surfaces by means of a

surface vorticity distribution. See, for example, Janson (2000), Hsin and Chou (1998) for further details). Now, the total flow field can be described by a velocity potential function Φ that satisfies Laplace's equation in the fluid domain:

$$\nabla^2\Phi = 0\,. \tag{3.6}$$

Equation 3.3 is reduced to Laplace's equation, which is a linear elliptic partial differential equation. Now, the three unknown velocity components are coupled by one function, that is

$$\begin{Bmatrix} u \\ v \\ w \end{Bmatrix} = \nabla\Phi\,. \tag{3.7}$$

Finally, by limiting the volumetric forces in Euler equations to gravity forces, conservation of momentum is satisfied by Bernoulli's equation; consequently, a relation between the pressure and the time derivative and gradients of the velocity potential is established:

$$\Phi_t + \frac{1}{2}(\nabla\Phi)^2 + gz + \frac{1}{\rho}p = c\,, \tag{3.8}$$

where g is the acceleration due to gravity force, c is a constant and the z-axis points upwards.

As a result of the assumptions given above, some important physical properties, which are mainly related to the viscous flow in the vicinity of the hull, are disregarded. However, for the simulation of the global loads and corresponding motions of the ship hull, the solution might well be adequate for engineering purposes.

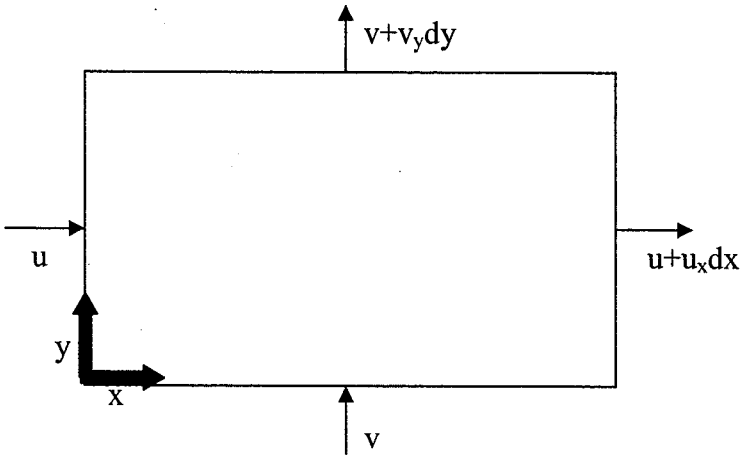

Figure 3.1: Control volume used for the derivation of the continuity equation in two dimensions.

3.1 Initial Boundary Value Problem

In reality, the fluid domain might be considered infinite relative to the scale of the ship. However, for computational purposes, boundaries surrounding the fluid domain have to be truncated as shown in figure 3.2, where S_H represents the hull boundary, S_F the free surface, S_B the bottom boundary and S_T the truncated boundaries. Initial and boundary conditions have to be imposed on all boundary surfaces and Laplace's equation (3.6) must be satisfied in the fluid domain.

A Cartesian coordinate system $\vec{x} = (x, y, z)$ is chosen to formulate the mathematical model. The coordinate system is fixed in the hull and its origin is at the centre-plane of the ship at amidships. The y-axis points to the starboard side, x is positive downstream and z is positive upwards. x and y lie in the plane of the undisturbed free surface.

For a ship travelling with a speed of $U(t)$ in the $-x$ direction, where t denotes time-dependence, the total velocity potential may be decomposed as

$$\Phi(\vec{x}, t) = U(t)x + \phi(\vec{x}, t). \tag{3.9}$$

The problem is solved for the perturbation potential ϕ, which also has to satisfy Laplace's equation in the whole fluid domain. That is to say,

$$\nabla^2 \phi(\vec{x}, t) = 0. \tag{3.10}$$

3.1.1 Initial Conditions

Kelvin's theorem (see, for example, Acheson (2000)) implies that if a flow is irrotational at some instant of time then it will remain irrotational provided that the density is constant and the fluid is inviscid and incompressible. Since the latter conditions are satisfied by the potential flow theory, when the problem is started from

rest, the flow will remain irrotational for the rest of the simulation and the appropriate initial conditions will be

$$\begin{aligned} &\phi(\vec{x},t)=0 \quad \text{at } t=0, \\ &\eta(x,y,t)=\eta_0(x,y) \quad \text{on } S_F \quad \text{at } t=0, \end{aligned} \tag{3.11}$$

where $\eta_0(x,y)$ is the known free surface elevation.

3.1.2 Boundary Conditions

For a viscous fluid, the normal and tangential components of fluid velocity at a solid boundary must be equal to those on the boundary itself. Since the fluid is assumed inviscid in potential theory, no condition is required for the tangential component. On the other hand, a kinematic condition is required to ensure that there is no flow penetrating the boundaries. On the hull boundary, the kinematic condition is

$$\vec{n}\cdot\nabla\phi=-n_1U(t)+\vec{n}\cdot\frac{\partial\vec{\delta}_h}{\partial t} \quad \text{on } S_H. \tag{3.12}$$

Equation 3.12 is derived simply from $\vec{n}\cdot\nabla\Phi=0$ and takes account of the oscillatory motions of the hull. $\vec{n}=(n_1,n_2,n_3)$ is the unit normal vector that points into the boundary surface. Subscripts $1,2,3$ refer to components along x, y and z axes respectively. The oscillatory displacement of the ship $\vec{\delta}_h$ is given as

$$\vec{\delta}_h=\vec{\gamma}_t+\vec{\gamma}_r\times\vec{x}, \tag{3.13}$$

where $\vec{\gamma}_t$ and $\vec{\gamma}_r$ are the translational and rotational displacements of the hull respectively (Huang (1997)).

A similar expression may be written to impose the kinematic condition on the bottom boundary:

$$\vec{n}\cdot\nabla\phi=-n_1U(t)+\vec{n}\cdot\vec{V}_B \quad \text{on } S_B. \tag{3.14}$$

In equation 3.14, $\vec{V}_B$ is the velocity of the bottom boundary relative to the hull-fixed coordinate system.

Two conditions have to be applied on the free surface boundary. In addition to a kinematic condition, a dynamic condition is also necessary, which ensures that the free surface pressure is equal to a prescribed value. The kinematic and dynamic free surface boundary conditions are written respectively as,

$$\frac{\partial \eta}{\partial t} = \frac{\partial \phi}{\partial z} - \nabla\phi \cdot \nabla\eta - U(t)\frac{\partial \eta}{\partial x} \quad \text{on } S_F, \tag{3.15}$$

$$\frac{\partial \phi}{\partial t} = -g\eta - \frac{1}{2}\nabla\phi \cdot \nabla\phi - U(t)\frac{\partial \phi}{\partial x} - \frac{P_a}{\rho} \quad \text{on } S_F. \tag{3.16}$$

In these equations, free surface elevation is defined by the single-valued function $z = \eta(x, y, t)$ owing to the fact that the overturning of waves is neglected. Surface tension being ignored, the atmospheric pressure P_a is assumed to be transferred directly to the fluid across the free surface.

In addition to these boundary conditions a condition in the far-field has to be satisfied which is given as

$$\nabla\phi \to 0 \quad \text{as} \quad \sqrt{x^2 + y^2} \to \infty. \tag{3.17}$$

However, since the computational domain must be finite, the far-field condition is approximated by a numerically imposed radiation condition on the truncated boundaries. This radiation condition has to be applied in such a manner that the ship-generated disturbances, and waves that enter the computational domain from the upstream boundary, pass through the truncated boundaries without reflection. Details of the radiation condition are given in section 4.3.1.

Initial and boundary conditions are satisfied throughout the fluid domain to evaluate the unknown velocity field. Once the velocity potential and hence the components of the fluid velocity are known, hydrodynamic forces and moments acting on the hull may be calculated by Bernoulli's equation (see equation 3.8).

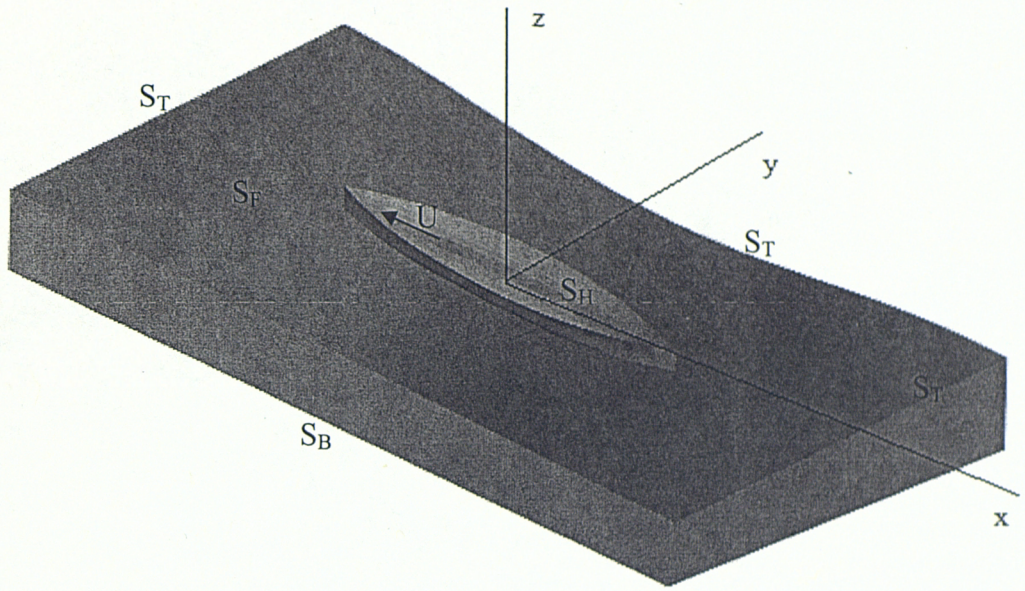

Figure 3.2: Hull-fixed coordinate system and the boundary surfaces.

4. NUMERICAL SOLUTION

The Euler-Lagrange time-stepping technique, originally due to Longuet-Higgins and Cokelet (1976), is adopted in this study for the implementation of the mathematical model described in chapter 3. The Euler-Lagrange method consists of two phases. In the Lagrange phase, individual nodes on the free surface are tracked by time-stepping the free surface boundary conditions. Since the fluid velocities are required to integrate the free surface conditions with respect to time, an initial-boundary value problem is solved in the Euler phase to obtain the velocities. Details of the formulation are given in the following sections.

4.1 Euler Phase

The Euler phase consists of the solution of Laplace's equation subject to the initial conditions and boundary conditions on the surfaces surrounding the fluid, namely,

$$\begin{aligned} &\nabla^2\phi = 0, \\ &\phi = \phi_0 \quad \text{on } S_F, \\ &\eta = \eta_0 \quad \text{on } S_F, \\ &\vec{n}\cdot\nabla\phi = -n_1 U + \vec{n}\cdot\frac{\partial\vec{\delta}_h}{\partial t} \quad \text{on } S_H, \\ &\vec{n}\cdot\nabla\phi = -n_1 U + \vec{n}\cdot\vec{V}_B \quad \text{on } S_B, \end{aligned} \tag{4.1}$$

where ϕ_0 is the known velocity potential on the free surface at the current time step. In addition to equation 4.1, an appropriate radiation condition (see section 4.3.1) must be applied on the truncated boundaries (S_T).

If a Green's function is used to solve Laplace's equation, the order of the problem reduces by one and the velocity potential may be found by solving the resulting integral equation,

$$\phi(\vec{x}) = \iint_S \sigma(\vec{\xi}) G(\vec{x}, \vec{\xi}) dS\,, \tag{4.2}$$

where S is the integration surface, σ is the unknown strength of a source located at point $\vec{\xi}$ and G is the Rankine source Green's function given as

$$G(\vec{x}, \vec{\xi}) = \frac{1}{\left|\vec{x} - \vec{\xi}\right|}. \tag{4.3}$$

Equation 4.2 is usually known as a source-only formulation (or indirect method). When a source-only formulation is used, fluid velocities are computed only after source strengths are determined in contrast to direct methods (see, for example, Kring (1994), Huang (1997)). The direct method yields higher accuracy for lifting flows; however, the resulting algorithm is computationally intensive, as stated by Bertram (2000).

Computations are carried out for infinite depth. The relevant boundary condition for infinite depth is given as

$$\nabla\phi \to 0 \quad \text{as} \quad z \to -\infty\,, \tag{4.4}$$

which is inherently satisfied by the Rankine source Green's function. The explicit use of a bottom boundary condition is thus not required. On the other hand, the Rankine source Green's function does not satisfy any other boundary or initial conditions. Therefore, the initial and remaining boundary conditions in equation 4.1 are expressed through the indirect method given in equation 4.2 as

$$\begin{aligned} &\iint_S \sigma(\vec{\xi}) G(\vec{x}, \vec{\xi}) dS = \phi_0 \quad \text{on } S_F, \\ &\iint_S \sigma(\vec{\xi}) \vec{n} \cdot \nabla G(\vec{x}, \vec{\xi}) dS = -n_1 U + \vec{n} \cdot \frac{\partial \vec{\delta}_h}{\partial t} \quad \text{on } S_H. \end{aligned} \tag{4.5}$$

4.1.1 The Desingularised Approach

By positioning the sources outside the actual fluid domain, the singularities when $\vec{x} = \vec{\xi}$ are avoided. In this desingularised approach, the sources are located inside the hull, above the free surface and outside the truncated boundaries. Therefore, the collocation and source points never coincide. The boundary conditions are satisfied at collocation points $\vec{x}$. In addition to this, if Rankine point sources are used instead of source panels, the integrals given in equation 4.5 may be replaced with summations,

$$\begin{aligned} &\sum_{i=1}^{N} \sigma_i G(\vec{x}_j, \vec{\xi}_i) = \phi_{0_j} \quad \text{on } S_F, \\ &\sum_{i=1}^{N} \sigma_i \vec{n}_j \cdot \nabla G(\vec{x}_j, \vec{\xi}_i) = -n_{1_j} U + \vec{n}_j \cdot \frac{\partial \vec{\delta}_{h_j}}{\partial t} \quad \text{on } S_H, \end{aligned} \tag{4.6}$$

where N is the total number of source points (which is also equal to the number of collocation points) and $i, j = 1, 2, ..., N$. The arrangement of the source and field (i.e. collocation) points is illustrated in figure 4.1 for the free surface and hull boundaries. The filled circles represent the source points and the empty ones the collocation points that are on the true boundaries. The collocation points where the free surface and the hull intersect need double nodes to be able to satisfy both the free surface conditions and the body boundary condition. It may also be a concern for the points where the free surface and a truncated boundary meet, if that truncated boundary is modelled as a rigid wall (see equation 4.13).

The summations in equation 4.6 together with the appropriate radiation conditions given in section 4.3.1 form a linear set of equations of order $N \times N$ (see equation 4.14) that are to be solved at each time step to evaluate the unknown source strengths. Once the source strengths are known, the fluid velocities may be calculated analytically; namely,

$$\nabla \phi(\vec{x}_j) = \sum_{i=1}^{N} \sigma_i \nabla G(\vec{x}_j, \vec{\xi}_i). \tag{4.7}$$

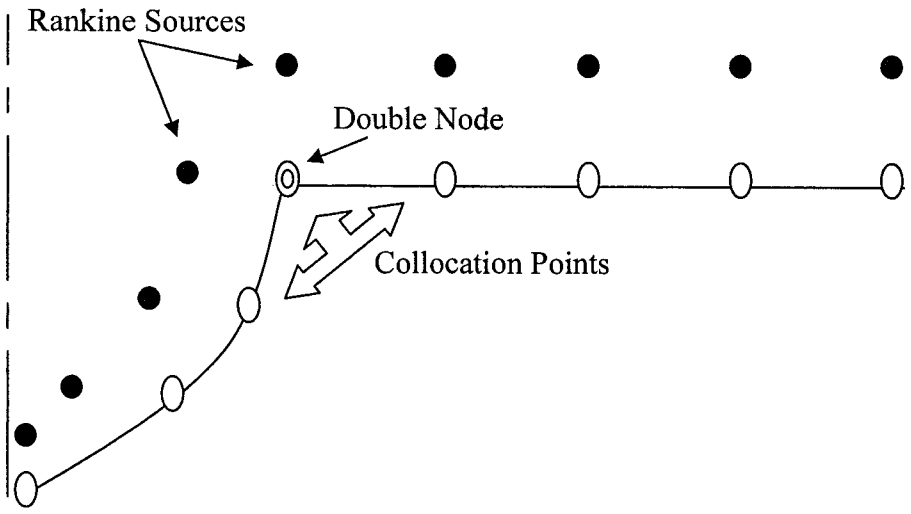

Figure 4.1: Arrangement of the Rankine sources (•) and collocation points (o).

4.2 Lagrange Phase

In the Lagrange phase, free surface boundary conditions (equations 3.15 and 3.16) are integrated in time using the fluid velocities obtained in the Euler phase. Initially, the kinematic free surface condition is stepped forward in time using the known velocity field. This time-stepping provides the change of wave elevation at the current time step, i.e. $\partial\eta/\partial t$. Subsequently, the dynamic free surface condition is integrated to obtain the new velocity potential on the free surface. Hence, with the integration of the free surface boundary conditions new values of ϕ and η are obtained, which are then used in the Euler phase of the next time step.

4.3 Numerical Scheme

The structure and details of the algorithm which is used to implement the numerical method given, are now discussed.

The choice of the programming language is not of paramount importance for this study. However, it should at least allow for dynamic memory allocation, which does not affect the overall CPU time but helps to minimise memory requirements. For an algorithm that has a large demand on memory, an effective memory management is not possible if the chosen programming language is capable of holding only static variables.

A more important (and most likely the first) step in a hydrodynamic analysis algorithm is the geometrical description of the boundary surfaces which is discussed at length in chapter 5. After the geometry and discrete representation of the boundary surfaces are determined, the next step in the solution is the simulation of the flow around the hull.

4.3.1 Flow Simulation – Euler Phase

As discussed in the mathematical model, the first phase of the flow simulation is the solution of the initial-boundary value problem.

If the hull is free to sink and trim, the hull boundary condition will be

$$\sum_{i=1}^{N} \sigma_i \vec{n}_j \cdot \nabla G(\vec{x}_j, \vec{\xi}_i) = -n_{1_j} U + \vec{n}_j \cdot \frac{\partial \vec{\delta}_{h_j}}{\partial t} \quad \text{on } S_H . \tag{4.8}$$

On the other hand; if the hull is restrained from sinkage and trim, the hull boundary condition may be reduced to

$$\sum_{i=1}^{N} \sigma_i \vec{n}_j \cdot \nabla G(\vec{x}_j, \vec{\xi}_i) = -n_{1_j} U \quad \text{on } S_H . \tag{4.9}$$

The initial condition on the free surface is given as

$$\sum_{i=1}^{N} \sigma_i G(\vec{x}_j, \vec{\xi}_i) = \phi_{0_j} \quad \text{on } S_F . \tag{4.10}$$

Equation 4.10 prescribes the velocity potential for the free surface collocation points. Since the simulation is started from rest, ϕ_0 is equal to zero at $t = 0$. For subsequent time steps, ϕ_0 is determined by integrating the dynamic free surface condition.

In addition to the equations above, a radiation condition must be satisfied on the truncated boundaries to complete the boundary value problem. For the side boundary, two options are considered. It may either be treated as an open boundary (hence no condition is applied) or as a wall-boundary. When the latter one is chosen, Rankine sources are placed outside the side boundary and a wall-boundary condition is imposed; namely,

$$\vec{n} \cdot \nabla \phi = 0 \quad \text{on } S_T . \tag{4.11}$$

Substituting equation 4.2 into equation 4.11 gives

$$\iint_S \sigma(\vec{\xi}) \vec{n} \cdot \nabla G(\vec{x}, \vec{\xi}) dS = 0 \quad \text{on } S_T . \tag{4.12}$$

And since point sources are used to define the velocity field, equation 4.12 can be rewritten as

$$\sum_{i=1}^{N} \sigma_i \vec{n}_j \cdot \nabla G(\vec{x}_j, \vec{\xi}_i) = 0 \quad \text{on } S_T \,. \tag{4.13}$$

The condition given above reflects all the wave energy back to the computational domain – a situation that is often observed in a towing tank. At the upstream boundary, the velocity potential ϕ and the wave elevation η are set to zero and the downstream is left as an open boundary owing to the idea that the free surface nodes convect downstream in a steady flow simulation and carry information out of the computational domain (Beck and Reed (2000)).

Equation 4.8 (or 4.9), 4.10 and 4.13 (if the side boundary is treated as a solid-boundary) are applied at N collocation points resulting in a set of linear equations:

$$[I]\{s\} = \{b\}, \tag{4.14}$$

where

$$I_{ji} = \begin{cases} \vec{n}_j \cdot \nabla_{\vec{x}_j} \dfrac{1}{\left|\vec{x}_j - \vec{\xi}_i\right|}; & \text{on solid boundaries} \\ \dfrac{1}{\left|\vec{x}_j - \vec{\xi}_i\right|} \quad ; & \text{on } S_F \end{cases},$$

$$b_j = \begin{cases} 0 \quad ; & \text{on } S_T \\ -n_{1_j} U \text{ or } -n_{1_j} U + \vec{n}_j \cdot \dfrac{\partial \vec{\delta}_{h_j}}{\partial t}; & \text{on } \mathrm{S_H} \\ \phi_{0_j} \quad ; & \text{on } S_F \end{cases}$$

and s_i's are the unknown source strengths.

The system of linear equations may be solved using direct solvers (such as Gauss elimination), iterative solvers or order-N methods (see, for example, Ferziger and Peric (2002)). The drawback of direct solvers is that they require N^3 operations to solve the equations. On the other hand, when an iterative or an order-N method is used, setting up

the equations may require more time than a direct solver. Details of the solution of equation 4.14 are discussed in section 7.3.

The solution of equation 4.14 yields the source strengths, which in turn are used for determining the fluid velocities (see equation 4.7).

4.3.2 Flow Simulation – Lagrange Phase

After the initial-boundary value problem is solved, the next step is the integration of the free surface boundary conditions. In terms of developing an algorithm for numerical solution, it is not efficient to implement the free surface conditions in their usual form (see equations 3.15 and 3.16). By adding $\vec{v}\cdot\nabla\eta$ to both sides of equation 3.15 and $\vec{v}\cdot\nabla\phi$ to both sides of equation 3.16 (Scorpio et al. 1996), the free surface boundary conditions can be rewritten as

$$\frac{\delta\eta}{\delta t}=\frac{\partial\phi}{\partial z}-\nabla\phi\cdot\nabla\eta+\vec{v}\cdot\nabla\eta-U(t)\frac{\partial\eta}{\partial x}\quad \text{on } S_F, \tag{4.15}$$

$$\frac{\delta\phi}{\delta t}=-g\eta-\frac{1}{2}\nabla\phi\cdot\nabla\phi-U(t)\frac{\partial\phi}{\partial x}-\frac{P_a}{\rho}+\vec{v}\cdot\nabla\phi\quad \text{on } S_F, \tag{4.16}$$

where $\frac{\delta}{\delta t}\equiv\frac{\partial}{\partial t}+\vec{v}\cdot\nabla$ is the time-derivative following a free surface point that has a prescribed velocity $\vec{v}$. The free surface conditions may now be adjusted to suit specific purposes. For instance, when the free surface nodes travel with the fluid velocity $\nabla\Phi$, they tend to penetrate the hull surface between time steps. However, by setting $\vec{v}=(0,0,\partial\eta/\partial t)$, their horizontal movements are constrained and they may only move vertically with the free surface. In this case, the kinematic and dynamic free surface conditions reduce to:

$$\frac{\partial\eta}{\partial t}=\frac{\partial\phi}{\partial z}-\nabla\phi\cdot\nabla\eta-U(t)\frac{\partial\eta}{\partial x}\quad \text{on } S_F, \tag{4.17}$$

$$\frac{\delta\phi}{\delta t}=-g\eta-\frac{1}{2}\nabla\phi\cdot\nabla\phi-\frac{P_a}{\rho}+\frac{\partial\eta}{\partial t}\frac{\partial\phi}{\partial z}-U(t)\frac{\partial\phi}{\partial x}\quad \text{on } S_F. \tag{4.18}$$

The right hand sides of the equations 4.17 and 4.18 are known at each time step. The fourth-order Runge-Kutta method (Ferziger and Peric (2000)) is adopted for their integration in order to determine the new velocity and wave elevation values.

Other numerical details are discussed at length in chapters 6, 7 and 8 for different kinds of problems that are examined.

5. DISCRETISATION OF BOUNDARY SURFACES

A discrete representation of the continuous physical problem that is to be solved is introduced in chapter 4 together with the details of the algorithm used to implement the chosen numerical method. The first step in a hydrodynamic analysis algorithm is the geometrical description of the computational domain. In a boundary element method (see Hess and Smith (1964)) this implies the discretisation of the boundary surfaces surrounding the fluid domain.

Discretisation of an analytically defined hull form is investigated in section 5.1 followed by a discussion on free surface representation in section 5.2. In section 5.3, a discretisation algorithm is introduced for mathematical representation of complex hull forms. The accuracy and capabilities of the algorithm are examined by discretising three different hull forms. Finally, problems that are faced when the flow simulation algorithm is applied to a Series 60 hull are discussed in section 5.4.

5.1 Geometric Description of the Wigley Hull

In order to discretise a hull surface with panels or nodes, one needs the geometric description of that surface defined either analytically or digitally. Initially, a Wigley hull is used for the purpose of inviscid flow simulation. Since the surface of the Wigley hull is analytically defined, it is a relatively easy task to discretise its hull surface at each time step. However, it is not possible to evaluate an analytical expression for an arbitrarily-shaped hull. A hull discretisation study is undertaken for the mathematical representation of real hull surfaces and is discussed in section 5.3. In this section, only the discretisation of the Wigley hull is considered.

The surface of the Wigley hull (Wigley (1934)) is described as

$$y(x,z) = B/2\left[1-\left(2x/L\right)^2\right]\left[1-\left(z/T\right)^2\right], \tag{5.1}$$

where L, B, T correspond to the length, breadth and draught of the hull.

At each time step, the collocation points are placed on the hull boundary in agreement with equation 5.1. Then, equation 5.1 is differentiated to obtain the normal vectors to the hull surface and the source points are located in the direction of the normal inside the hull boundary. The normal vector $\vec{N}$ at a point (x_0, z_0) on the hull surface $y = f(x,z)$ is given as

$$\vec{N} = \begin{bmatrix} f_x(x_0, z_0) \\ -1 \\ f_z(x_0, z_0) \end{bmatrix}. \tag{5.2}$$

Subsequently, unit normal vectors for the hull can be calculated, which are required for the body boundary condition:

$$\vec{n} = \frac{\vec{N}}{\left|\vec{N}\right|}. \tag{5.3}$$

5.2 Free Surface Representation

In contrast to the free surface Green's function, the Rankine source Green's function does not inherently satisfy the free surface boundary conditions. Consequently, not only the hull boundary but also the free surface must be discretised and due to the nature of the problem, this discretisation must be repeated at each time step. A cubic B-spline function is chosen as an accurate way of representing the free surface.

The definition of the B-spline surface Q is given as

$$Q(\beta, \chi) = \sum_{i=0}^{m}\sum_{j=0}^{n} B_{i,j} P_{i,3}(\beta) R_{j,3}(\chi) \tag{5.4}$$

for $m+1$ rows and $n+1$ columns of control points, where β and χ are the parametric values in the horizontal plane, $P_{i,3}$ and $R_{j,3}$ are the B-spline basis functions in the β and χ directions respectively and $B_{i,j}$'s are the vertices of the defining polygon net. The second subscripts in the basis functions $P_{i,3}$ and $R_{j,3}$ denote the degree of the curve in the parametrical β and χ directions correspondingly (degree 3 defines a cubic spline curve). A B-spline surface and its defining polygon net is illustrated in figure 5.1. The polygon net is placed vertically above the B-spline surface for illustrative purposes. For details of B-spline surfaces, see, for example, Rogers and Adams (1990), Bartels et al. (1986).

Aside from the discretisation of the free surface at each time step, the need for a mathematical representation of the free surface also comes from the fact that Rankine point sources are located at a small distance above the actual surface in the normal direction. Accordingly, normal vectors to the free surface and hence the partial derivatives of the surface have to be known. The parametric derivatives of the B-spline surface are calculated using the following equations:

$$\begin{aligned} Q_{\beta}(\beta,\chi) &= \sum_{i=0}^{m}\sum_{j=0}^{n} B_{i,j} P_{i,3}'(\beta) R_{j,3}(\chi), \\ Q_{\chi}(\beta,\chi) &= \sum_{i=0}^{m}\sum_{j=0}^{n} B_{i,j} P_{i,3}(\beta) R_{j,3}'(\chi), \end{aligned} \tag{5.5}$$

where prime denotes partial differentiation with respect to the corresponding parameter value.

The problem with the formulation given in equation 5.5 is that the defining polygon net $B_{i,j}$ is not known. However, free surface data points are known and the basis functions $P_{i,3}(\beta)$, $R_{j,3}(\chi)$ can easily be calculated once the parametric values β, χ are known at the data points.

In order to fit a B-spline surface to a set of known data points $D_{c,d}$, at first, two set of parameters ($s_c (0 \le c \le m)$ in the β direction and $t_d (0 \le d \le n)$ in the χ direction) have to be calculated. The chord length approximation is used for the evaluation of these sets of parameters. Once s_c and t_d are known, the knot vectors S_c and T_d are found by averaging the parameter values in each direction. The knot vectors are in turn used for computing the basis functions.

Equation 5.4 can now be rewritten as

$$D_{c,d} = \sum_{i=0}^{m} \sum_{j=0}^{n} B_{i,j} P_{i,3}(s_c) R_{j,3}(t_d), \tag{5.6}$$

i.e.

$$[D] = [C][B], \tag{5.7}$$

where $[D]$ is an $M \times 3$ matrix (M being the total number of field points on the free surface), $[C]$ is an $M \times M$ matrix of the products of the basis functions $P_{i,3}$ and $R_{j,3}$, and $[B]$ is the unknown $M \times 3$ matrix containing the vertices of the polygon net.

Once equation 5.7 is solved and the defining polygon is evaluated, the normal vectors and hence the location of the free surface source points can be determined.

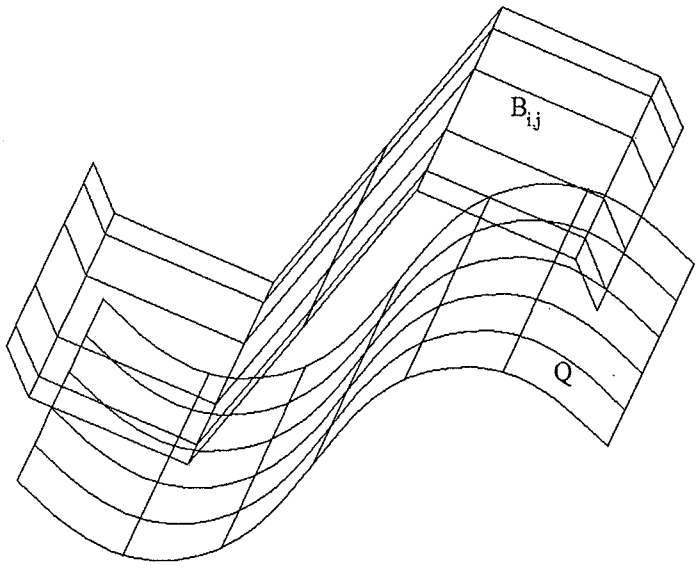

Figure 5.1: A B-spline surface (Q) and its defining polygon net ($B_{i,j}$).

5.3 Mathematical Representation of Arbitrarily-Shaped Hull Surfaces

The flow simulation is initially applied to a Wigley hull, which has an analytically defined body surface (see equations 5.1 and 5.8). In order to extend the algorithm to realistic hull shapes, a discretisation study is undertaken. Similar to the free surface representation mentioned in section 5.2, cubic B-splines are implemented to discretise the hull surfaces. The idea behind the discretisation algorithm is to generate as much data as possible with minimum input.

The algorithm requires offset values of the surfaces at stations along the length of the hull. The stations do not have to be on a 2D plane, i.e. data points on a particular station can lie at different x-coordinates. These input data are used to evaluate the defining polygon net by solving a set of equations in the form of equation 5.7. Once the vertices of the defining polygon are known, any grid point can be calculated in parametric space by using equation 5.4.

A yacht and an NPL hull are discretised in order to investigate the capabilities of the algorithm. For both hull forms, the input data consist of 25 points that are distributed evenly among five stations along the hull as shown in figures 5.2 and 5.3. The corresponding outputs are shown in figures 5.4 and 5.5. With relatively small amount of data, 441 grid points (21 stations each defined by 21 points) are evaluated in approximately one second of CPU time.

Since the algorithm uses the cubic B-spline method (i.e. series of third-order polynomials) to express a hull surface, there are some errors introduced due to discretisation. The order of errors increases with the geometric complexity of the hull form. The accuracy of the algorithm is investigated by comparing its output for a Wigley hull with the analytical calculations obtained from

$$y(x,z)=\begin{cases}\dfrac{B}{2}\left[1-\left(\dfrac{2x}{L}\right)^2\right]\left[1-\left(\dfrac{z}{T}\right)^2\right]; & z \text{ below waterline}\\ \dfrac{B}{2}\left[1-\left(\dfrac{2x}{L}\right)^2\right]\left[1+\left(\dfrac{z}{T}\right)^2\right]; & z \text{ above waterline}\end{cases} \quad (5.8)$$

Equation 5.8 defines a Wigley hull with flaring sides and hence a geometrically more complex body surface compared to a wall-sided hull.

The Wigley hull that is used as input for the algorithm and the resulting output are plotted in figures 5.6 and 5.7 respectively. In figure 5.8, the results from the discretisation code are compared with the analytical calculations for five stations along the hull. The dashed lines represent the analytical calculations, while the continuous ones represent the results from the discretisation code. There are some discrepancies in the vicinity of the free surface, where the hull form changes drastically. This indicates that the amount of input data was insufficient to capture the geometrical complexity of the sections in this region. When the amount of input data are increased, the computations match the analytical calculations more closely as shown in figure 5.9. For figures 5.8 and 5.9 each station was defined by 5 and 13 points respectively.

In all of the examples given above, each station has been considered as a single patch. Hence, it is assumed that the curvature values do not change significantly at a particular station. Obviously, this is not the case for a hull with cross-sections similar to the one given in figure 5.10. For instance, in figure 5.10, the curvature values in the second region are much higher than in regions 1 and 3. This section might better be defined by three different patches e.g. AB, BC and CD. Thus, it should be possible to maintain a similar accuracy in the results without necessarily increasing the number of input points.

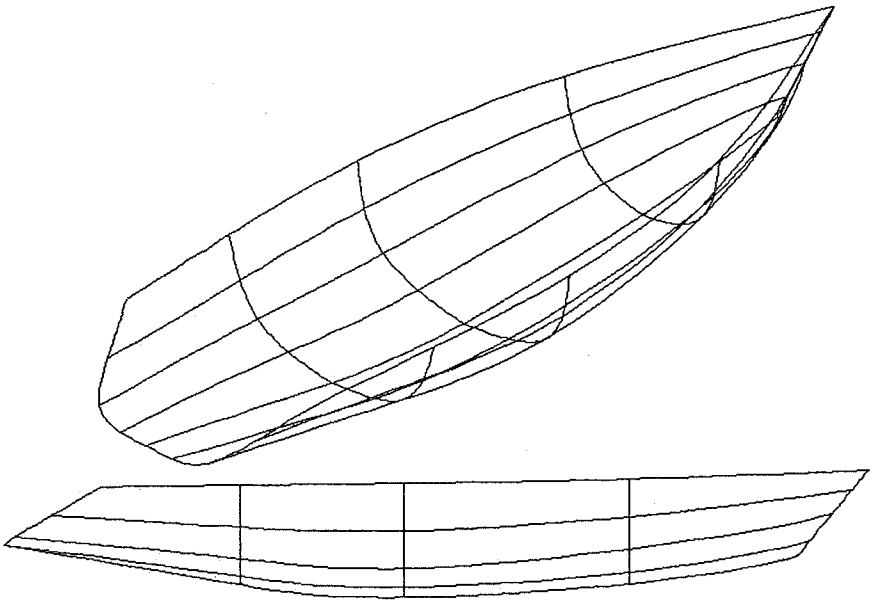

Figure 5.2: The input yacht hull for the discretisation algorithm.

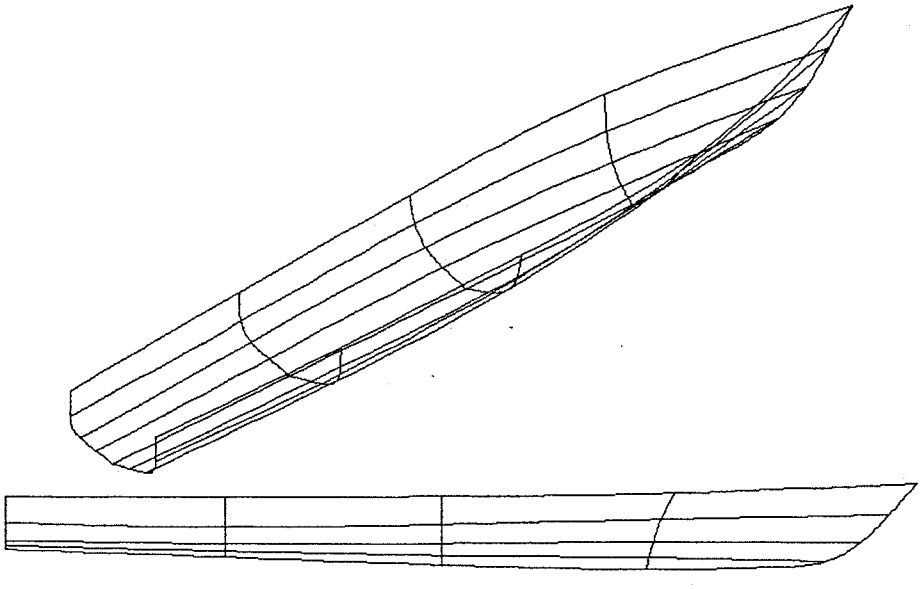

Figure 5.3: The input NPL hull for the discretisation algorithm.

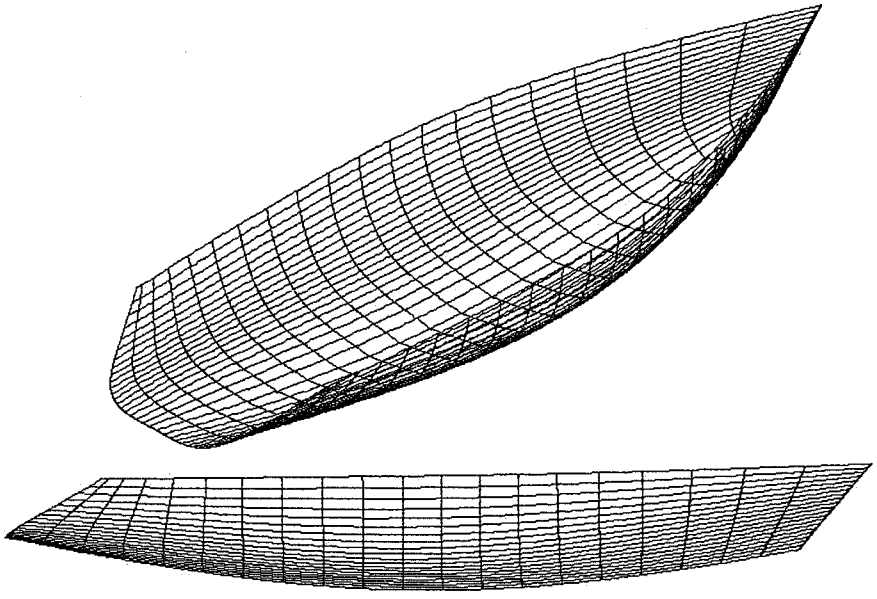

Figure 5.4: The output of the discretisation algorithm for the yacht hull.

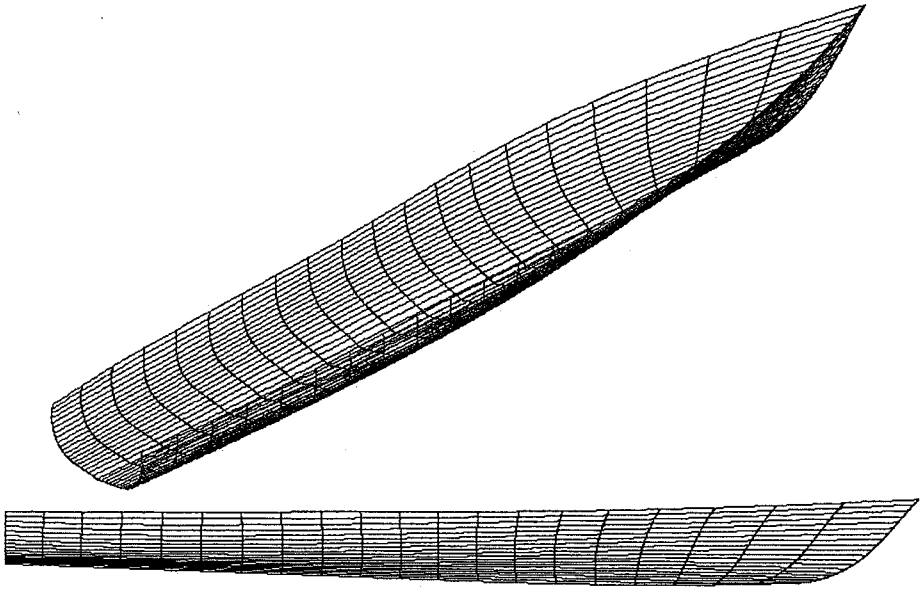

Figure 5.5: The output of the discretisation algorithm for the NPL hull.

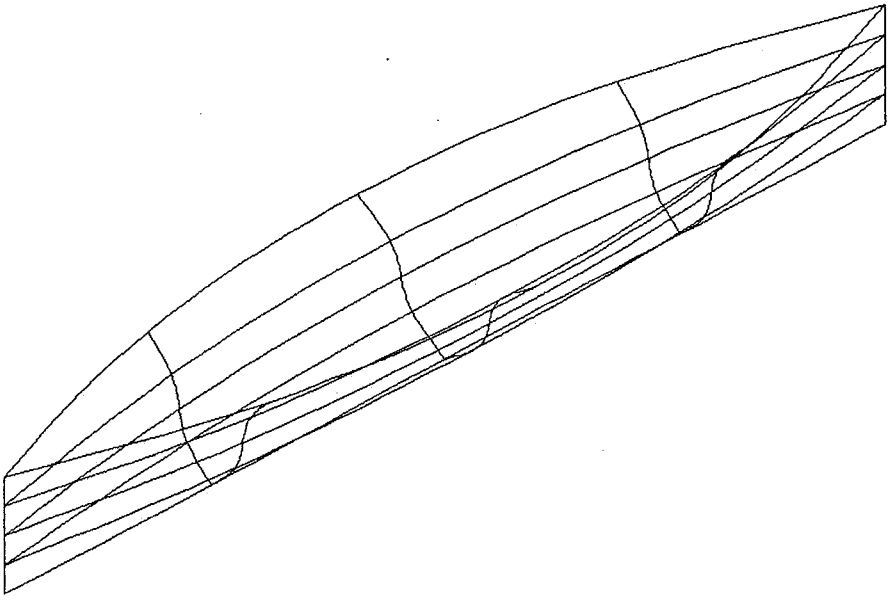

Figure 5.6: The input Wigley hull for the discretisation algorithm.

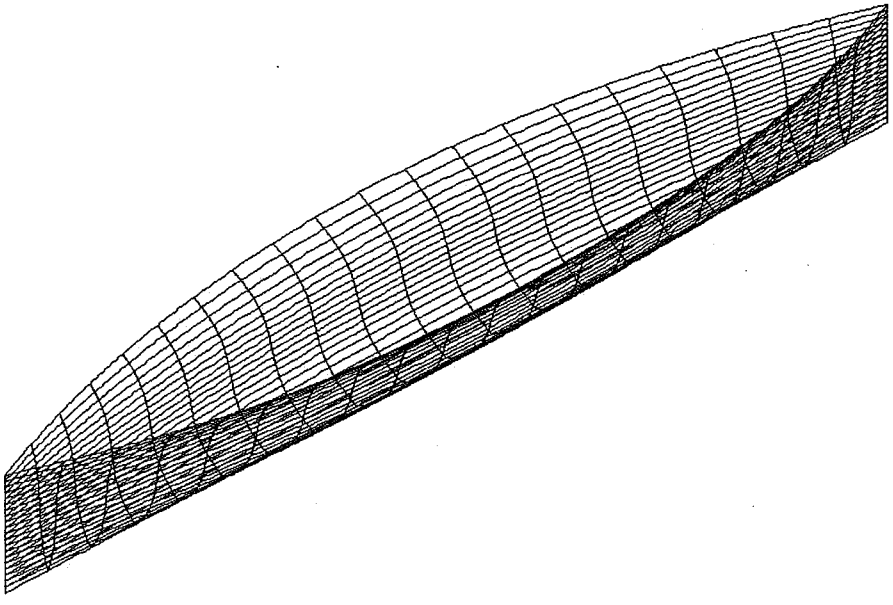

Figure 5.7: The output of the discretisation algorithm for the Wigley hull.

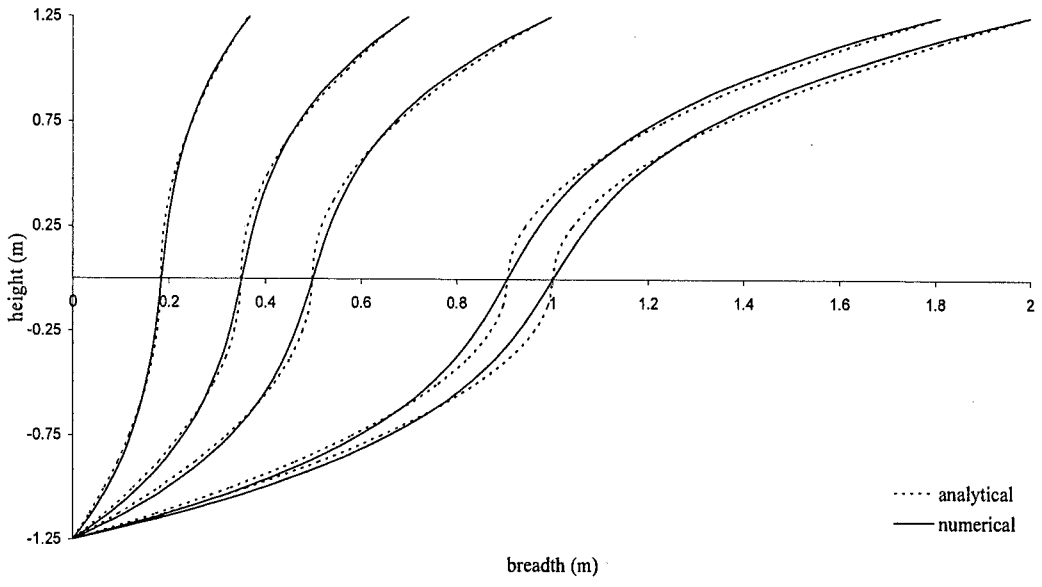

Figure 5.8: Comparison of offset values for the Wigley hull – input stations defined by 5 points.

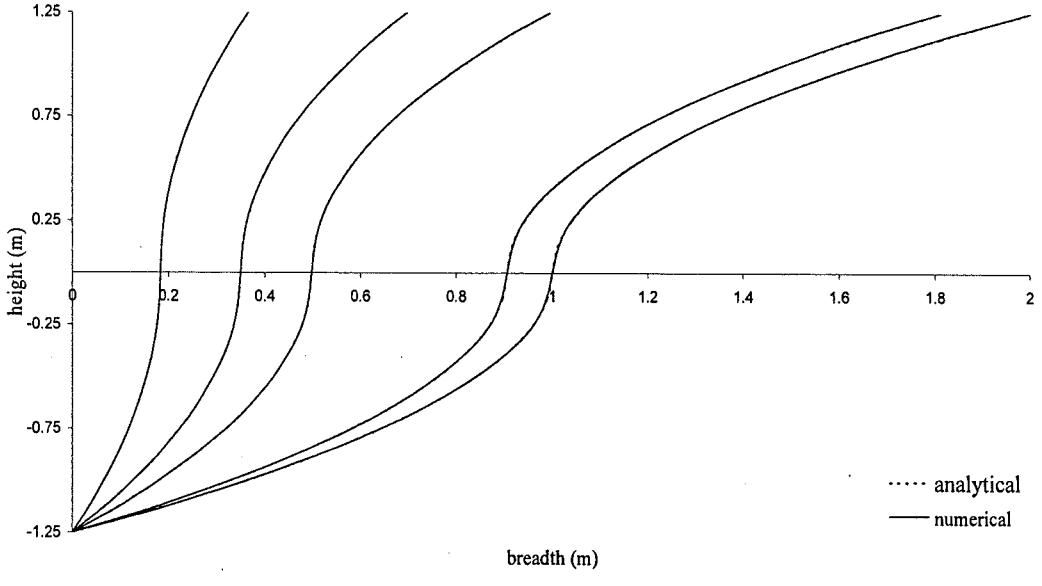

Figure 5.9: Comparison of offset values for the Wigley hull – input stations defined by 13 points.

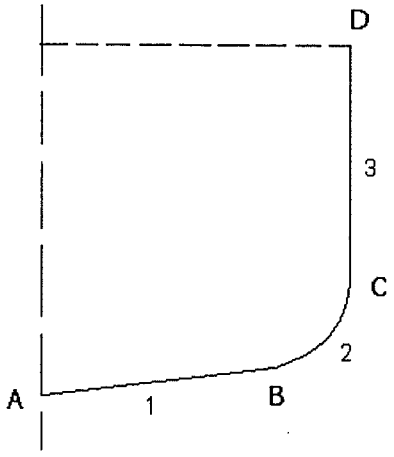

Figure 5.10: A sample cross-section.

5.4 Geometric Description of the Series 60 Hull

Once the steady flow around an analytically defined hull form is computed (see chapter 7), the problem is extended to the simulation of the fluid flow around complex body geometries. A Series 60 hull (Todd (1953)) is chosen for this purpose for which an extensive amount of experimental data are available (see, for example, Toda et al. (1992), Longo et al. (1993), Longo and Stern (1996), Stern et al. (1996), Subramani et al. (2000)).

In the numerical method, the boundary conditions are applied on the instantaneous positions of the surfaces. Therefore, the discretisation of the Series 60 hull (see figure 5.11) has to be repeated at each time step in accordance with the wave elevations along the hull.

Wave elevations ($\eta = z(x, y)$) along the hull are known at each time step once the kinematic free surface boundary condition is integrated with respect to time. Hence, it is possible to calculate the y-ordinate of a point on the hull surface corresponding to the known wave elevation provided that the hull surface can be described by an analytical or a mathematical expression. Since the former cannot be established for the Series 60 hull, a mathematical expression is required to define its body surface.

With the experience gained from sections 5.2 and 5.3, a discretisation algorithm is constructed using B-splines to describe the geometry of the Series 60 hull.

Prior to the flow simulation, the hull is defined up to its deck for reasons that will be mentioned later. At the first step of the flow simulation the x, y and z coordinates of all data points on the hull surface are known. Consequently, a B-spline surface representation can be obtained by substituting the known data points into equation 5.6 and computing the unknown vertices of the defining polygon net $B_{i,j}$. This polygon net

along with the knot vectors and hence the basis functions define a B-spline surface as given in equation 5.4 (see figure 5.12). Once the hull surface is defined the B-spline expression is differentiated to obtain the normal vectors.

At consequent time steps a problem arises due to the vertical displacement of the free surface control points that follow the wave elevation. Accordingly, the B-spline representation obtained in a previous time step is no longer valid at the current time step. Therefore, a node-search routine is incorporated into the discretisation algorithm. This routine searches the entire hull surface for the hull point that corresponds to a given wave elevation on the hull with the aid of the B-spline expression (that contains information for the hull surface from keel to depth) computed prior to the flow simulation. Once the entire set of control points are found along the hull/free surface interface, the Series 60 hull is re-discretised and the normal vector values are updated.

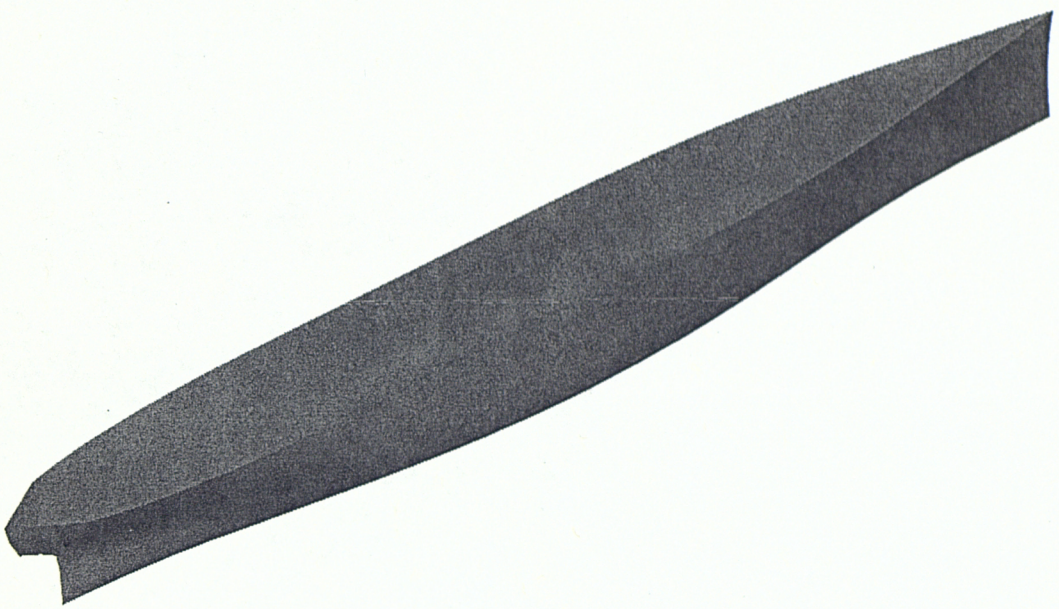

Figure 5.11: A rendered image of the Series 60 hull - $C_B = 0.60$.

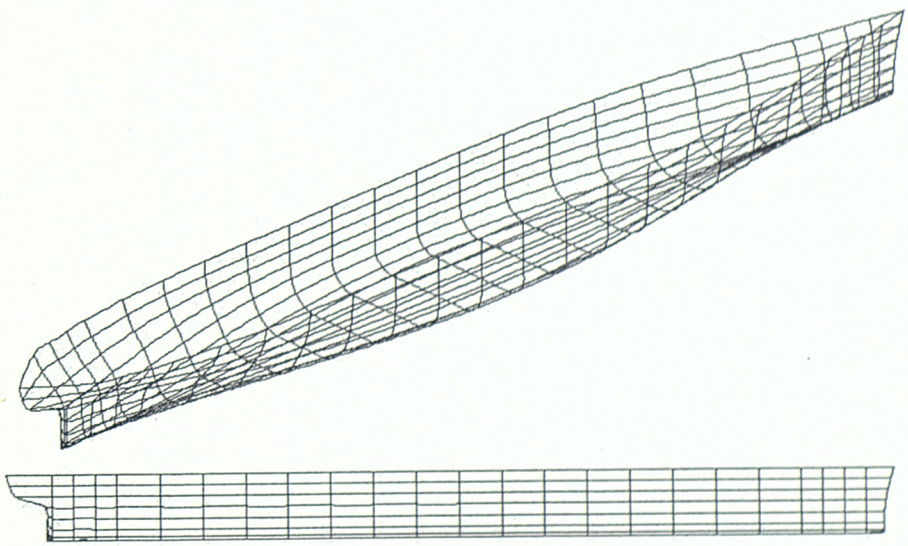

Figure 5.12: Discretisation of the Series 60 hull - $C_B = 0.60$.

6. A SIMPLE APPLICATION OF THE RANKINE SOURCE METHOD

Before progressing to the complex three-dimensional flow problem, the desingularised Rankine source method is applied to the solution of two-dimensional flow around a body submerged in an infinite fluid.

A circular cylinder is chosen to represent the submerged body, for which an analytical solution is available (see, for example, Anderson (1991)).

The circular cylinder (figure 6.1) moves with a speed of U in the $-x$ direction in an inviscid and incompressible fluid of constant density and the fluid motion is irrotational. This problem is equivalent to the case where the submerged body is fixed and the incoming flow speed is U.

The continuity of mass is satisfied by Laplace's equation in the fluid domain,

$$\nabla^2\Phi = 0. \tag{6.1}$$

A body boundary condition is required to ensure that the fluid does not penetrate the body surface; thus,

$$\vec{n}\cdot\nabla\Phi = 0 \quad \text{on } S_B. \tag{6.2}$$

Rankine point sources are placed inside the cylinder, which satisfy Laplace's equation and the radiation condition at infinity. The total velocity potential is decomposed into the free stream and perturbation potentials,

$$\Phi = Ux + \phi, \tag{6.3}$$

where ϕ is the summation of the contributions from a total of N two-dimensional Rankine point sources, i.e.

$$\phi = \sum_{i=1}^{N} \sigma_i G(\vec{x}_j, \vec{\xi}_i) . \tag{6.4}$$

Equations 6.3 and 6.4 are substituted into the body boundary condition (equation 6.2) to solve for the unknown source strengths; namely,

$$\sum_{i=1}^{N} \sigma_i \vec{n}_j \cdot \nabla G(\vec{x}_j, \vec{\xi}_i) = -Un_1 \quad \text{on } S_B . \tag{6.5}$$

Equation 6.5 is applied at N collocation points on the body surface resulting in a linear system of equations of order $N \times N$. Following the solution for the source strengths and the determination of fluid velocities, the pressure on the cylinder's surface is obtained by Bernoulli's equation.

The surface pressure coefficient over a circular cylinder in an ideal fluid is given by (McCormick (1979))

$$C_P = \frac{p}{0.5\rho U^2} = 1 - 4\sin^2\theta , \tag{6.6}$$

where θ is the polar distance of a point from the x-axis. The predicted pressure coefficients are compared with the theoretical values obtained using equation 6.6 and shown in figures 6.2 to 6.5.

Figure 6.2 illustrates the results that are obtained using 10 source/collocation points, whereas for figures 6.3, 6.4 and 6.5 the body is defined by 25, 50 and 100 points respectively. The desingularisation distance l_d in these cases is $0.2r$, where r is the radius of the cylinder. Since pressure distributions over the top and bottom halves of the cylinder are equal, collocation points are distributed on the top half only.

In general, the numerical calculations agree well with the analytical solution. However, there is a clear disagreement at the top of the cylinder ($\theta \approx 90^\circ$), where the velocity of the fluid reaches its highest value (consequently, the pressure value is at its lowest).

Increasing the desingularised distance by a factor of 2, the numerical predictions get much closer to the theoretical values as shown in figures 6.6 to 6.9.

As seen from equations 6.1 to 6.5, the solution presented above is not time-dependent. The results are obtained without any iteration or time-stepping. On the other hand, it is also possible to accelerate the cylinder from rest to its steady speed U_s and hence establish a time-dependent formulation, which is similar to the one that is used for the three-dimensional problem presented in chapters 7 and 8. In this case, equation 6.5 is rewritten as

$$\sum_{i=1}^{N} \sigma_i \vec{n}_j \cdot \nabla G(\vec{x}_j, \vec{\xi}_i) = -U(t) n_1 , \tag{6.7}$$

where $U(t)$ changes from 0 to U_s.

A parallel trend is observed for the time-domain solution compared to the time-independent one. This is illustrated in figure 6.10, where the velocity of a collocation point on the body surface that is positioned at $\theta = 81^\circ$ is plotted against the free stream velocity for varying desingularisation distance. The numerical predictions get much closer to the analytical calculations when the desingularisation distance is equal to $0.4r$, analogous to the time-independent solution discussed above.

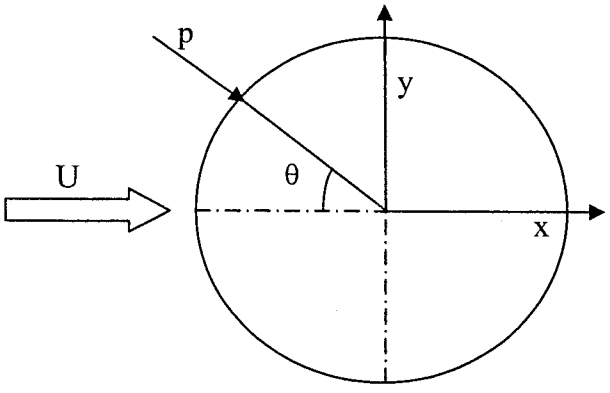

Figure 6.1: Two-dimensional flow around a circular cylinder.

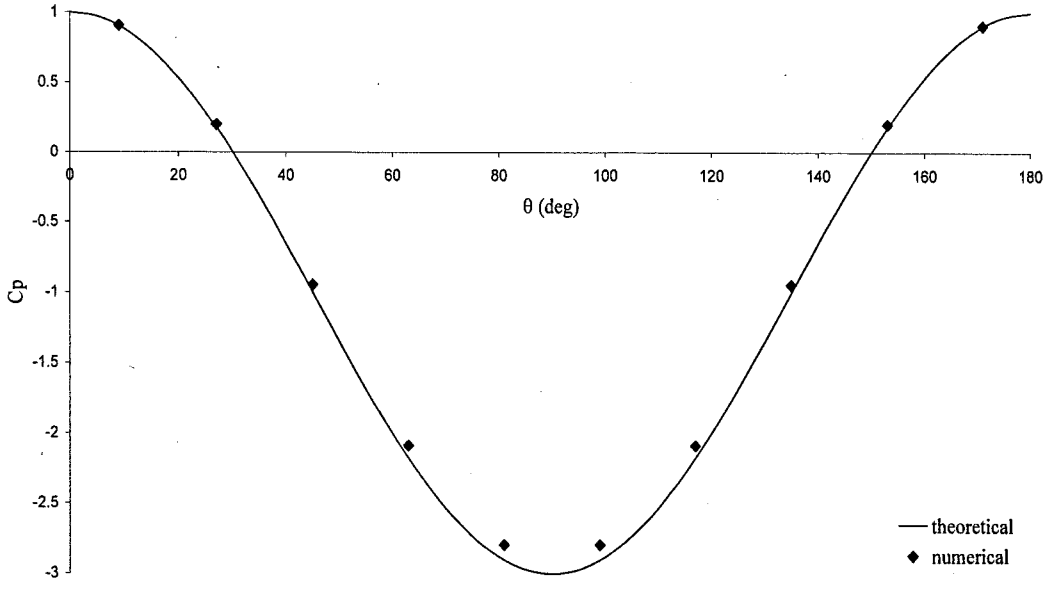

Figure 6.2: Pressure distribution over the cylinder for 10 point sources - $l_d = 0.2r$.

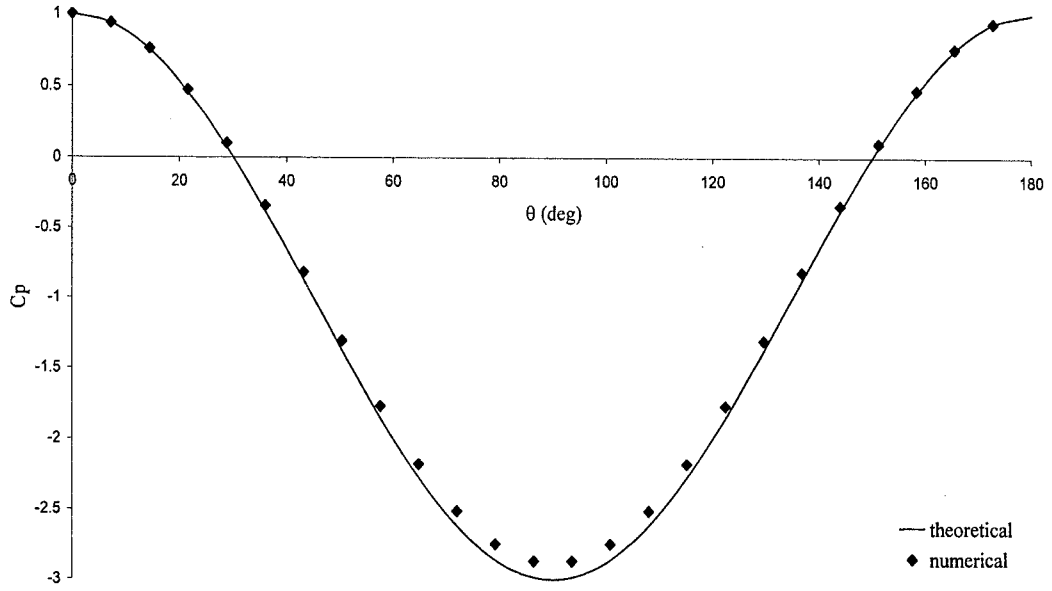

Figure 6.3: Pressure distribution over the cylinder for 25 point sources - $l_d = 0.2r$.

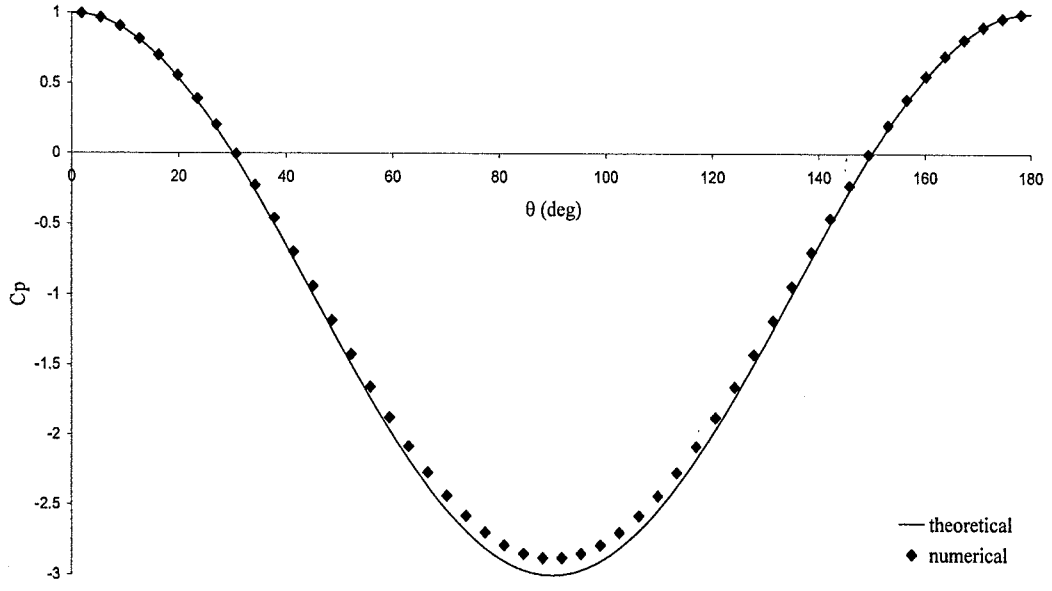

Figure 6.4: Pressure distribution over the cylinder for 50 point sources - $l_d = 0.2r$.

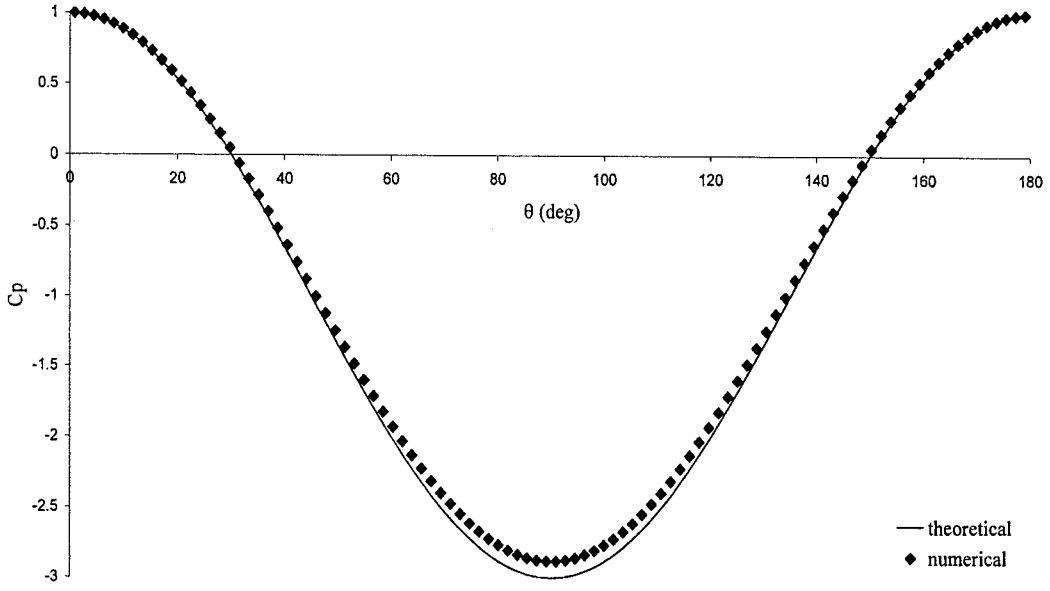

Figure 6.5: Pressure distribution over the cylinder for 100 point sources - $l_d = 0.2r$.

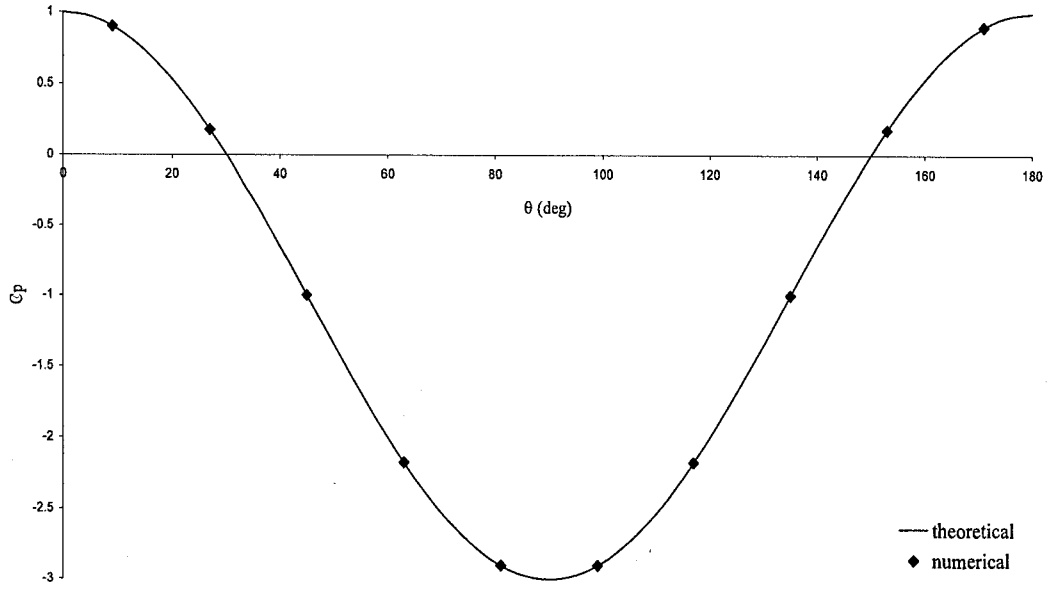

Figure 6.6: Pressure distribution over the cylinder for 10 point sources - $l_d = 0.4r$.

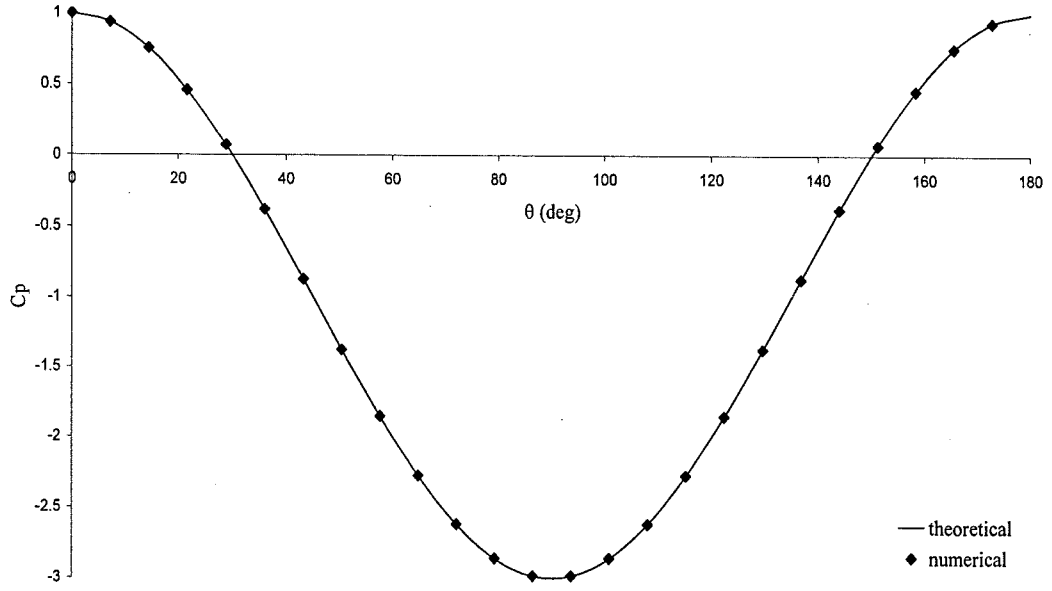

Figure 6.7: Pressure distribution over the cylinder for 25 point sources - $l_d = 0.4r$.

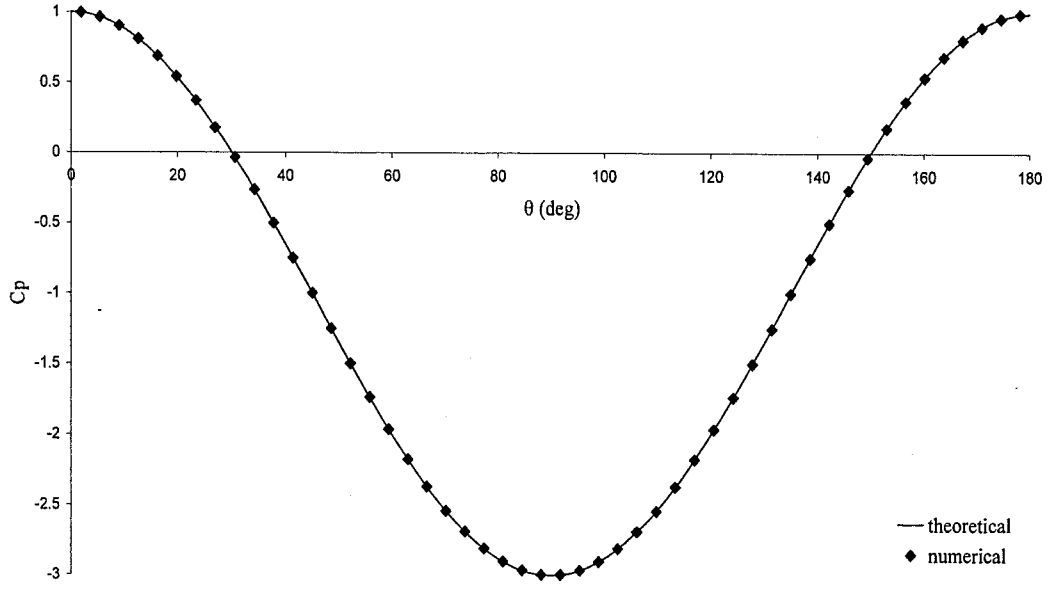

Figure 6.8: Pressure distribution over the cylinder for 50 point sources - $l_d = 0.4r$.

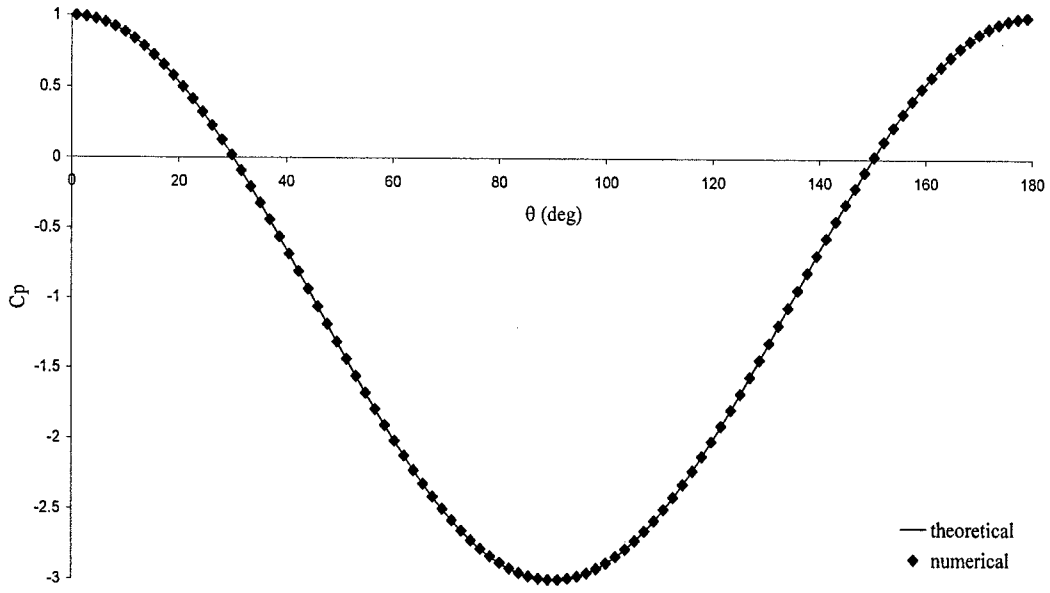

Figure 6.9: Pressure distribution over the cylinder for 100 point sources - $l_d = 0.4r$.

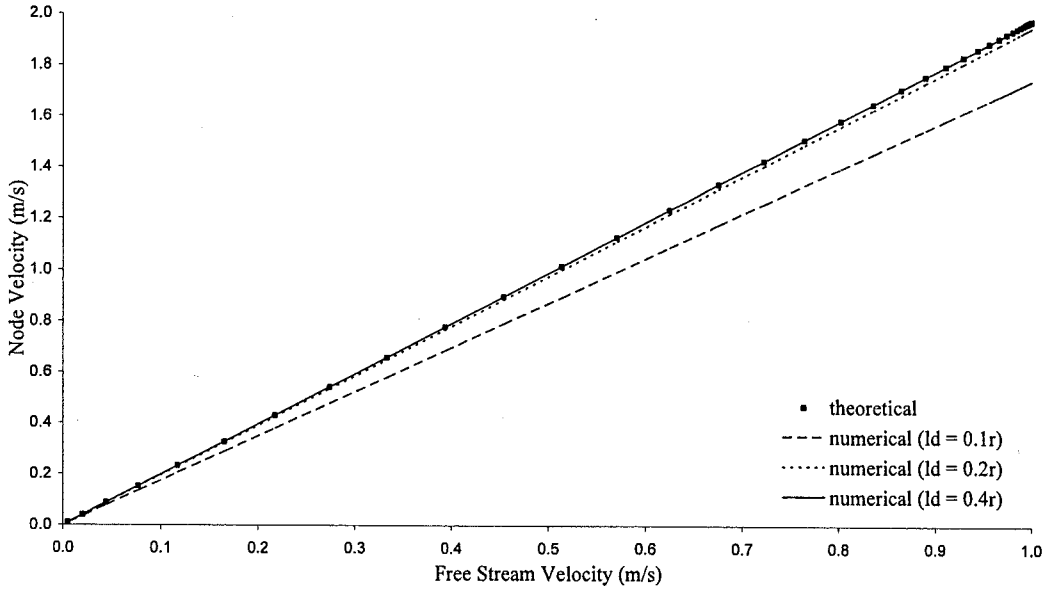

Figure 6.10: Comparison of the theory with the time-domain solution for varying desingularisation distances.

7. SIMULATION OF THE STEADY FLOW AROUND A WIGLEY HULL

The desingularised Rankine source method is adopted for the solution of the steady flow around a Wigley hull travelling in an initially undisturbed free surface. In this chapter, the numerical algorithm that is implemented for the solution is discussed in detail and corresponding results are presented.

All numerical simulations presented in this study are performed on a PC with a Pentium 4 processor running at a clock speed of 2.53 GHz.

7.1 Discretisation of the Body Surface

The surface of the Wigley hull is analytically defined, as given by equation 5.1. The Wigley hull that is used for the simulation has principal ratios of $L/B=10$ and $B/T=1.6$.

At each time step collocation points, on which the boundary conditions are imposed, are placed on the body surface in agreement with equation 5.1.

Rankine point sources are located inside the hull in the normal direction. The normal distance between the collocation and source points (the desingularisation distance) is defined as

$$l_h = A^{1/4} d_h, \tag{7.1}$$

where l_h is the desingularisation distance, d_h is the desingularisation coefficient for the hull and A is approximately the area defined by four adjacent collocation points (see Cao et al. (1991)).

For a particular value of d_h, equation 7.1 ensures that the desingularisation distance is larger for a coarse computational grid and smaller for a fine mesh. The desingularisation coefficient d_h is set to 1.0 at the initial stages of testing and then adjusted until the algorithm converges to a steady-state solution. Once the upper and lower bounds are found for d_h, the results are not very sensitive to the changes in d_h within those limits (see figures 7.2 and 7.6). See Lalli (1997) for an investigation into specification of the criteria related to the choice of the optimum desingularisation distance and the effects of the desingularisation distance on the accuracy and stability of a numerical solution.

7.2 Discretisation of the Free Surface

As a result of the chosen free surface conditions that will be discussed in section 7.4, it is not necessary to discretise the free surface at each time step. Additionally, if the Rankine point sources are placed vertically above the free surface rather than in the normal direction, the solution of equation 5.7 can be avoided completely and since the $[C]$ matrix in equation 5.7 is of order M^2, where M is the total number of control points on the free surface, the required CPU time will reduce accordingly.

The desingularisation distance for the free surface is given by

$$l_{fs} = A^{1/4} d_{fs}. \tag{7.2}$$

l_{fs} is the vertical distance between free surface field and source points and d_{fs} is the desingularisation coefficient for the free surface.

Similar to the hull boundary discretisation, equation 7.2 is used to change the distance between the control points on the free surface and the Rankine point sources above it in accordance with the grid density. Once again, d_{fs} is initially set to 1.0 and if needed adjusted to achieve a stable solution.

In figure 7.1, the computational grid is plotted with panels for illustrative purposes. In the actual numerical algorithm, only nodes are used to discretise the boundary surfaces.

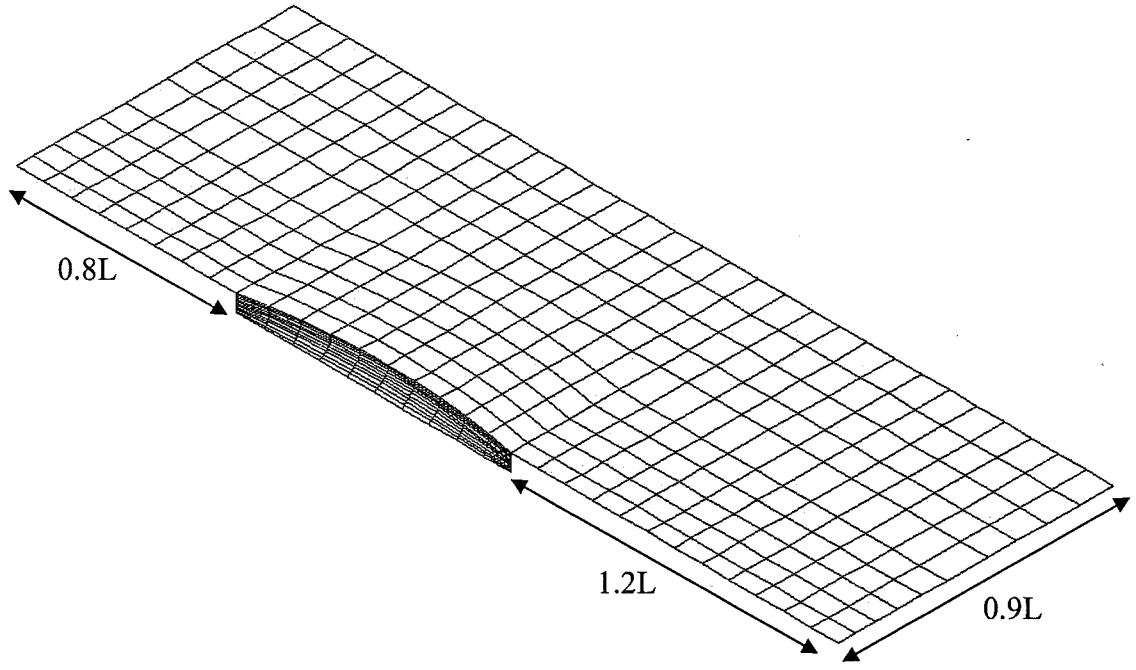

Figure 7.1: Computational grid for the Wigley hull.

7.3 Solution of the Linear Equation System

Although the Lagrange phase of the flow simulation, i.e. time-stepping of the free surface conditions, significantly affects the accuracy of the outcome, the solution of the linear equation system that is obtained in the Euler phase takes up to sixty percent of the overall CPU time (see table 7.1).

Equation 4.14 is solved at each time step to evaluate the unknown source strengths. The influence matrix $[I]$ in equation 4.14 is made up of the boundary and initial conditions applied on all of the surfaces surrounding the fluid domain. Being such a large system, the computational time depends mostly on the efficiency of the solver that is adopted for the solution of equation 4.14.

Three different solvers are tested for the solution of equation 4.14. These three solvers employ the Gauss elimination, LU decomposition and singular value decomposition (SVD) methods (see, for example, Press et al. (1986)). The numerical algorithm is tested with each solver with identical parameters to compare the accuracy and efficiency of the three methods. The computations are carried out for 10 time steps and the corresponding computational times are compared in table 7.2 together with the order of accuracy obtained. In order to compare the accuracy of the three methods, the source matrix $\{s\}$ obtained from the solution of equation 4.14 is substituted into equation 7.3

$$[I]\{s\} = \{b'\}. \tag{7.3}$$

Afterwards, $\{b'\}$ is compared with the original $\{b\}$ matrix. The average of the differences between the elements of these two matrices and hence the order of the accuracy of the solvers are listed in table 7.2.

Although the accuracy of the methods is similar and almost equal to the computer's precision limit, the computing times are significantly different. With the LU

decomposition method, the computing time is reduced by more than fifty percent as compared to the other two methods and therefore it is used for the rest of the computations presented here. The error tolerance for the solution of equation 4.14 is set to 10^{-12} in the algorithm; therefore, when the difference between any two corresponding elements of the matrices $\{b\}$ and $\{b'\}$ reaches this limit, the computations stop.

Hull Grid	Free Surface Grid	Total CPU Time	Grid Generation	Euler Phase	Lagrange Phase	Pressure Integration
(LxT)	(LxT)	(seconds)	% of total CPU Time	% of total CPU Time	% of total CPU Time	% of total CPU Time
11x11	31x11	443	1	44	48	7
11x21	31x11	670	1	48	39	12
11x11	31x21	1480	1	48	46	5
21x11	61x11	2043	1	52	41	6
21x21	61x21	9125	1	61	33	5

Table 7.1: CPU times for different grid densities.

Solution Method	CPU Time (sec)	Accuracy
Gauss Elimination	100	1.E-16
LU Decomposition	45	1.E-16
SVD	125	1.E-16

Table 7.2: Comparison of CPU times and accuracy of different solvers.

7.4 Integration of the Free Surface Boundary Conditions

In the Lagrange phase of the simulation, kinematic and dynamic boundary conditions are defined on the free surface. By integrating these conditions with respect to time, free surface wave elevation and velocity potential values are updated, which are required for the subsequent time step.

For the simulation of steady flow around the Wigley hull, the prescribed velocity is set to $\vec{v} = (0, 0, \partial\eta / \partial t)$, which implies that the horizontal movements of the free surface nodes are constrained and they are only allowed to move in the vertical direction with wave elevation.

The idea behind constraining the horizontal movements is to eliminate the need to discretise the free surface between each time step. Discretising the free surface at each time step increases the total CPU time considerably as discussed in section 7.2.

7.5 Sensitivity to Numerical Parameters

In order to investigate the sensitivity of the algorithm to the changes in the different numerical parameters (e.g. time-step size, hull acceleration, desingularisation distance), the algorithm is tested with different variables and the results are compared with a test case denoted *test-A*. Numerical parameters used for *test-A* are listed in table 7.3, where Δt is the time-step size and α is the hull acceleration parameter as given by

$$U(t) = U_s\left(1 - e^{-\alpha t^2}\right). \tag{7.4}$$

In addition to the Gaussian acceleration function given in equation 7.4, a linear acceleration function is tested as well (see section 8.5). However, equation 7.4 provides

a smooth acceleration of the ship hull and therefore is more suitable for the present numerical algorithm.

The number of Rankine point sources used for *test-A* is given in table 7.4. The upstream, downstream and side boundaries are positioned $0.8L$, $1.2L$ and $0.9L$ away from the hull respectively (see section 8.5, figures 8.24 to 8.26, for an analysis on the position of the truncated boundaries). The hull is restrained from sinkage and trim. The computations reach a steady state around the 90^{th} time-step in approximately 435 seconds of CPU time.

For the results presented in figures 7.2 to 7.9, all numerical parameters except the one being investigated are kept constant. For instance, the numerical parameters that are used to obtain the results shown in figure 7.5 have the values given in tables 7.3 and 7.4. The only parameter that changes in this particular figure is the hull acceleration parameter. In this manner, it is easier to distinguish the effect of a single numerical parameter on the final result.

In figures 7.2 to 7.5, the time histories of the fluid velocity of a control point on the body surface are plotted for varying values of four numerical parameters; the desingularisation coefficients d_h and d_{fs}, the time-step size Δt and the hull acceleration parameter α.

The effect of hull desingularisation distance is illustrated in figure 7.2, for which the numerical code is run for five different d_h values ranging from 0.1 to 0.8 and $d_h = 0.2$ corresponds to *test-A*. It is clear that increasing the hull desingularisation distance beyond $d_h = 0.4$ does not affect the solution significantly. This is in agreement with Raven's (1998) findings who states that the upper limit of the desingularisation distance is not determined by accuracy but by robustness and the conditioning of the linear equation system.

In figure 7.3, the time histories of the fluid velocity at the same control point are plotted for varying free surface desingularisation distances. With the exception of the case when $d_{fs} = 0.4$, all solutions converge to a similar value.

The effect of time-step size Δt on the numerical solution is demonstrated in figure 7.4, where the solution for $\Delta t = 0.04$ corresponds to *test-A*. When Δt is higher than 0.04, relatively high oscillations are observed in the results even after the hull reaches its steady speed. These oscillations reduce considerably once the time-step size is lowered to 0.04. Essentially, the stability of the numerical scheme depends on the time-step to grid size ratio as revealed by numerical tests (see also section 7.6). Though not mathematically verified in the current study, it is in agreement with the results of a recent stability analysis of a similar numerical model (Buchmann (2001)). For a constant grid size the instabilities die out with decreasing time-step size as shown in figure 7.4.

The hull acceleration parameter α has a less significant effect on the final solution compared to the desingularisation distance coefficients and the time-step size. On the other hand, with a low hull acceleration parameter such as $\alpha = 0.5$ it takes more time for the algorithm to converge to a pseudo-steady solution as illustrated in figure 7.5 and hence the total CPU time increases accordingly. However, as with the time-step size, the oscillations reduce with decreasing α value.

The investigation of the sensitivity of the algorithm to the changes in the numerical parameters discussed above is repeated for a control point on the free surface and presented through figures 7.6 to 7.9. A similar trend is observed in the results for the control point on the free surface as compared to the one on the body surface. The convergence is less satisfactory, especially in figure 7.7, where the free surface desingularisation distance is altered. Once again, oscillations are present in the results for large values of time-step (see figure 7.8).

The oscillations present in the figures may be explained by short-wave instabilities (see, for example, Longuet-Higgins and Cokelet (1976)) and/or non-uniformity effects in the spatially discretised model (Buchmann (2001)). The former is due to short-length waves which cannot be resolved by the computational grid. In order to resolve these components denser grids are required. This in turn means low time-step sizes (and hence higher CPU times) if one is to keep the time-step to grid size ratio constant. Since the results converge (at least temporarily) to a steady solution, these instabilities do not pose a problem for the current analysis. However, in worst cases, the instabilities grow exponentially in time and eventually cause the computations to stop. Therefore, for a successful extension of the current method to the unsteady flow problem (which requires a much longer simulation time) a remedy must be sought that deals with these instabilities (see section 8.6).

L (m)	20	**d_h**	0.2
B (m)	2	**d_{fs}**	0.8
T (m)	1.25	**Δt (s)**	0.04
F_n	0.25	α	0.9

Table 7.3: Numerical parameters used for *test-A*.

	Hull Grid	**Free Surface Grid**
(LxT)	11x11	31x11
Total	121	341

Table 7.4: The number of Rankine sources used for *test-A*.

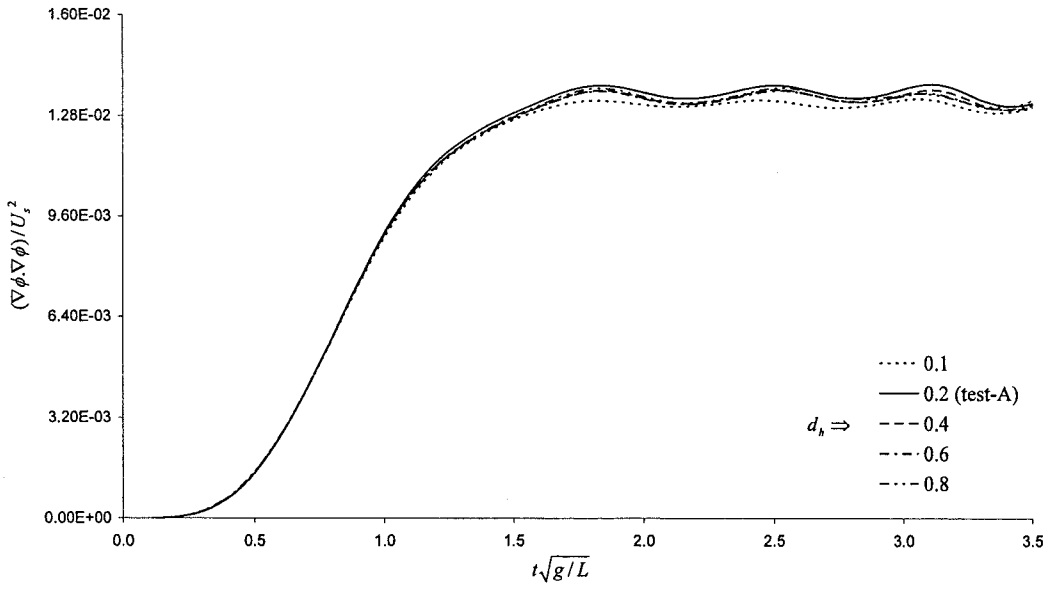

Figure 7.2: The effect of hull desingularisation distance on the numerical solution – control point on the hull surface.

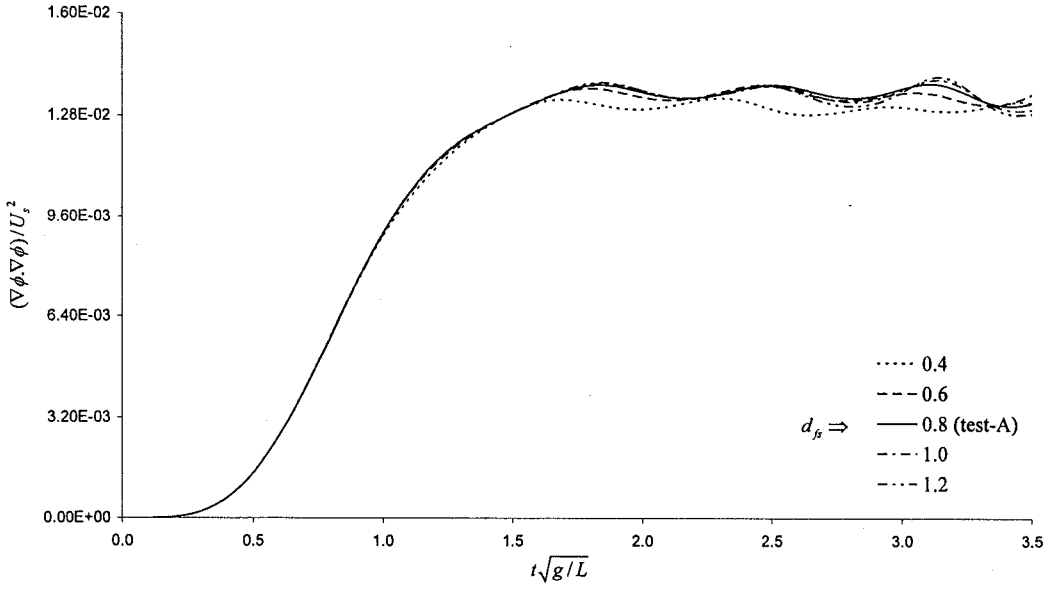

Figure 7.3: The effect of free surface desingularisation distance on the numerical solution – control point on the hull surface.

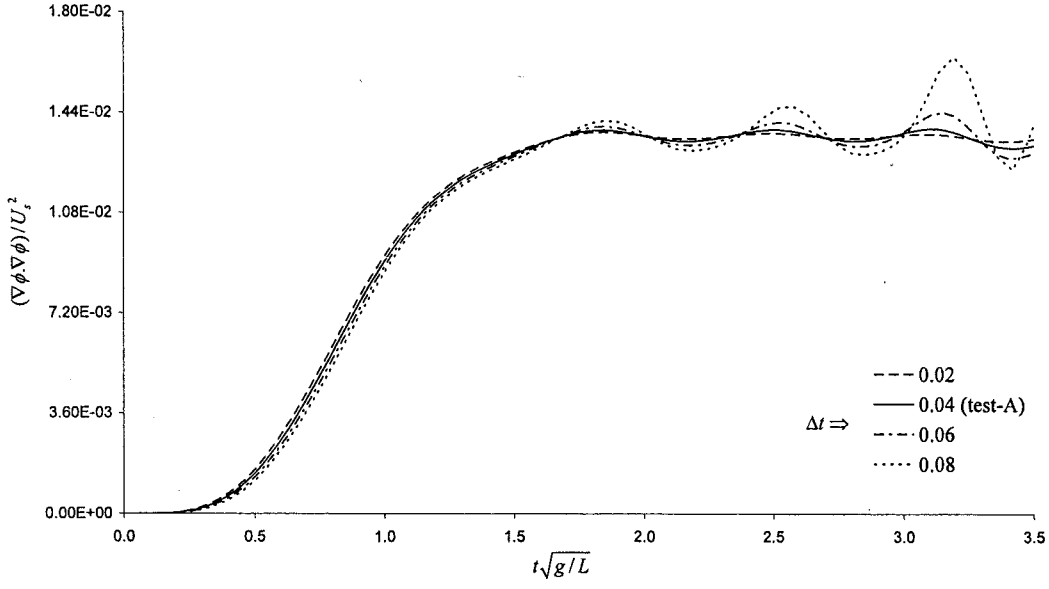

Figure 7.4: The effect of time-step size on the numerical solution – control point on the hull surface.

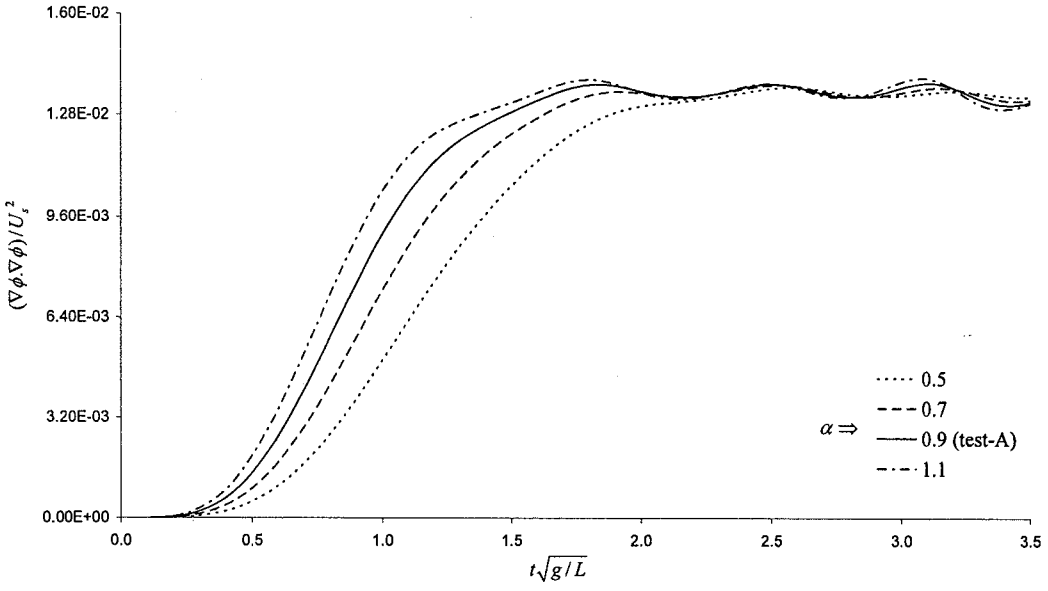

Figure 7.5: The effect of hull acceleration parameter on the numerical solution – control point on the hull surface.

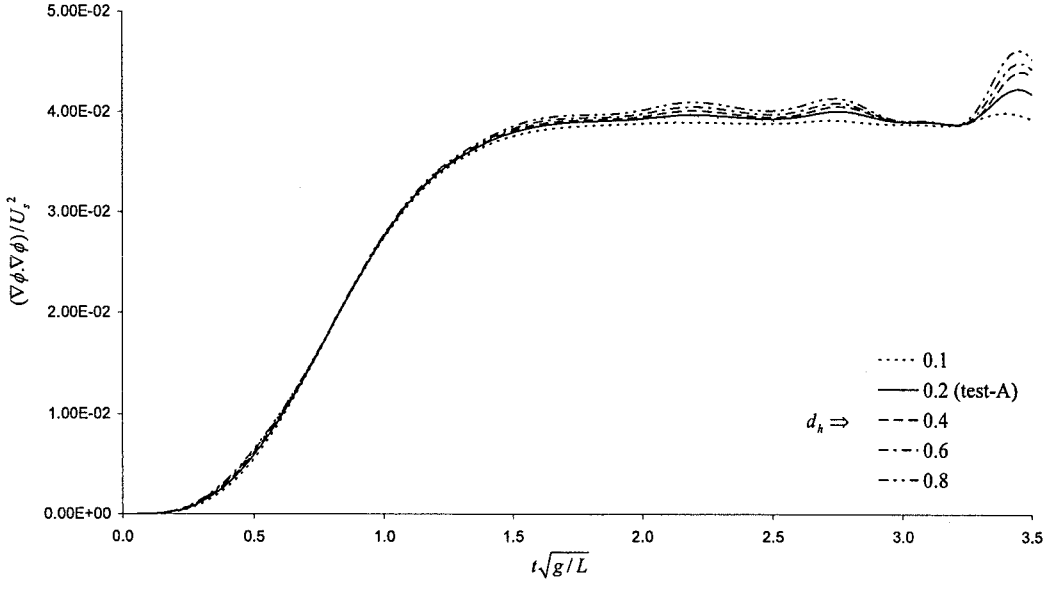

Figure 7.6: The effect of hull desingularisation distance on the numerical solution – control point on the free surface.

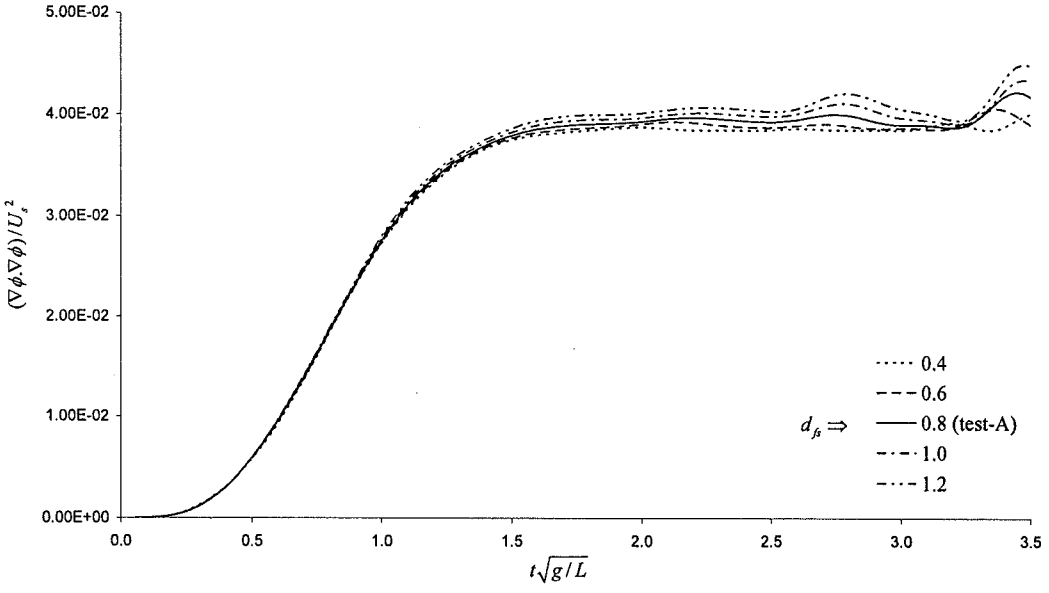

Figure 7.7: The effect of free surface desingularisation distance on the numerical solution – control point on the free surface.

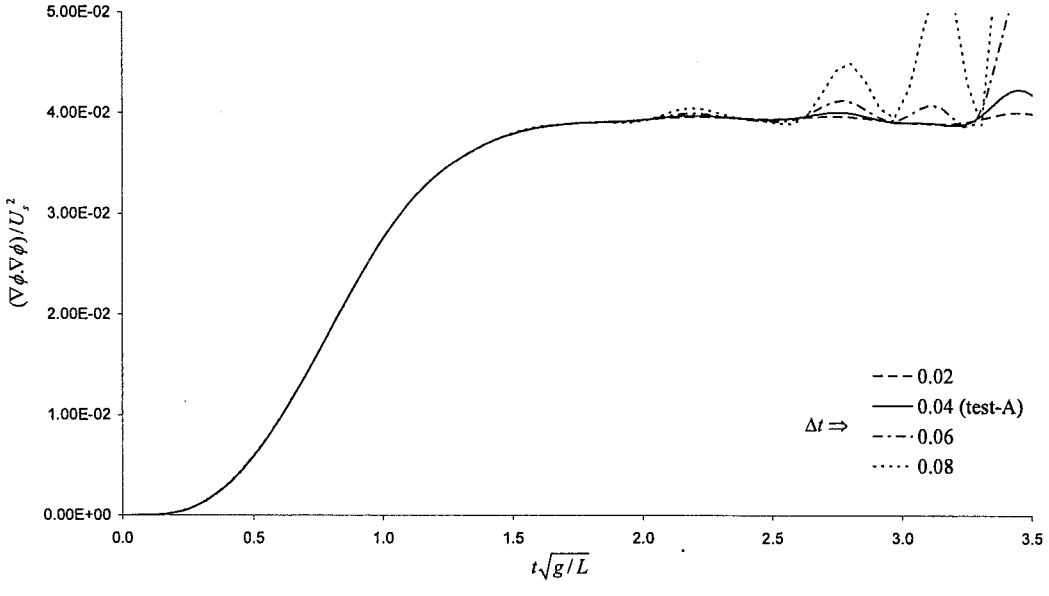

Figure 7.8: The effect of time-step size on the numerical solution – control point on the free surface.

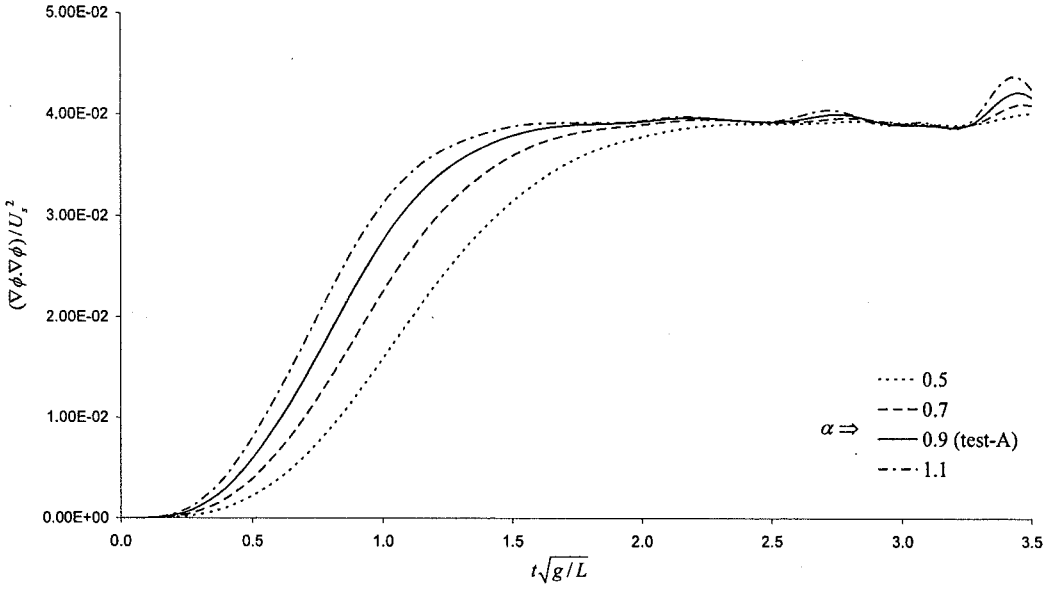

Figure 7.9: The effect of hull acceleration parameter on the numerical solution – control point on the free surface.

7.6 Wave Profile along the Wigley Hull

The wave profile along the Wigley hull for $F_n = 0.25$ is compared to the measurements of Noblesse and McCarthy (1983) in figure 7.10. The wave profile is slightly different from that presented in Diken et al. (2004) (see appendix) due to some minor modifications in the algorithm and use of different numerical parameters. In this case, the results are obtained by setting $\Delta t = 0.04$ and $\alpha = 0.11$. Additionally, the wave profiles are illustrated for Froude numbers 0.267, 0.289 and 0.316 in figures 7.11 to 7.13, where the simulations are run with numerical parameters identical to those used for $F_n = 0.25$.

The computational grid that is used to obtain the wave profiles shown through figures 7.10 to 7.13 consists of 11×11 control points on the hull surface and 31×11 on the free surface. Results are also obtained for a finer mesh that has 21×11 control points on the hull surface and 61×21 on the free surface. The wave profile along the hull for this particular mesh is plotted in figure 7.14 for a Froude number of 0.25.

In figure 7.15, the time histories of the wave elevation of a control point that is positioned on the hull/free surface interface at $x = 0.$ are plotted for two different mesh sizes. The coarse grid has a total of 462 Rankine sources whereas the finer mesh is defined by 1512 sources. The control point oscillates about a mean value (indicated by straight lines in the figure) once the hull reaches its steady speed. Due to this oscillatory behaviour, mean values are calculated once the flow reaches a pseudo-steady state and plotted for the wave elevations presented in figures 7.10 to 7.14.

In figure 7.15, for the same time-step size of 0.01 the oscillations are larger for the finer mesh. As mentioned before, increasing the grid density while keeping the time-step size constant affects the stability of the numerical scheme. When the grid density is increased, the time-step size should be lowered to ensure a stable solution. For instance,

when the time-step size is lowered to 0.008, the amplitudes of the oscillations for the finer mesh reduce considerably as shown in figure 7.15.

The wave profile predictions along the Wigley hull agree well with the measurements – especially at the bow and stern regions. However, there exist some discrepancies around the midship section. The discrepancies are larger at low Froude numbers, which is expected since the same computational grid is used to obtain the results plotted in figures 7.11 to 7.13. A relatively fine discretisation is required at low Froude numbers in order to guarantee an accuracy comparable to that obtained for a higher Froude number as evident from the comparison of figures 7.10 and 7.14, where an almost three times denser grid is used for the latter.

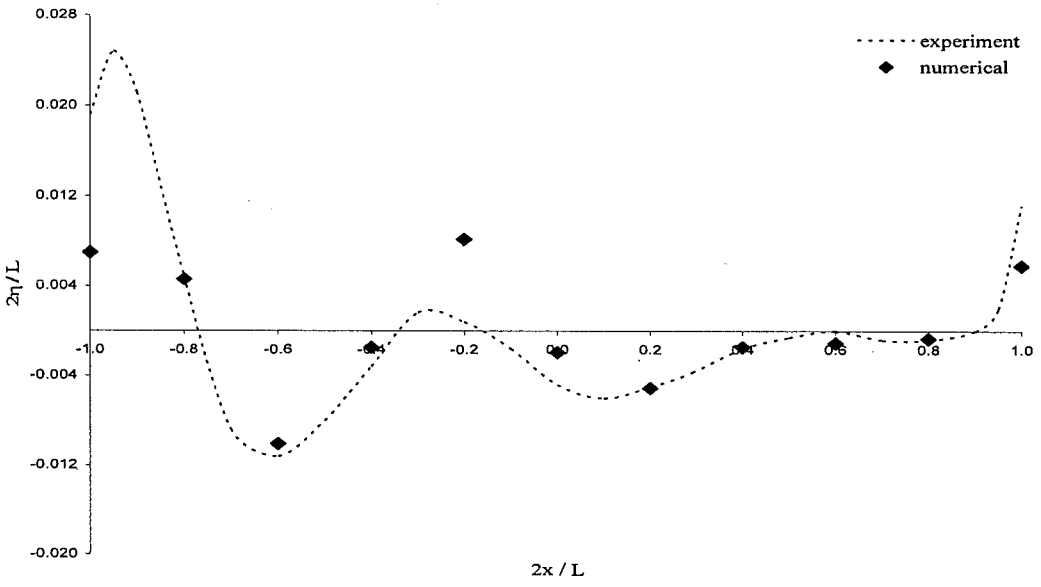

Figure 7.10: Wave profile along the Wigley hull - $F_n = 0.25$.

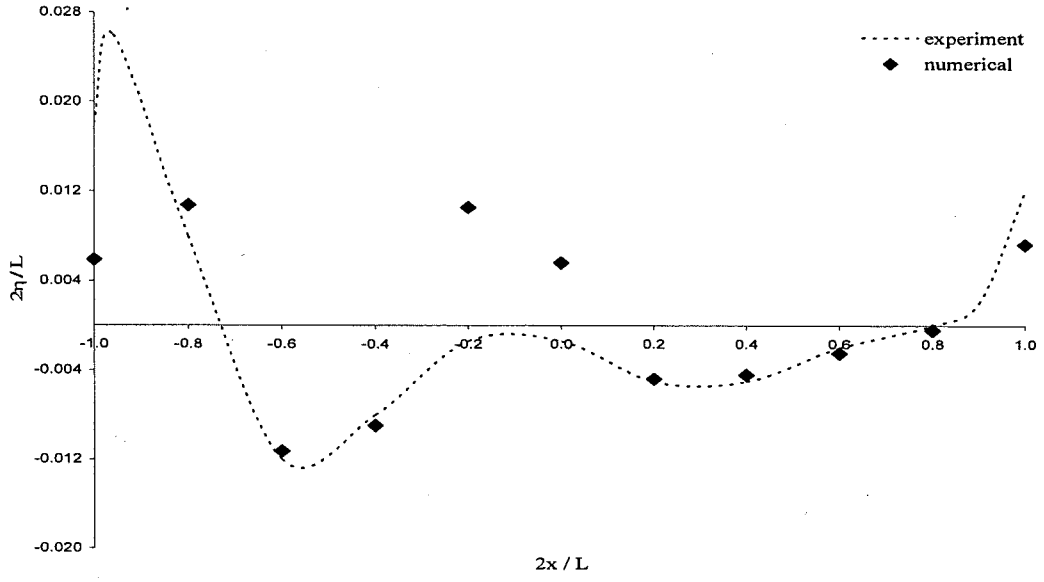

Figure 7.11: Wave profile along the Wigley hull - $F_n = 0.267$.

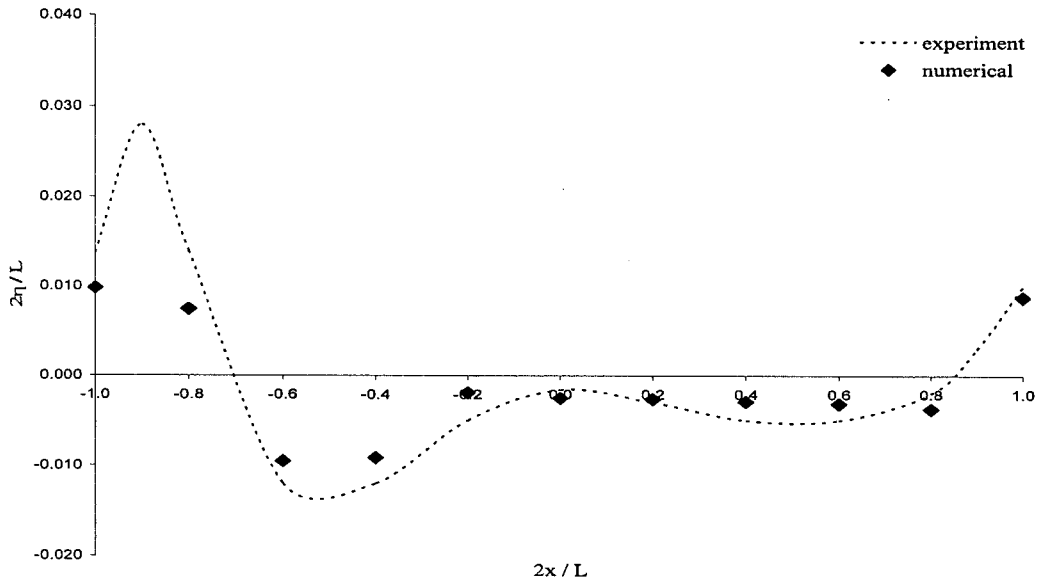

Figure 7.12: Wave profile along the Wigley hull - $F_n = 0.289$.

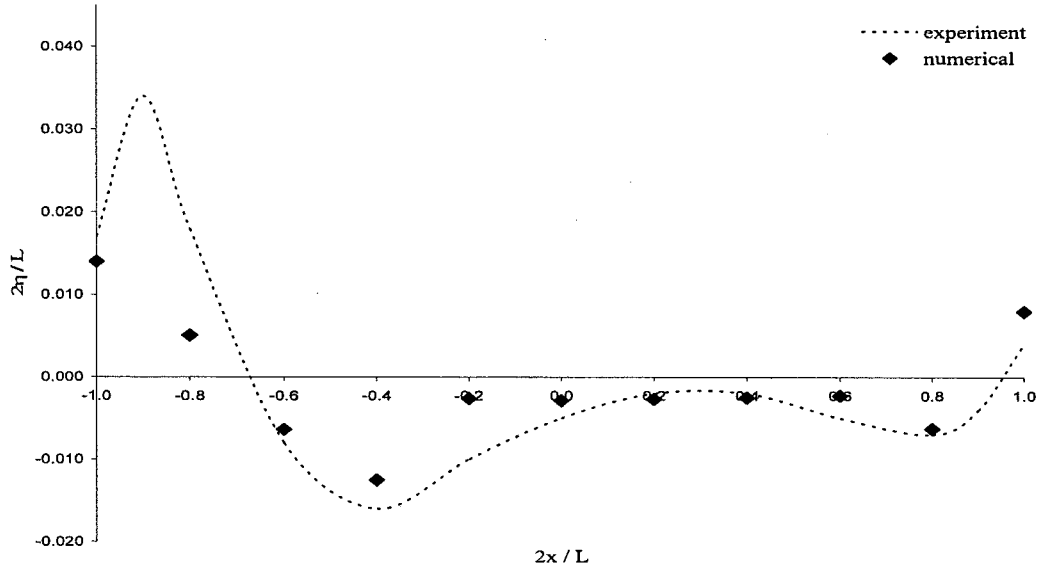

Figure 7.13: Wave profile along the Wigley hull - $F_n = 0.316$.

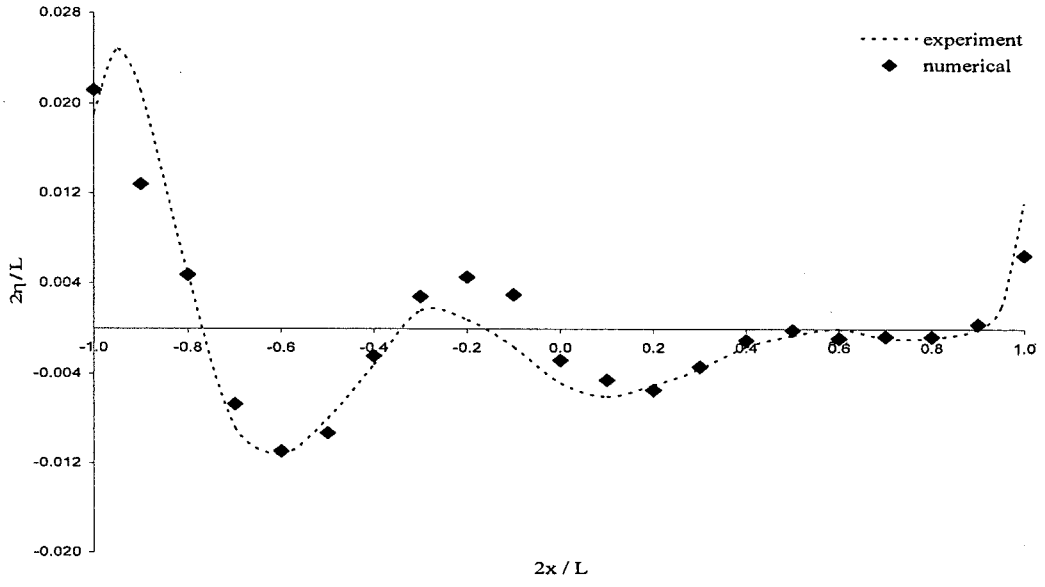

Figure 7.14: Wave profile along the Wigley hull for the finer mesh - $F_n = 0.25$, $\Delta t = 0.01$, $\alpha = 0.11$.

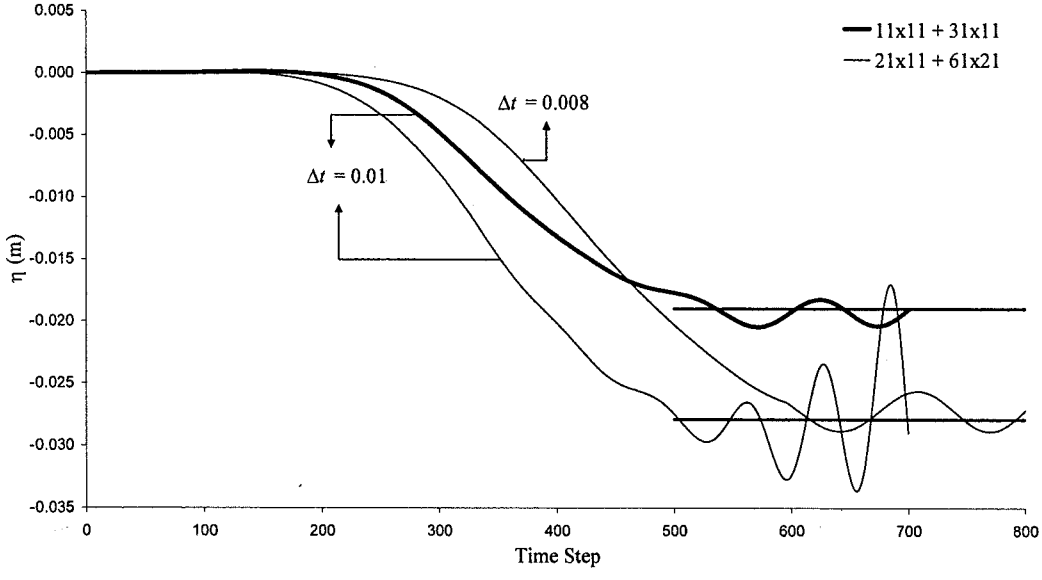

Figure 7.15: Time histories of the wave elevation of a control point for two different mesh sizes - $F_n = 0.25$.

7.7 Forces and Moments on the Hull

In order to calculate the forces and moments acting on the hull surface, the fluid pressure, p, has to be computed at every time step. A form of Bernoulli's equation (hence a similar one to the dynamic free surface condition) is used for this purpose; namely,

$$\frac{-p}{\rho} = \frac{\delta\phi}{\delta t} + gz + \frac{1}{2}\nabla\phi\cdot\nabla\phi + U(t)\frac{\partial\phi}{\partial x} + \vec{v}_h\cdot\nabla\phi \quad \text{on } S_H, \tag{7.5}$$

where $\frac{\delta}{\delta t}$ is the time-derivative following a node on the body surface that has a velocity $\vec{v}_h$. Assuming that the calculations are at the n^{th} time step, the fluid pressure can be computed at the $(n-1)^{th}$ step as given in equation 7.6, provided the hull is restrained from sinkage and trim.

$$\begin{aligned} p^{n-1} = &-\rho\left(\frac{\delta\phi}{\delta t}\right)^{n-1} - \rho g z^{n-1} - \frac{1}{2}\rho\left(\nabla\phi\cdot\nabla\phi\right)^{n-1} \\ &-\rho\left(U\frac{\partial\phi}{\partial x}\right)^{n-1} - \rho(\vec{v}_h\cdot\nabla\phi)^{n-1} \quad \text{on } S_H. \end{aligned} \tag{7.6}$$

The time derivative of the velocity potential in equation 7.6 and the velocity of the hull nodes are calculated with a central-differencing scheme (see, for example, Greenberg (1998)).

Once equation 7.5 is solved, hydrodynamic forces and moments acting on the hull are computed by integrating the fluid pressure on the wetted surface of the hull. The generalised force is given as

$$F_j = \iint p n_j dS \quad \text{on } S_H, \tag{7.7}$$

Where n_j is the generalised unit normal defined as

$$\begin{aligned} (n_1, n_2, n_3) &= \vec{n} \\ (n_4, n_5, n_6) &= \vec{x}\times\vec{n} \end{aligned}$$

Equation 7.7 yields the hydrodynamic forces for $j = 1,2,3$ and the moments about the body-fixed axis for $j = 4,5,6$.

The force in the x direction, F_1, provides the wave-making resistance of the hull. However, F_1 has to be corrected by subtracting the hydrostatic pressure acting below the calm water line. The hydrostatic pressure force in the x direction should be zero over the area under the calm water surface. However, it is non-zero in most if not all cases due to the discretisation errors in numerical methods. Therefore, once the total fluid pressure is integrated over the actual wetted hull surface, the hydrostatic pressure force acting below the calm water line is subtracted from F_1 in order to reduce these discretisation errors.

In figure 7.16, the wave resistance coefficient of the parabolic hull form is compared with the experimental measurement for $F_n = 0.25$. The time history of the total wave resistance coefficient is divided into five components as numbered in the graph and described in the table below.

Label	Term	Definition
1	$\frac{\delta\phi}{\delta t}$	Time derivative of the velocity potential
2	$U\frac{\partial\phi}{\partial x}$	Linear pressure term
3	gz	Nonlinear gravity term
4	$\frac{1}{2}\nabla\phi\cdot\nabla\phi$	Velocity-squared term
5	$\vec{v}_h\cdot\nabla\phi$	Correction for the moving nodes

The experimental measurement (see Noblesse and McCarthy (1983)) for the wave resistance coefficient is indicated by a straight line and the numerical prediction is denoted as *Total* (C_w), which is the sum of the five components mentioned above.

The largest contribution to the total resistance value comes from the linear pressure term indicated by number 2 in the figure, which is directly related to the forward motion of the hull. The time derivative of the velocity potential slowly decays to zero with time and the correction for the moving nodes is very close to zero throughout the calculations.

For the results in figure 7.16 the following numerical parameters are chosen: $d_h = 0.8$, $d_{fs} = 1.0$, $\Delta t = 0.02$, $\alpha = 0.11$. The computational grid consists of 462 control points distributed on one symmetric half of the hull.

The resistance computations for $F_n = 0.25$ are repeated keeping all the numerical parameters the same except the time-step size (Δt) which is reduced to 0.01 and the corresponding results are presented in figure 7.17. As expected, the time histories for the resistance components closely match those in figure 7.16.

The oscillatory behaviour mentioned previously in sections 7.5 and 7.6 is observed once again in the resistance calculations. The amplitude of the oscillations reduces considerably with low time-step sizes. Therefore, low Δt values were chosen for the calculations presented in figures 7.16 and 7.17 to avoid having to stop the computations once the hull reaches its steady speed.

Results are presented for finer meshes in figures 7.18 and 7.19, for which the computational grids consist of 572 and 902 Rankine point sources respectively. The time-step size has been increased to 0.04 and the hull acceleration parameter is set to 0.9 in order to reduce the required CPU time. This choice resulted in relatively large

oscillations in terms 1 and 3 i.e. the time derivative of the velocity potential and the nonlinear gravity term. Therefore, mean values are calculated and plotted in figures 7.18 and 7.19 for these terms.

The numerical predictions for the wave-making resistance coefficient at $F_n = 0.25$ are plotted in figure 7.20 for four different mesh sizes to examine the grip-dependence of the numerical algorithm. The coarsest grid consists of 462 Rankine point sources, 121 of which are positioned inside the hull surface. The corresponding resistance prediction is significantly higher than the experimental value. For the second grid, 231 sources are placed inside the hull and 341 sources are positioned above the free surface. Although the numerical prediction is still higher than the experimental measurement, it is much closer to the expected value. For the last two meshes, 671 and 1281 free surface sources are used respectively; whereas, the number of hull sources is maintained at 231.

To further investigate the capabilities of the algorithm, the wave-making resistance calculations are carried out for higher Froude numbers. Once again, the total C_w for the Wigley hull travelling with a Froude number of 0.267 is plotted together with its five components and compared with measurements in figures 7.21 to 7.23. Additionally, numerical results that are obtained using different grid densities are shown in figure 7.24. Since there is only a slight increase in the speed of the ship, the results have similar characteristics to those presented for $F_n = 0.25$.

The resistance calculations are then repeated for even higher Froude numbers. In figures 7.25 to 7.29, the wave-making resistance predictions are plotted for the Wigley hull travelling at $F_n = 0.289$ and in figures 7.30 to 7.34 the numerical predictions are presented for $F_n = 0.316$.

The predictions for $F_n = 0.289$ are yet again higher than the measurements as shown in figure 7.29. The results converge to a similar value with the exception of the second

mesh that contains 572 control points. It is supposed that the prediction for the second mesh exhibits an anomaly due to the aspect ratio used for the hull discretisation. The aspect ratio chosen for the other three meshes is closer to unity, whereas for the second mesh 21 control points are used on the transverse direction and the remaining 11 are distributed longitudinally on the hull surface. Since the draught of the ship is much smaller than its length, this discretisation results in very closely positioned control points in the transverse direction. The same anomaly is also present in the predictions for $F_n = 0.316$ for this particular mesh (see figure 7.34).

In figure 7.35, the wave-making resistance predictions for different ship speeds are plotted and compared with measurements and with other numerical methods. These numerical methods are the recent linear time-domain method of Kara and Vassalos (2005), Scorpio's (1997) nonlinear time-domain method and another linear time-domain method of Lin and Yue (1990). The predictions are for the computational grid that is defined by 902 control points. Although the present numerical algorithm yields wave resistance values that are higher than the experimental measurements throughout the speed range examined here, the predictions follow the correct trend and hence the results are at least useful in a comparative sense.

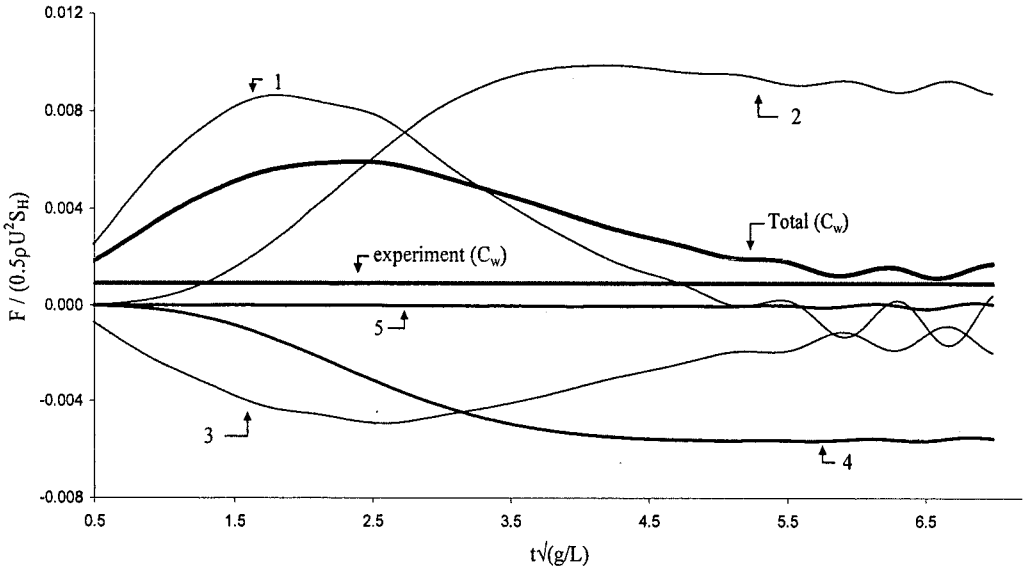

Figure 7.16: Components of the wave resistance coefficient - $F_n = 0.25$, $d_h = 0.8$, $d_{fs} = 1.0$, $\Delta t = 0.02$, $\alpha = 0.11$, 462 Rankine sources.

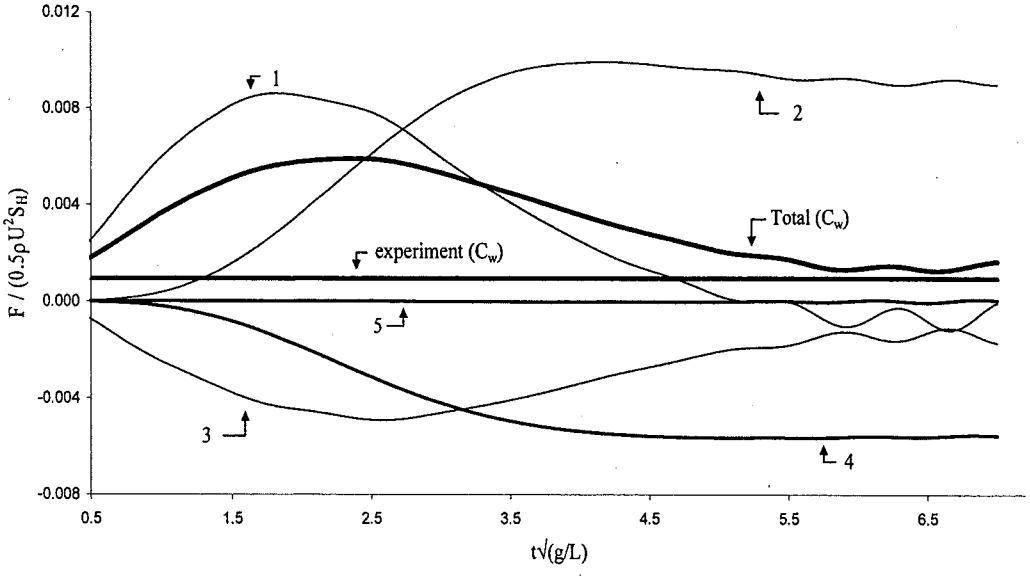

Figure 7.17: Components of the wave resistance coefficient - $F_n = 0.25$, $d_h = 0.8$, $d_{fs} = 1.0$, $\Delta t = 0.01$, $\alpha = 0.11$, 462 Rankine sources.

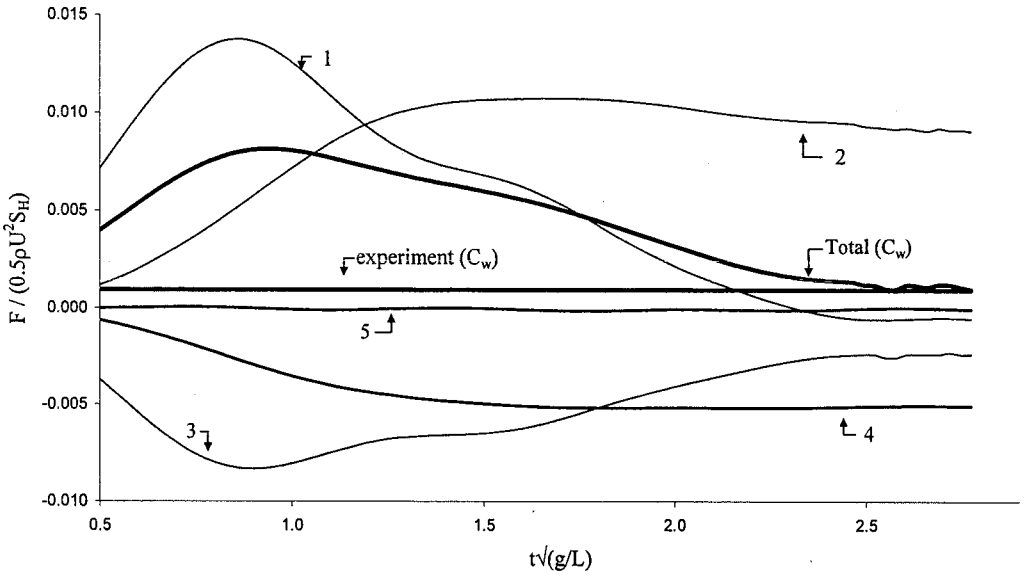

Figure 7.18: Components of the wave resistance coefficient - $F_n = 0.25$, $d_h = 0.2$, $d_{fs} = 0.8$, $\Delta t = 0.04$, $\alpha = 0.9$, 572 Rankine sources.

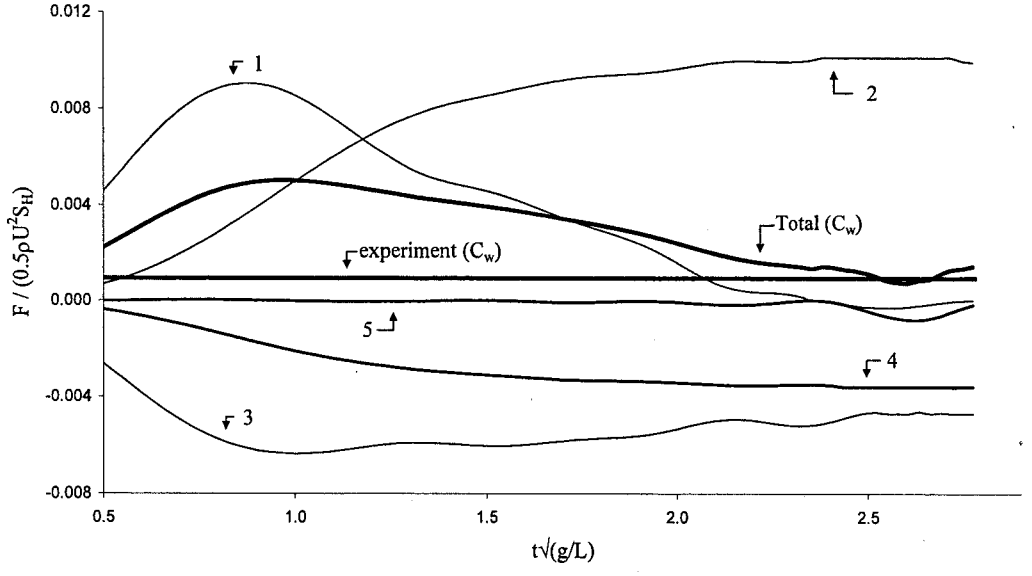

Figure 7.19: Components of the wave resistance coefficient - $F_n = 0.25$, $d_h = 0.2$, $d_{fs} = 0.8$, $\Delta t = 0.04$, $\alpha = 0.9$, 902 Rankine sources.

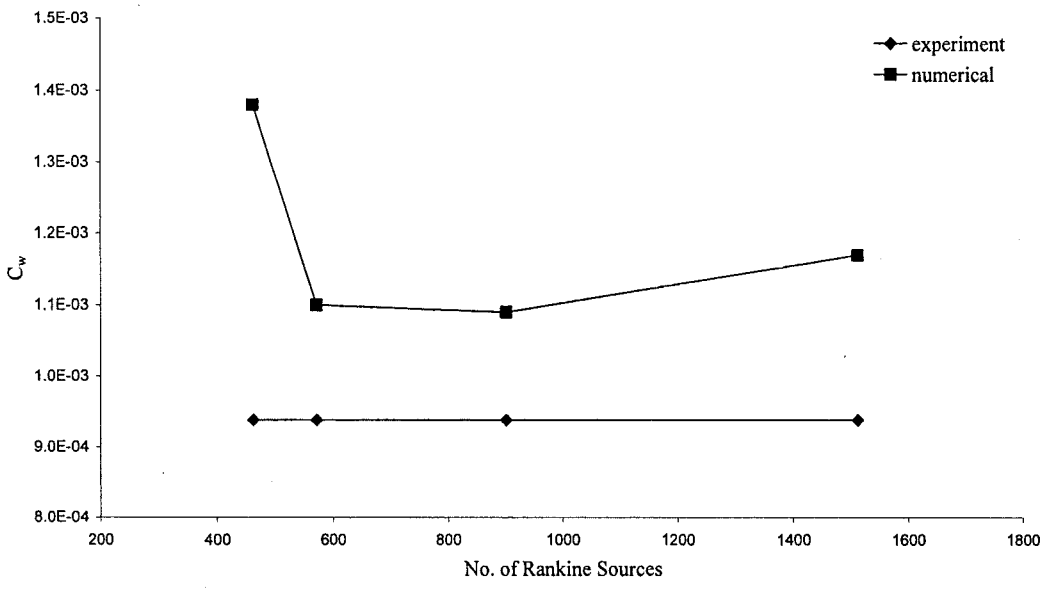

Figure 7.20: Grid-dependence of the numerical predictions for wave-making resistance of the Wigley hull at $F_n = 0.25$.

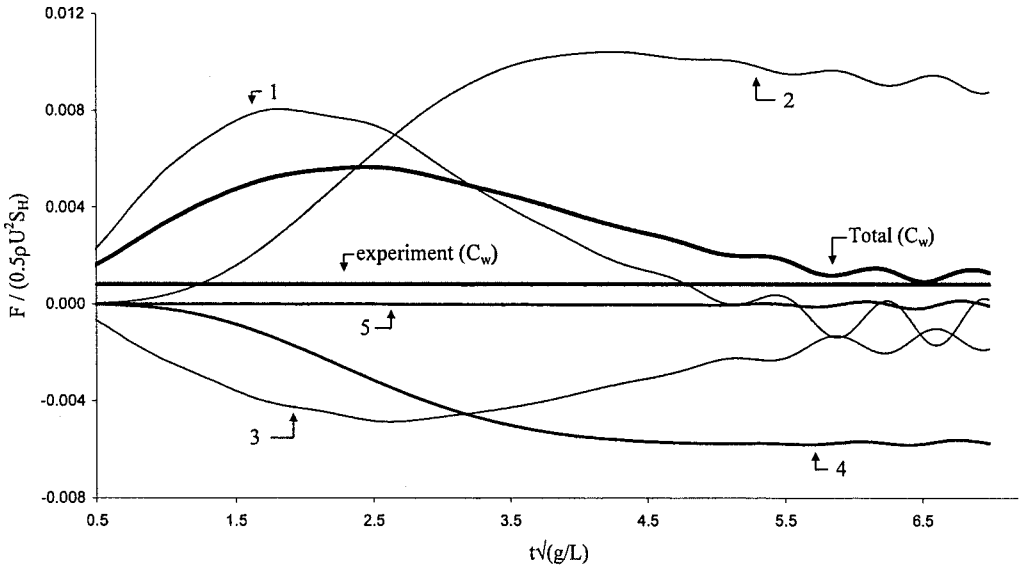

Figure 7.21: Components of the wave resistance coefficient - $F_n = 0.267$, $d_h = 0.8$, $d_{fs} = 1.0$, $\Delta t = 0.02$, $\alpha = 0.11$, 462 Rankine sources.

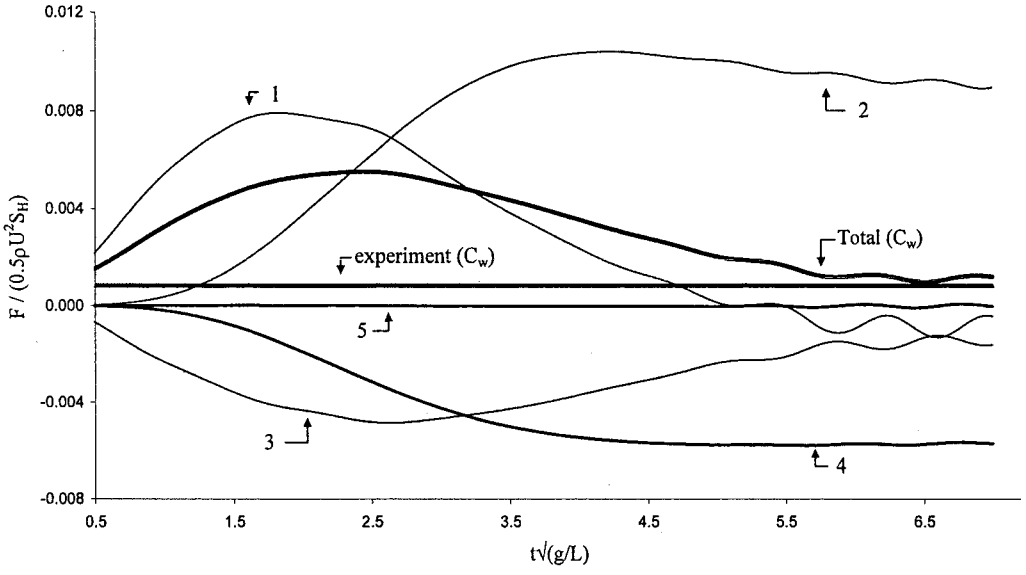

Figure 7.22: Components of the wave resistance coefficient - $F_n = 0.267$, $d_h = 0.8$, $d_{fs} = 1.0$, $\Delta t = 0.01$, $\alpha = 0.11$, 462 Rankine sources.

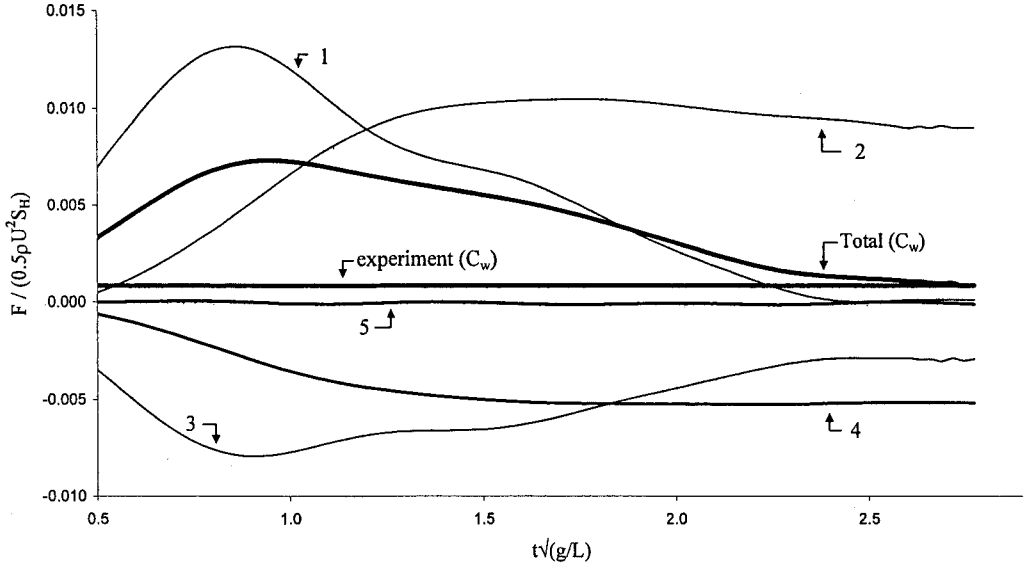

Figure 7.23: Components of the wave resistance coefficient - $F_n = 0.267$, $d_h = 0.2$, $d_{fs} = 0.8$, $\Delta t = 0.04$, $\alpha = 0.9$, 572 Rankine sources.

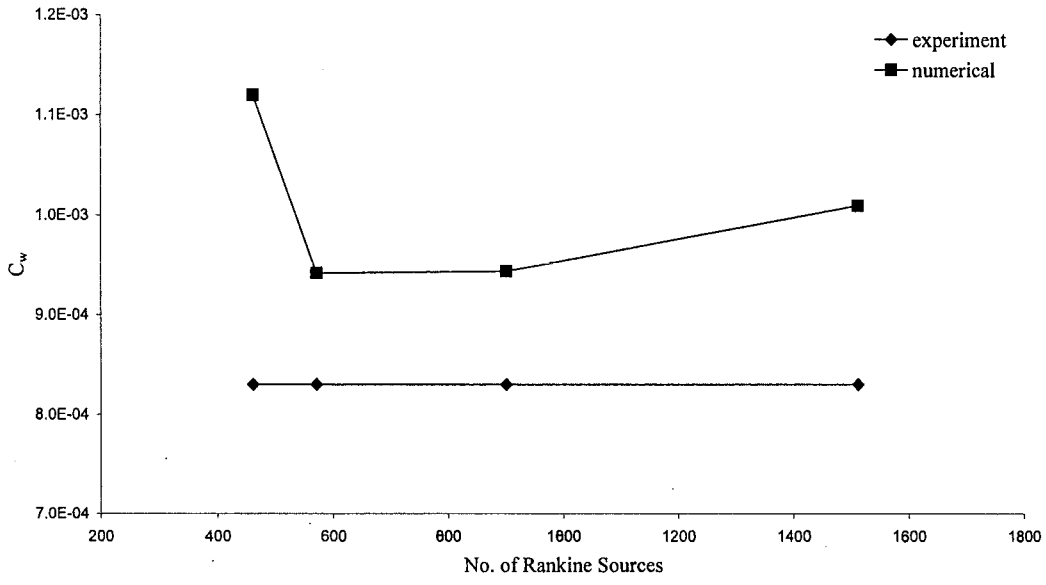

Figure 7.24: Grid-dependence of the numerical predictions for wave-making resistance of the Wigley hull at $F_n = 0.267$.

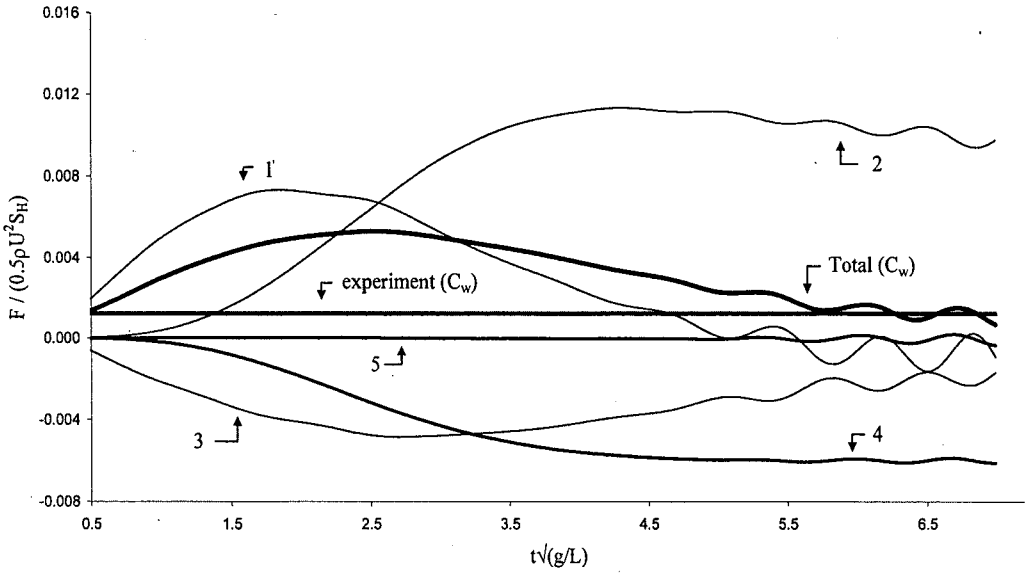

Figure 7.25: Components of the wave resistance coefficient - $F_n = 0.289$, $d_h = 0.8$, $d_{fs} = 1.0$, $\Delta t = 0.02$, $\alpha = 0.11$, 462 Rankine sources.

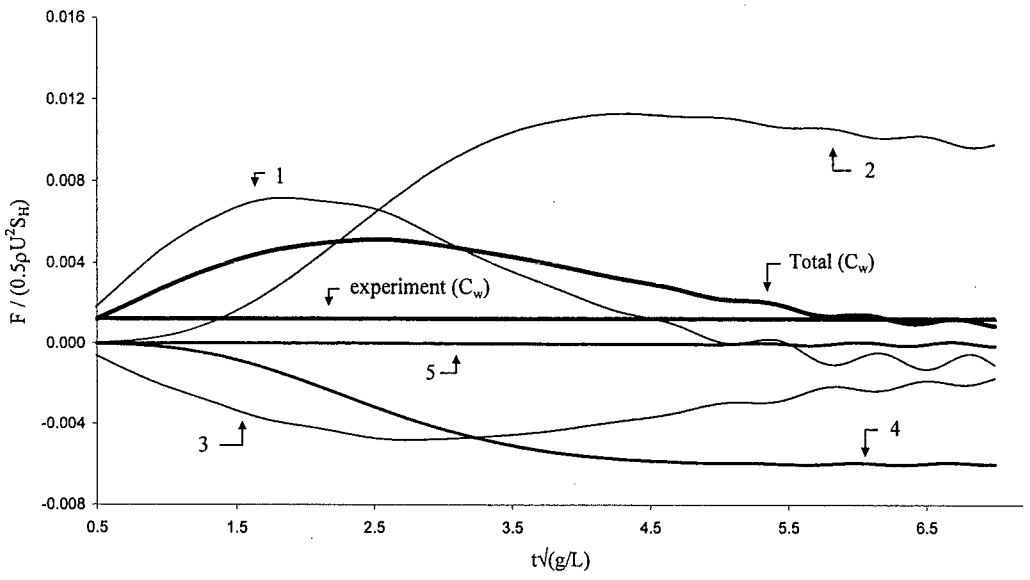

Figure 7.26: Components of the wave resistance coefficient - $F_n = 0.289$, $d_h = 0.8$, $d_{fs} = 1.0$, $\Delta t = 0.01$, $\alpha = 0.11$, 462 Rankine sources.

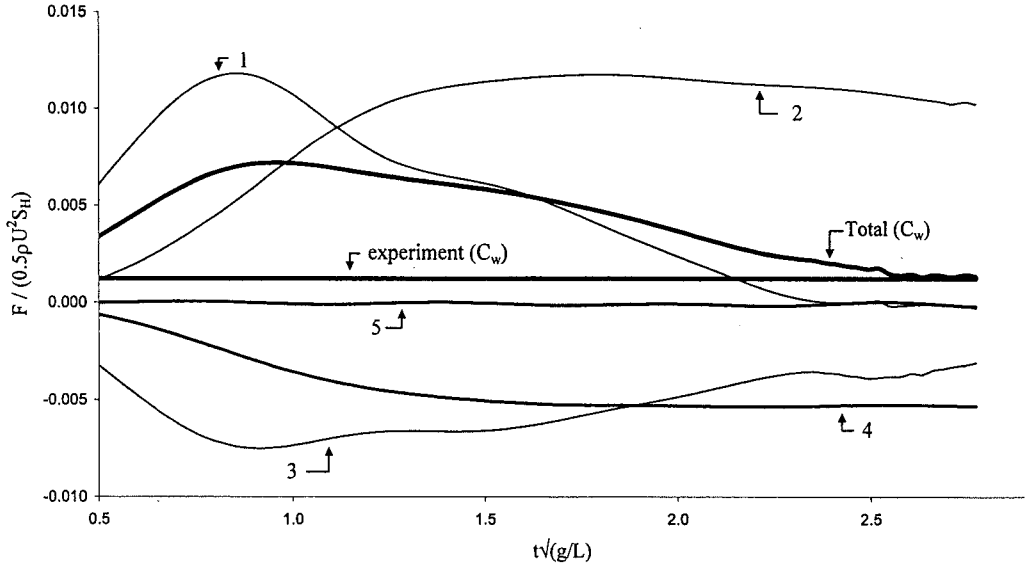

Figure 7.27: Components of the wave resistance coefficient - $F_n = 0.289$, $d_h = 0.2$, $d_{fs} = 0.8$, $\Delta t = 0.04$, $\alpha = 0.9$, 572 Rankine sources.

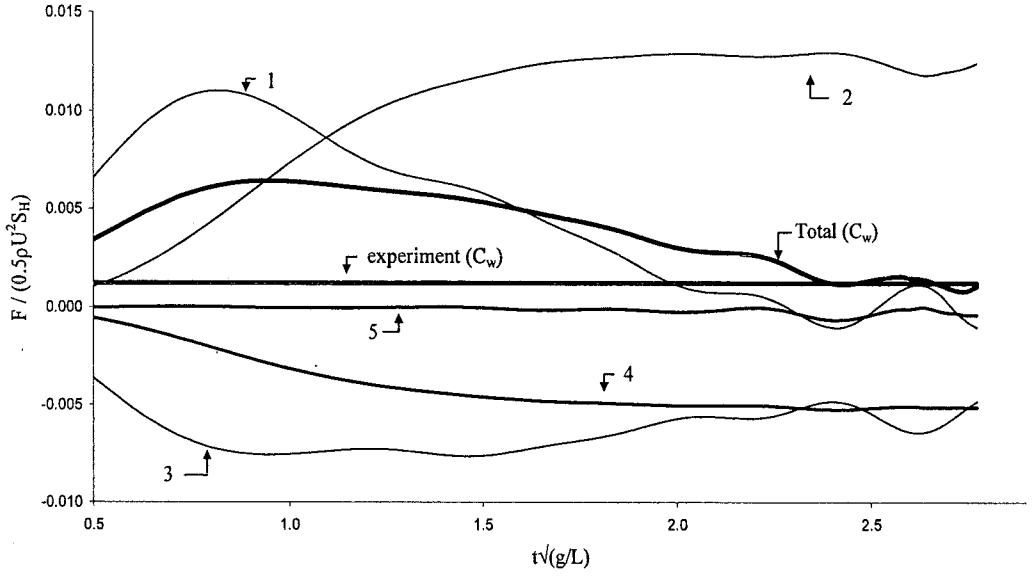

Figure 7.28: Components of the wave resistance coefficient - $F_n = 0.289$, $d_h = 0.2$, $d_{fs} = 0.5$, $\Delta t = 0.04$, $\alpha = 0.9$, 902 Rankine sources.

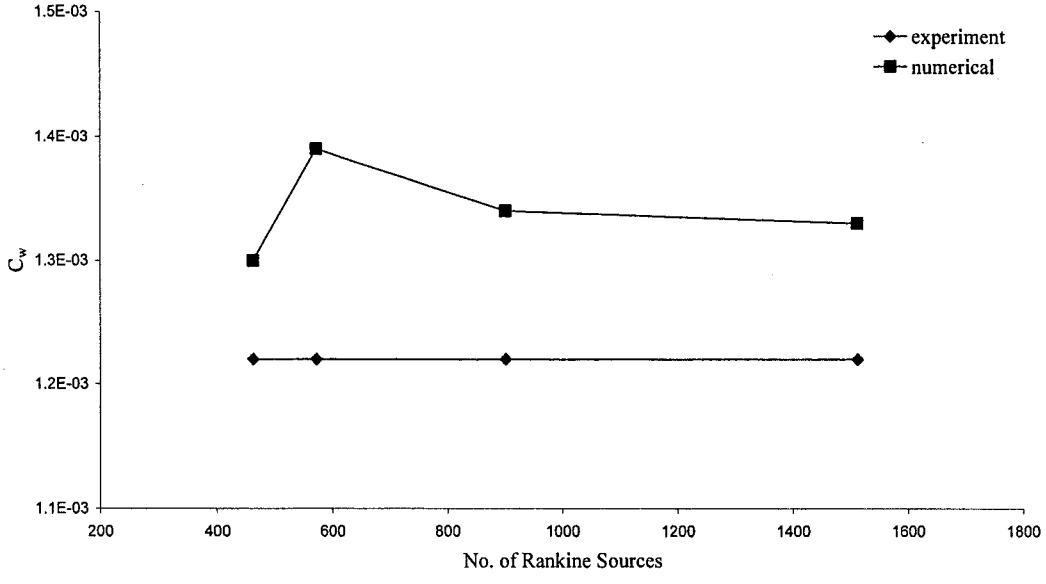

Figure 7.29: Grid-dependence of the numerical predictions for wave-making resistance of the Wigley hull at $F_n = 0.289$.

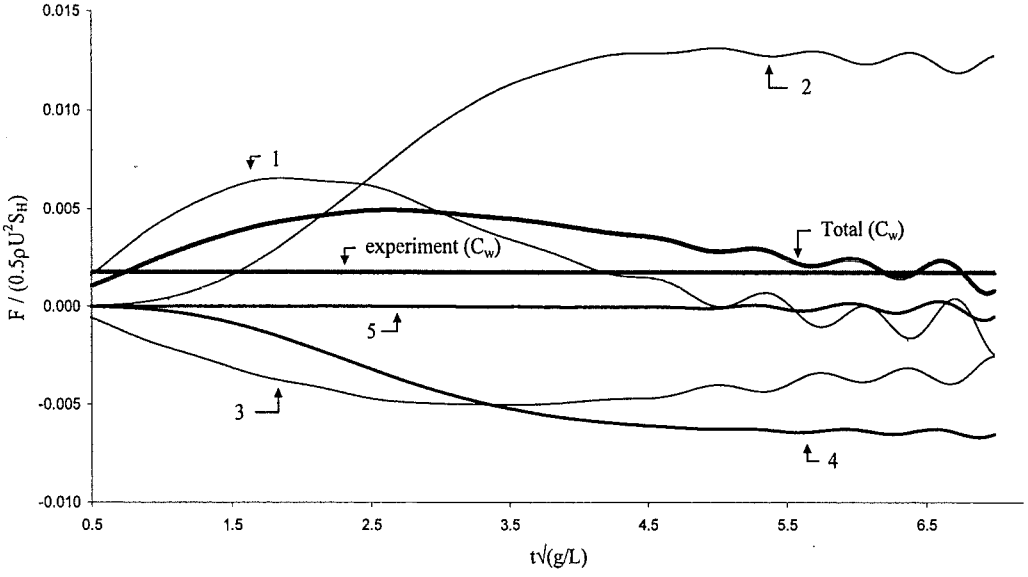

Figure 7.30: Components of the wave resistance coefficient - $F_n = 0.316$, $d_h = 0.8$, $d_{fs} = 1.0$, $\Delta t = 0.02$, $\alpha = 0.11$, 462 Rankine sources.

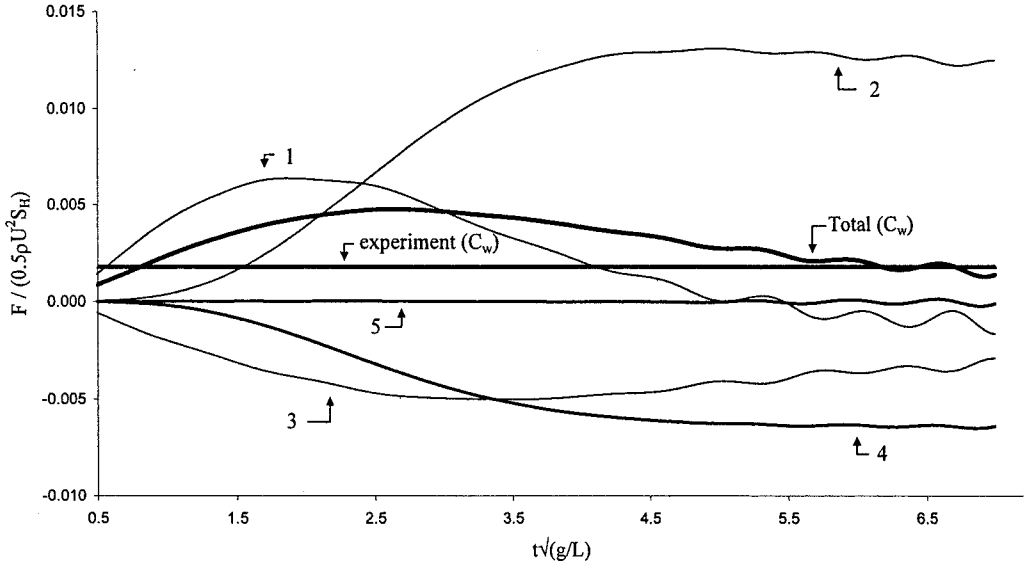

Figure 7.31: Components of the wave resistance coefficient - $F_n = 0.316$, $d_h = 0.8$, $d_{fs} = 1.0$, $\Delta t = 0.01$, $\alpha = 0.11$, 462 Rankine sources.

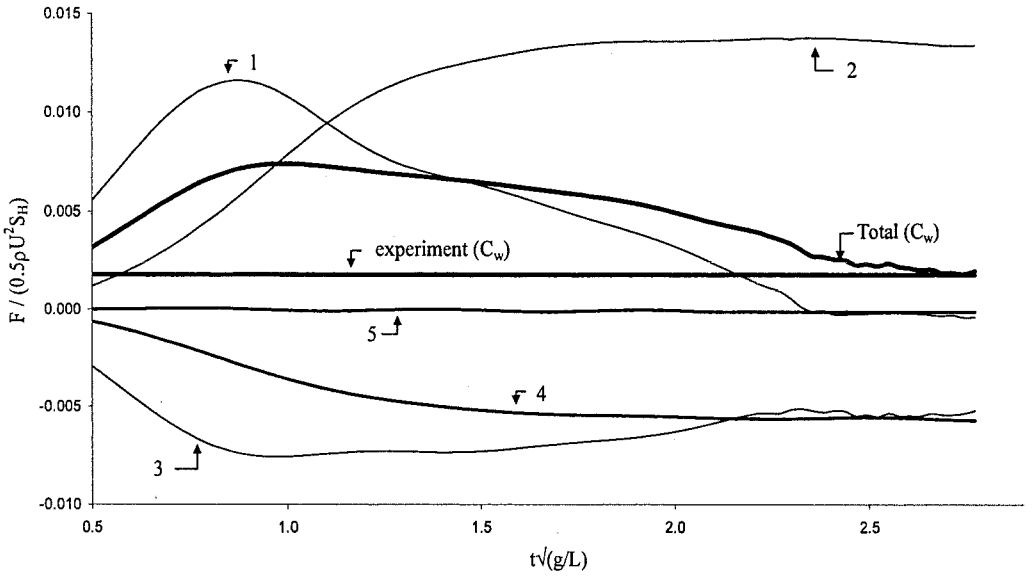

Figure 7.32: Components of the wave resistance coefficient - $F_n = 0.316$, $d_h = 0.2$, $d_{fs} = 1.0$, $\Delta t = 0.04$, $\alpha = 0.9$, 572 Rankine sources.

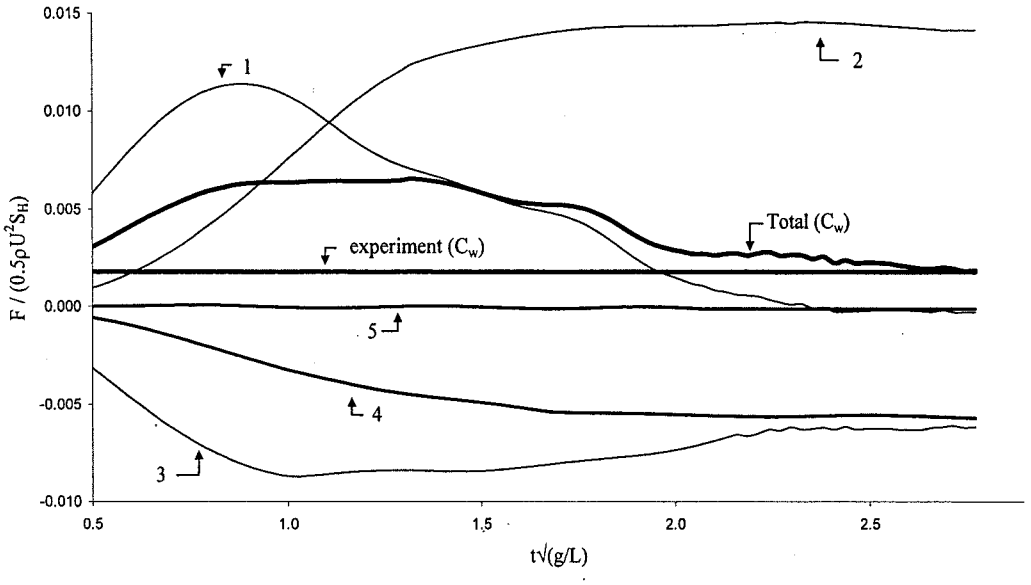

Figure 7.33: Components of the wave resistance coefficient - $F_n = 0.316$, $d_h = 0.2$, $d_{fs} = 1.0$, $\Delta t = 0.04$, $\alpha = 0.9$, 902 Rankine sources.

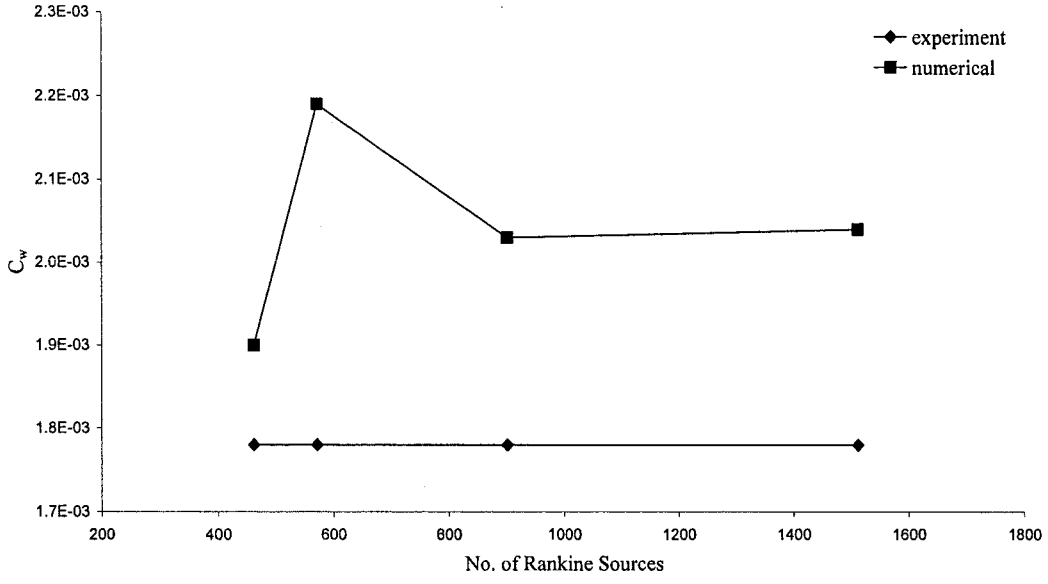

Figure 7.34: Grid-dependence of the numerical predictions for wave-making resistance of the Wigley hull at $F_n = 0.316$.

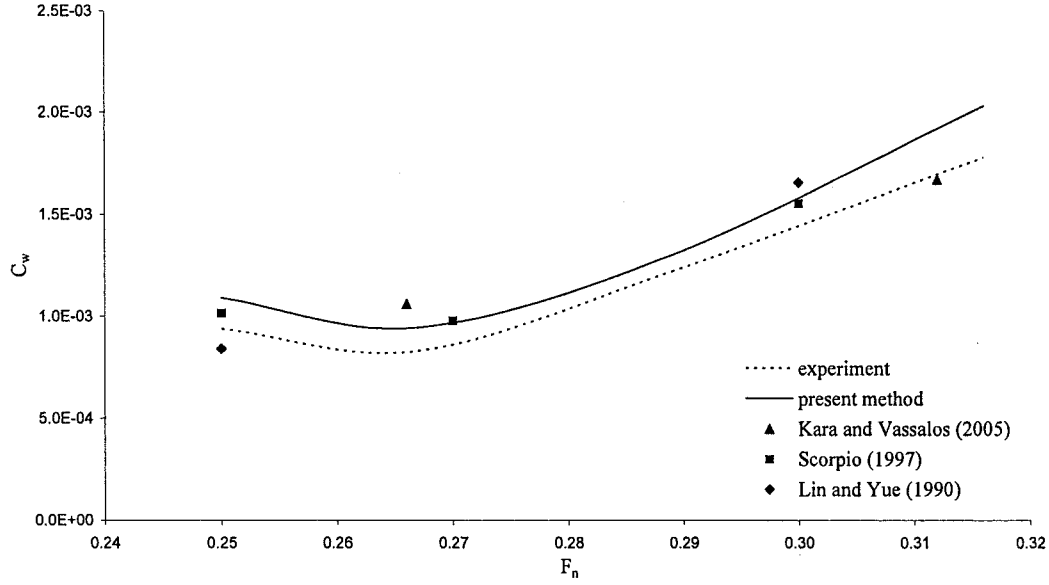

Figure 7.35: Wave-making resistance of the Wigley hull.

7.8 Sinkage and Trim

The wave profile and wave-making resistance calculations presented in the preceding sections for the Wigley hull were for fixed sinkage and trim. In order to allow sinkage and trim in the calculations, ideally, the equations of motion for the ship hull have to be solved at each time step prior to the resistance computations. However, as an initial step an approximate method is adopted.

Assuming small changes in the position of the ship, the hydrodynamic force in the vertical direction, F_3, and the moment about the y-axis, F_5, are used to adjust the position of the ship hull every time step. Namely,

$$\begin{Bmatrix} \Delta z \\ \Delta\theta \end{Bmatrix} = \begin{bmatrix} \rho g A_{WL} & -\rho g A_{WL} x_{WL} \\ -\rho g A_{WL} x_{WL} & \rho g I_{WL} \end{bmatrix}^{-1} \begin{Bmatrix} F_3 \\ F_5 \end{Bmatrix}, \tag{7.8}$$

where A_{WL} is the waterplane area, x_{WL} is the centre of the waterplane, I_{WL} is the moment of inertia, Δz and $\Delta\theta$ are the amount of sinkage and trim the hull experiences respectively.

The wave-making resistance predictions that are obtained by the method mentioned above are plotted in figure 7.36 and compared with the numerical calculations of Gadd and Daube taken from Chen and Noblesse (1983). The results are presented for both the restrained and the unrestrained hull, that is, for a hull free to sink and trim. The numerical algorithm is run for Froude numbers 0.266, 0.313 and 0.350.

The results presented in figure 7.36 are consistent with the findings of Chen and Noblesse (1983), which state that the wave-making resistance of the Wigley hull free to sink and trim is higher than of the fixed hull.

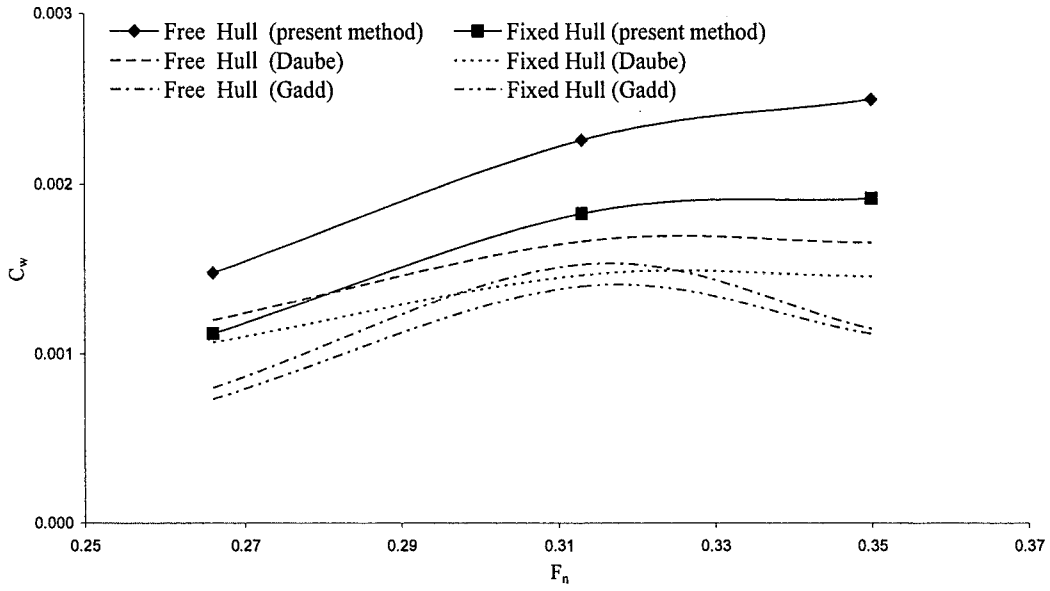

Figure 7.36: Wave resistance coefficients for the restrained and unrestrained Wigley hull - $d_h = 0.2$, $d_{fs} = 0.8$, $\Delta t = 0.02$, $\alpha = 0.11$, 462 Rankine sources.

8. SIMULATION OF THE STEADY FLOW AROUND A SERIES 60 HULL

Once the steady flow problem around the analytically defined Wigley hull form is solved, the problem is extended to the simulation of the fluid flow around a realistic hull form. A Series 60 hull (Todd (1953)) is chosen for this purpose as an extensive amount of experimental data are readily available that can be used for the validation of the numerical predictions.

The numerical algorithm described in chapter 7 was modified in such a manner that it is now possible to model the fluid flow around mathematically defined hull surfaces. In this chapter, these modifications are discussed briefly and numerical predictions are presented for the Series 60 hull.

8.1 Discretisation of the Body Surface

A cubic B-spline scheme is incorporated into the numerical algorithm (see chapter 5) in order to discretise the Series 60 hull. Since the body boundary condition is applied on the instantaneous position of the wetted hull surface, the discretisation of the Series 60 hull is repeated at each time step.

The principal dimensions of the Series 60 hull used in the numerical simulations are given in table 8.1 (See Todd (1953)). Similar to the discretisation of the Wigley hull, Rankine point sources are located inside the hull surface in the normal direction and the hull desingularisation distance is obtained using equation 7.1.

L (m)	121.92	**D (m)**	9.7580
B (m)	16.256	**S_H (m^2)**	2526.4
T (m)	6.5020	**C_B**	0.6

Table 8.1: Principal dimensions of the Series 60 hull.

8.2 Discretisation of the Free Surface

The computational grid used for the Series 60 hull is plotted in figure 8.1. The upstream, downstream and side boundaries are positioned $0.875L$, $1.125L$ and $0.9L$ away from the hull respectively (see section 8.5, figures 8.24 to 8.26, for an analysis on the position of the truncated boundaries). The control points are concentrated in the vicinity of the bow and stern to reflect the relatively large changes in the hull geometry at these regions. Since the flow details are less important in the far-field, the transverse distance between the control points on the free surface is increased algebraically towards the side boundary. This also acts as a simple damping mechanism and helps to reduce the wave amplitudes before the waves reach the side boundary.

The horizontal movements of the free surface nodes are constrained and hence the free surface is discretised only once prior to flow simulation. The same discretisation is then used for the rest of the simulation time. At every time step, the control points on the hull/free surface interface are used to update the wave elevations along the hull surface (see section 5.4).

The vertical distance between free surface field and source points is determined using equation 7.2. The positions of the Rankine point sources are adjusted at each time step consistent with the vertical displacement of the control points on the free surface.

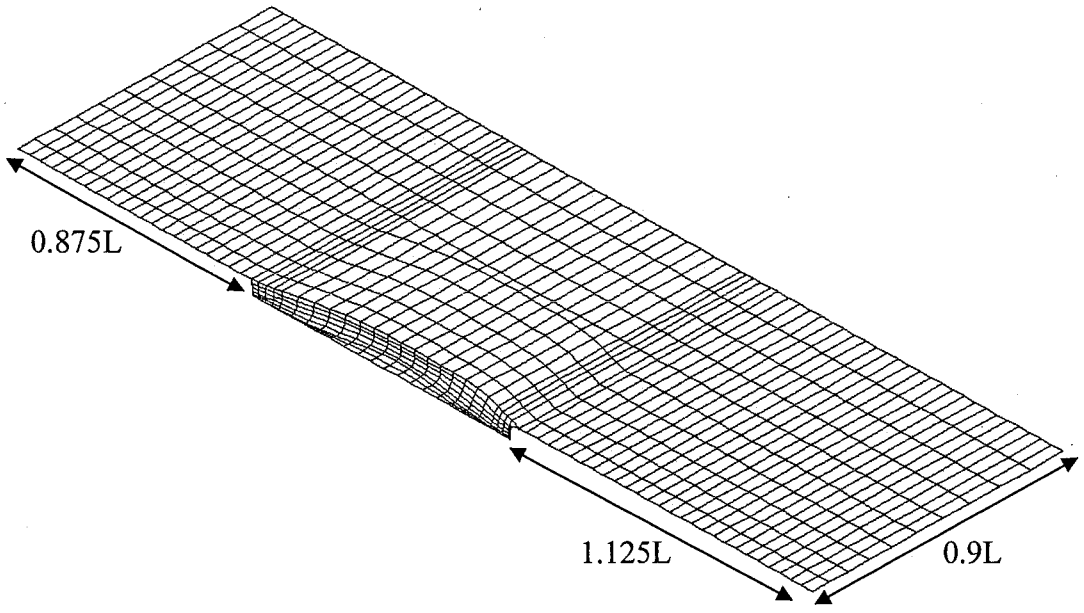

Figure 8.1: Computational grid for the Series 60 hull.

8.3 Integration of the Free Surface Boundary Conditions

Once again, the fourth-order Runge-Kutta method is adopted for the integration of the kinematic and dynamic free surface boundary conditions. An integration scheme based on the fourth-order Runge-Kutta method (Ferziger and Peric (2000)) consists of the solution of four consecutive sub-steps: a half-step forward Euler predictor, a half-step backward Euler corrector, a full-step midpoint rule predictor and a full-step Simpson's rule corrector. In a single time step, this requires four runs of the Euler phase, i.e. equation 4.14 has to be solved four times at every time step.

However, if a compromise is made between accuracy and computational time, it may be possible to utilise influence coefficients that remain constant over the period of a single time step. That is to say, the influence coefficient matrix, $[I]$, can be updated once per time step and the same coefficient matrix can then be used for the Runge-Kutta scheme at that particular time step. As long as the time-step size is not too large, it is thought that this choice will not have a considerable effect on the accuracy of the outcome (see section 8.4).

As in the case of the Wigley hull, the prescribed velocity is set to $\vec{v} = (0, 0, \partial\eta/\partial t)$ and therefore the spatial derivatives of the wave elevation appear in the kinematic free surface boundary condition (see equation 4.17).

The spatial derivatives of the wave elevation ($\partial\eta/\partial x$ and $\partial\eta/\partial y$) must be evaluated numerically prior to the integration of the free surface boundary conditions. $\partial\eta/\partial x$ and $\partial\eta/\partial y$ are determined using simple finite-differencing schemes. In order to increase the accuracy of the results obtained by the differencing schemes, cubic splines are fitted to the actual free surface grid in x and y directions and a new free surface grid is generated with increased number of control points. This new grid is then used to find

the spatial derivatives of the wave elevation on control points that correspond to the original free surface grid.

8.4 Sensitivity to Numerical Parameters

The sensitivity of the algorithm to the changes in different numerical parameters is investigated in section 7.5 for the Wigley hull. Since the algorithm is further modified to deal with realistic hull shapes, it is appropriate to carry out another convergence study specifically for the Series 60 hull. A test case denoted *test-B* is used for the purpose of comparison. Numerical parameters used for *test-B* and the number of Rankine point sources are listed in tables 8.2 and 8.3 respectively.

The choice of numerical parameters is crucial for the stability of the numerical scheme. It should be reminded that optimal parameters depend both on the hull form and the Froude number. Ideally, a detailed numerical sensitivity analysis should be carried out for each hull form at different Froude numbers. However, the numerical parameters given in tables 7.3 and 8.2 can be used as a general guideline. For different hull forms and ship speeds the time-step size should be between 0.01 and 0.05. Values higher than 0.05 may cause numerical instability. The hull acceleration parameter should not be increased beyond 1.0 for the same reason. On the other hand, it is not easy to provide rough estimates for the desingularisation distances as these depend largely on the hull form. However, the hull desingularisation distance must be kept much smaller for ship hulls with a flat bottom such as the Series 60.

The effect of hull desingularisation distance on the numerical solution is demonstrated in figure 8.2. The plots are for the time histories of the fluid velocity of two different control points on the body surface (denoted P1 and P2). As it is clear from the figure, the results are not very sensitive to the changes in d_h in this range. A similar trend is

observed in figure 8.3, where the time histories of the fluid velocity at the same control points are plotted for varying free surface desingularisation distances.

The effect of time-step size is illustrated in figure 8.4. Calculations are performed for five different time-step sizes ranging from 0.04 to 0.2. The results are insensitive to the changes in the time-step size up to $\Delta t = 0.08$. For a relatively high time-step size of 0.2, results start to diverge at around $t\sqrt{g/L} = 0.9$ and the computations stop after a while due to numeric instability. With such a large integration time step, it is clear that the algorithm could not resolve the temporal variations in the fluid.

As mentioned previously in section 7.5, the hull acceleration parameter α mainly affects the overall computational time and has only a modest effect on the outcome (see figure 8.5).
The analysis is carried out further for two free surface control points (denoted P3 and P4) and presented through figures 8.6 to 8.9. For a d_h value of 0.003 there are some oscillations present in figure 8.6. When d_h is further increased to 0.03 the results for the free surface control points fail to converge. These findings show that the distance between the field and source points must be kept much lower for the Series 60 hull in order to ensure numerical stability.

In figure 8.7, the time histories of the fluid velocity at the control points on the free surface are plotted for different free surface desingularisation distances. Although there are oscillations present for the lowest d_{fs} value, all solutions converge to a similar value.

The situation for the free surface control points is similar to the ones on the hull surface as far as the time-step size and hull acceleration parameter are concerned (see figures 8.8 and 8.9). There is only a slight unsteady behaviour of control point P3 in figure 8.9 for $\alpha = 1.2$ which was not observed for the control points on the hull surface.

In section 8.3, it was mentioned that instead of solving 4 Euler phases at each time step it may be possible to use an influence coefficient matrix that is constant over the period of a single time step. As long as the accuracy is not compromised this would result in a reduction of more than 50% in the CPU time. With a careful analysis (see figure 8.10) it was seen that using constant influence matrixes over a single time step has a minor influence on the numerical results. Hence, it was decided to exploit this property of the numerical scheme for the benefit of reducing the CPU time. In order to obtain the results presented in figure 8.10, 1118 seconds of CPU time are used for those using a constant influence coefficient matrix, whereas 2312 seconds of CPU time are used for the others.

Another important property of the current numerical scheme mentioned in section 8.3 was its use of cubic splines to add extra control points to the free surface grid for the evaluation of the spatial derivatives of the wave elevation. A fixed number of new control points are added between two neighbouring control points for this purpose. In the case of *test-B*, 3 new control points are added between each adjacent control points both in the x and y directions. Once the spatial derivatives of the wave elevation are calculated, those newly obtained control points are disregarded. Figure 8.11 shows the effects of the number of control points that are added to the original free surface grid by the aforementioned cubic spline scheme. The number of extra control points has virtually no effect on the presented results. However, when the number of control points that are added between each adjacent point using the cubic spline scheme is less than 3 or when no extra point is added at all, the algorithm breaks down at the early stages of computation in most cases and fails to yield any results.

L (m)	121.92	**d_h**	0.0003
B (m)	16.24	**d_{fs}**	2.1
T (m)	6.52	**Δt (s)**	0.05
F_n	0.316	α	0.9

Table 8.2: Numerical parameters used for *test-B*.

	Hull Grid	**Free Surface Grid**
(LxT)	25x8	73x5
Total	200	365

Table 8.3: The number of Rankine sources used for *test-B*.

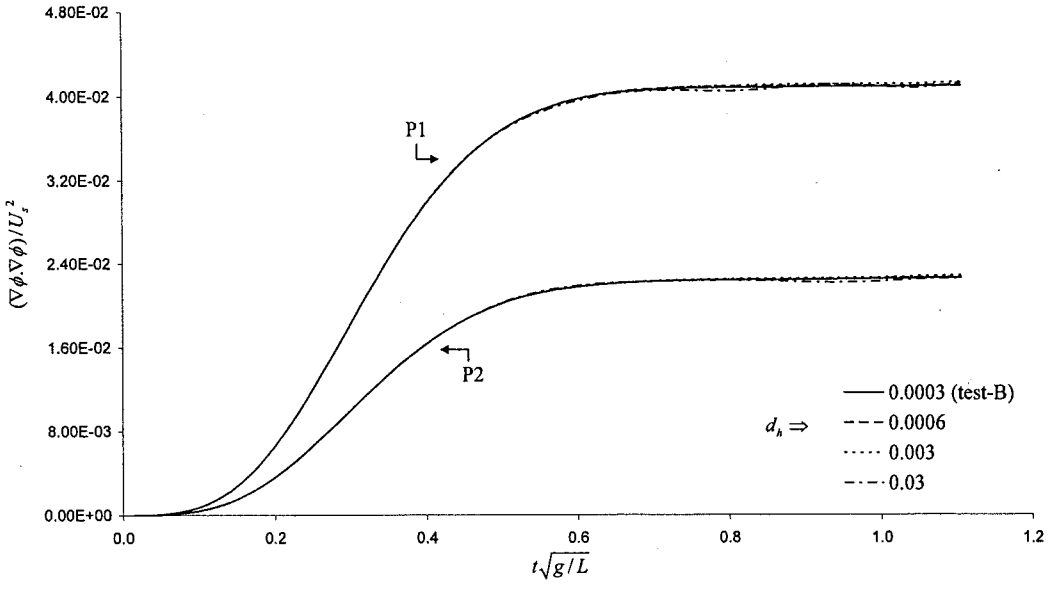

Figure 8.2: The effect of hull desingularisation distance on the numerical solution – control points on the hull surface.

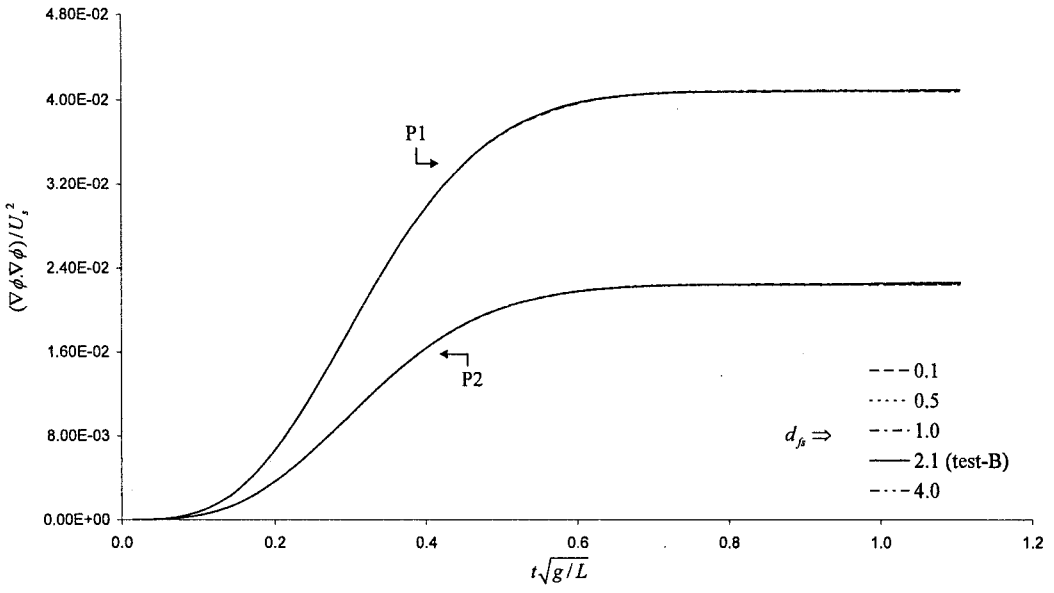

Figure 8.3: The effect of free surface desingularisation distance on the numerical solution – control points on the hull surface.

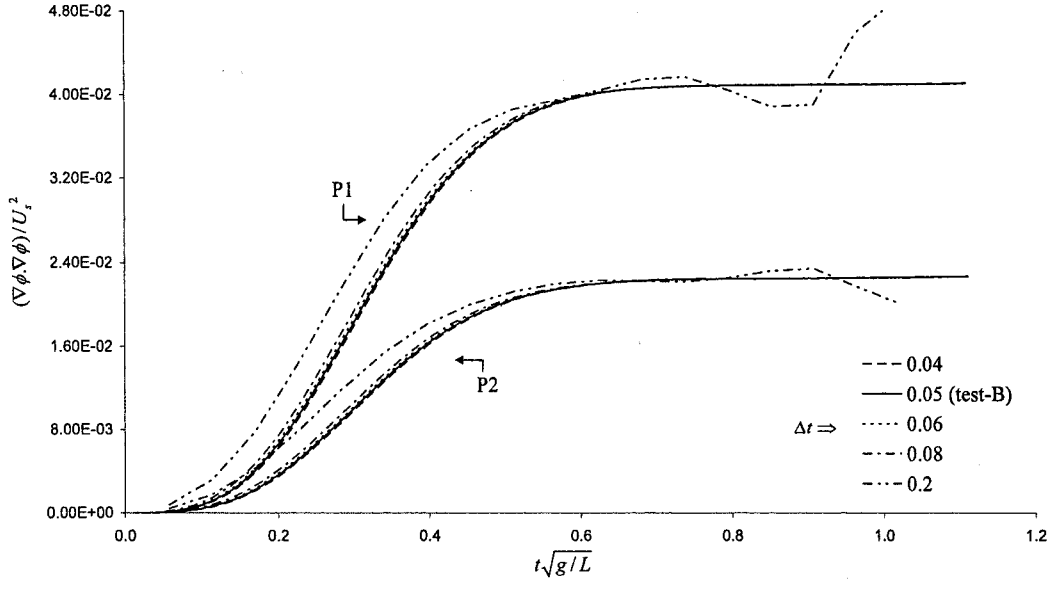

Figure 8.4: The effect of time-step size on the numerical solution – control points on the hull surface.

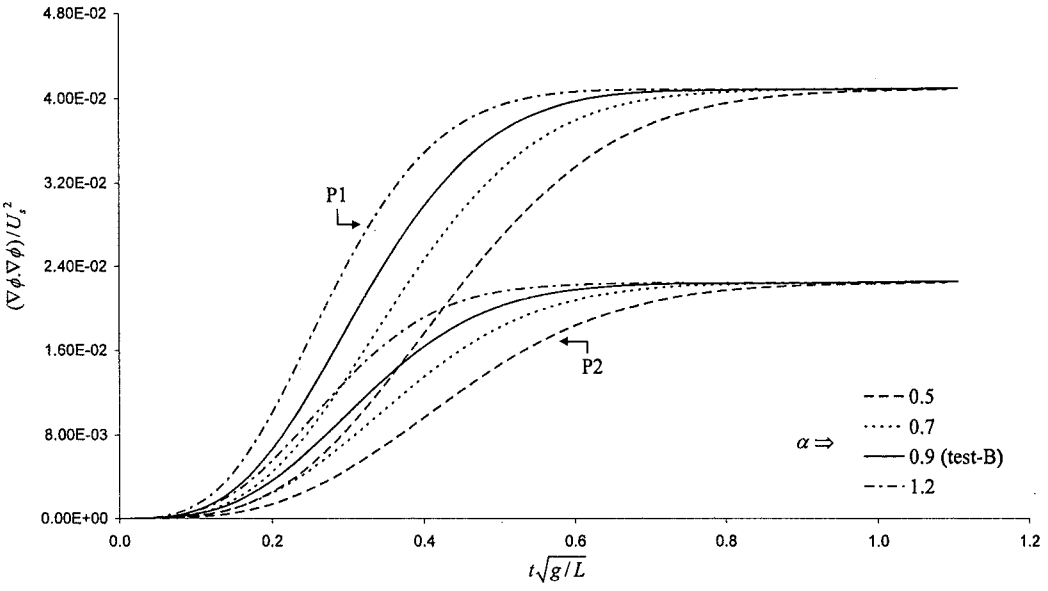

Figure 8.5: The effect of hull acceleration parameter on the numerical solution – control points on the hull surface.

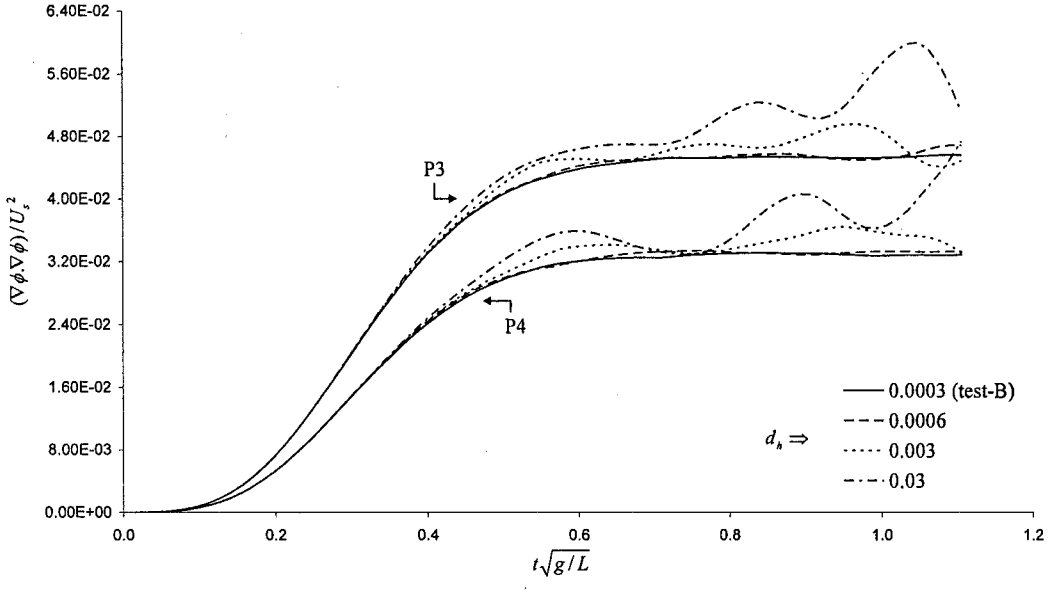

Figure: 8.6: The effect of hull desingularisation distance on the numerical solution – control points on the free surface.

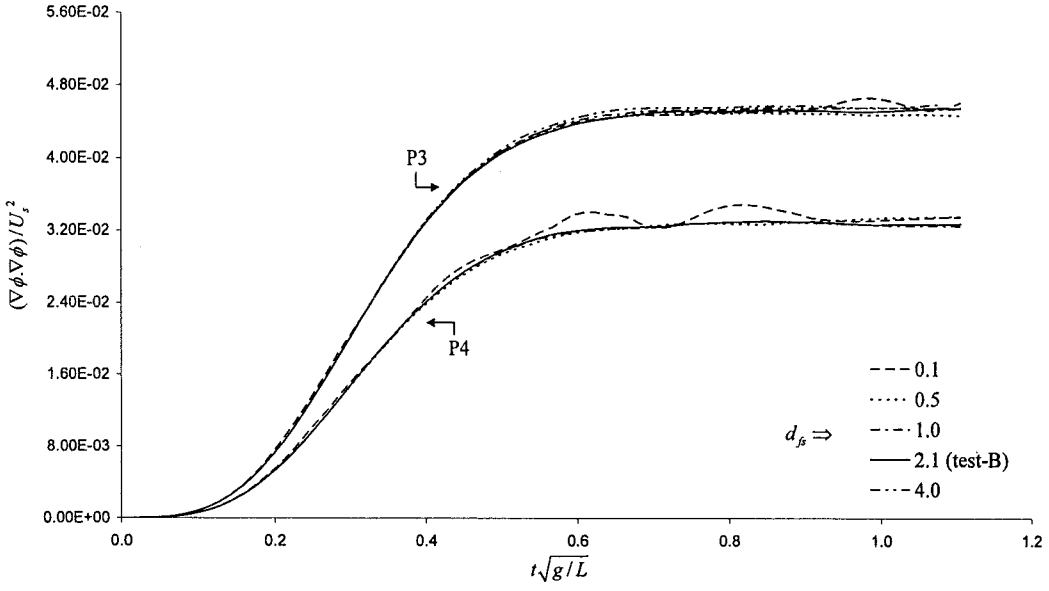

Figure 8.7: The effect of free surface desingularisation distance on the numerical solution – control points on the free surface.

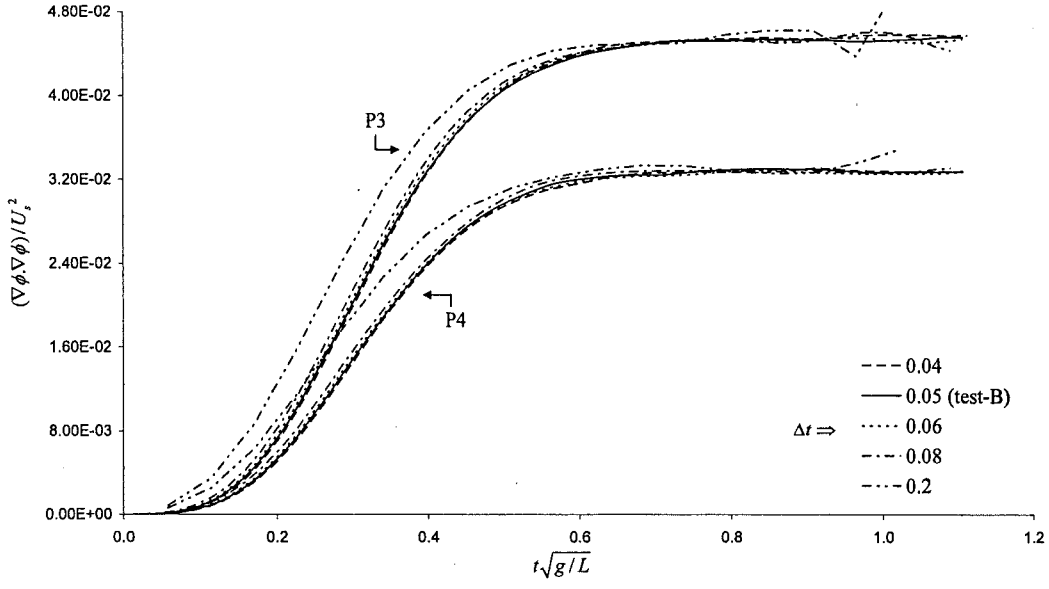

Figure 8.8: The effect of time-step size on the numerical solution – control points on the free surface.

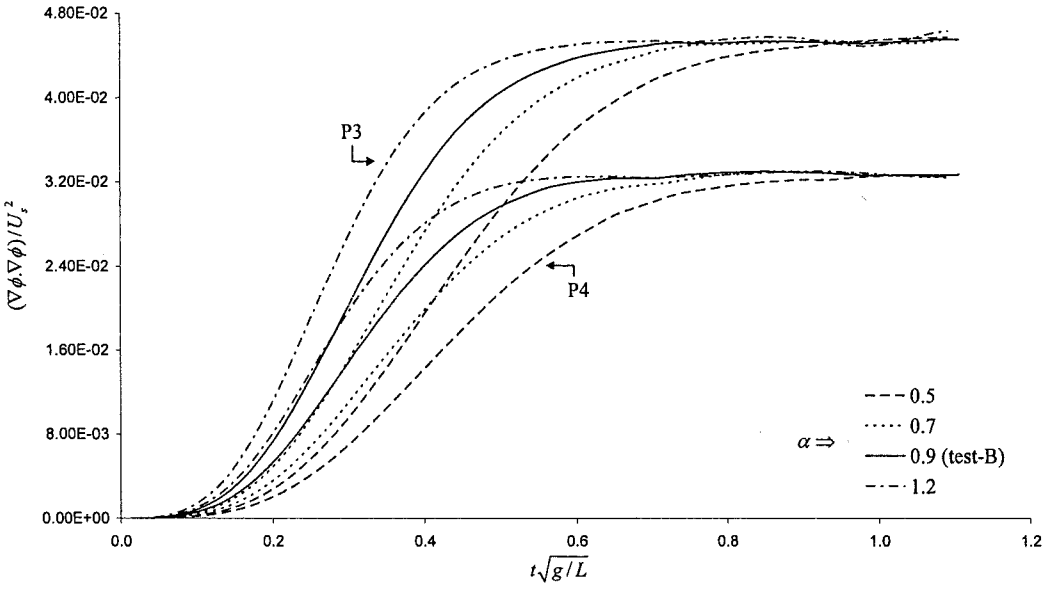

Figure 8.9: The effect of hull acceleration parameter on the numerical solution – control points on the free surface.

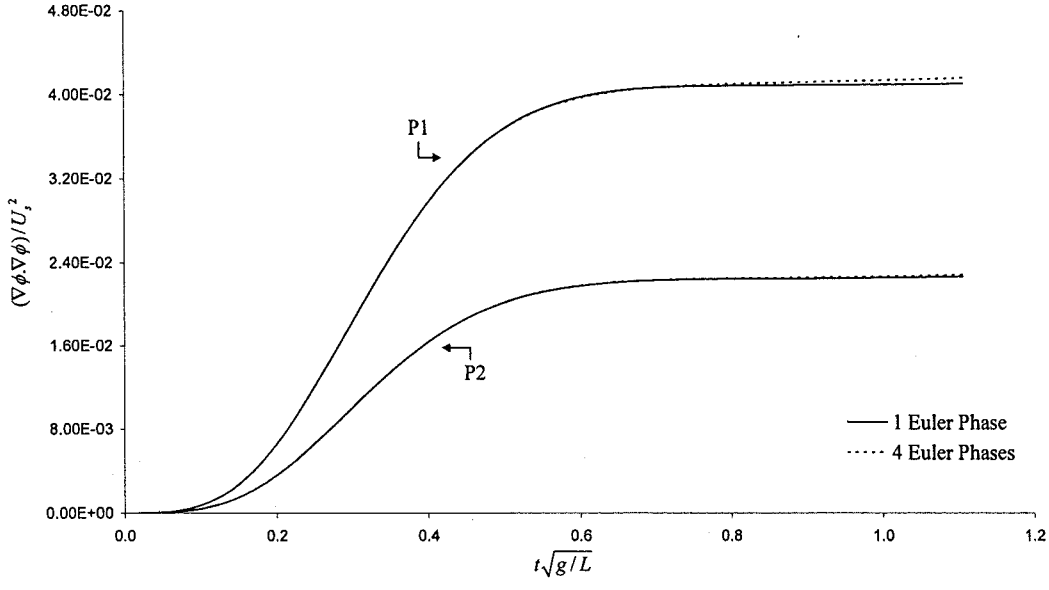

Figure 8.10: The effect of constant influence coefficient matrix on the numerical solution.

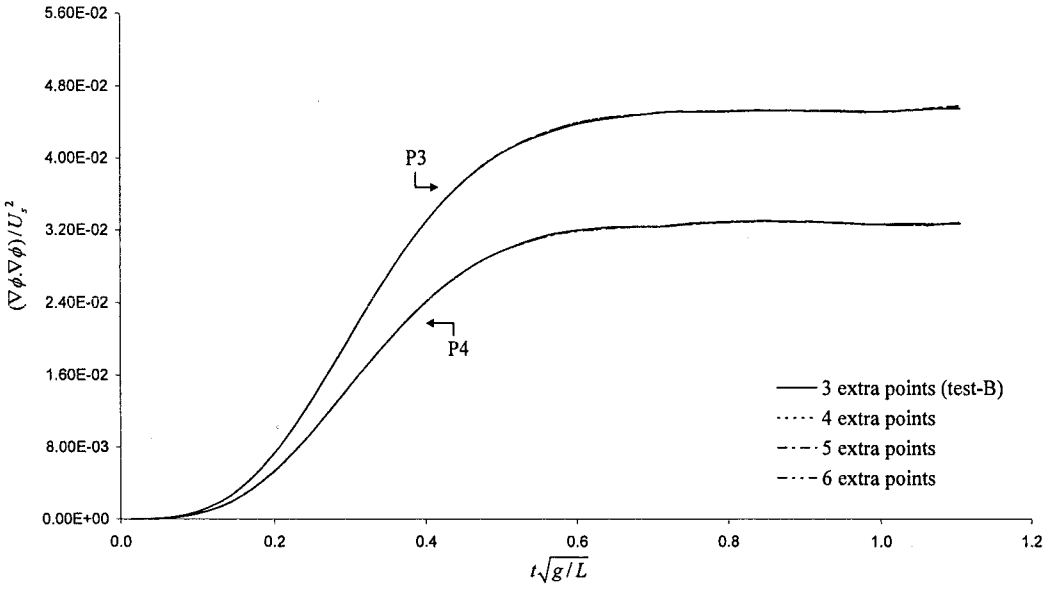

Figure 8.11: The effect of the cubic spline scheme on the numerical solution.

8.5 Wave-Making Resistance of the Series 60 Hull

Wave-making resistance of a Series 60 hull that is restrained from sinkage and trim is determined following the procedure outlined in section 7.7. However, it should be remembered that pressure integration over the hull surface is not the only means of computing the resistance of a ship hull. For instance, it is possible to predict the wave-making resistance of a hull form by wave pattern analysis, i.e. by measuring the energy contained in the wave pattern behind the hull (see, for example, Havelock (1934), Eggers et al. (1967), Raven and Prins (1998)).

The problems in pressure integration are mainly associated with the errors caused by the discretisation of the hull surface. Although hull discretisation plays no major role in wave pattern analysis, a large number of control points are required on the free surface resulting in a computationally intensive formulation. Additionally, the free surface grid should stretch far downstream in order to accurately evaluate the energy contained in the wave pattern behind the ship.

The time history of the wave resistance coefficient of the Series 60 hull at $F_n = 0.25$ is presented in figure 8.12 for different free surface meshes. The numbers 365, 511, 657, 803 in the legend correspond to the number of control points on the free surface. The computations reach a steady state at around $t\sqrt{g/L} = 0.8$. Although there are oscillations present in the figure after this time, they are not excessive and the convergence of the wave resistance coefficient with respect to free surface mesh size is satisfactory.

In figures 8.13 to 8.18, the time histories of the wave resistance coefficient are given for Froude numbers 0.28, 0.30, 0.316, 0.32, 0.34 and 0.35. Once again, the convergence of the results are analysed with respect to free surface mesh size. The curves exhibit very similar characteristics for each Froude number. The steady state is attained between

$t\sqrt{g/L} = 0.7$ and $t\sqrt{g/L} = 0.8$. The convergence is slightly better at higher Froude numbers.

The convergence properties of the wave resistance coefficient at $F_n = 0.316$ are shown through figures 8.19 to 8.22 with respect to hull desingularisation distance, free surface desingularisation distance, time-step size and hull acceleration parameter. An important outcome of this analysis is that the results are in harmony with those of section 8.4. For instance, as demonstrated previously in figure 8.6 large oscillations in the results correspond to large d_h values. This is once again exemplified in the wave resistance calculations (see figure 8.19). Similarly, a change in the hull acceleration parameter has little effect on the final value of the wave resistance coefficient (see figure 8.22), which is also in agreement with the findings of section 8.4.

The function that is used to accelerate the ship hull is given previously in equation 7.4. The wave-making resistance predictions that are obtained by using this Gaussian function are compared in figure 8.23 with those evaluated by using a linear acceleration function. The curves that correspond to these linear and Gaussian functions are also shown in the same figure.

In figure 8.24, the time histories of the wave resistance coefficient at $F_n = 0.316$ are plotted for different positions of the side boundary. The values in the legend correspond to the distance between the hull and the side boundary. The convergence of the results with respect to the side boundary position is quite satisfactory. However, at $0.3L$ the predictions start to diverge and when the distance between the side boundary and hull surface is decreased below $0.3L$, the numerical scheme fails to yield any results due to the breakdown of the computations. This is an expected outcome because this value is not large enough to prevent the reflections from the side boundary having a considerable impact on the fluid flow inside the computational domain.

The time histories of the wave resistance coefficient for different positions of the downstream edge are plotted in figure 8.25. The values in the legend correspond to the distance between the hull and the downstream edge, i.e. to the length of the downstream portion of the computational domain. Once the length of the downstream portion is reduced to $0.5L$, the computations break down at around $t\sqrt{g/L} = 0.5$. The predictions for the wave resistance coefficient converge to a similar value when the downstream section is longer than $0.5L$. A similar analysis is carried out for the upstream boundary (see figure 8.26). The convergence of the numerical predictions is satisfactory for $0.875L$ and $0.65L$. On the other hand, when the length of the upstream section of the computational domain is reduced to $0.55L$, predictions start to diverge. Once the upstream edge is positioned just $0.375L$ away from the ship hull, computations break down at around $t\sqrt{g/L} = 1.1$. Below this value, the numerical algorithm breaks down at the very early stages of computation and fails to yield any results. (not shown in the figure).

In figure 8.27, numerical predictions for the wave resistance coefficient are compared with several experimental and other numerical results gathered from various sources. The grey-coloured solid band represents the experimental measurements of Kim and Jenkins (1981) and Norrbin (1984) for a Series 60 hull with a block coefficient of 0.60 at fixed sinkage and trim. The dashed band shows the results of the numerical computations of Aanesland (1989) and Musker (1989). The former used a hybrid linear method combining Rankine and Kelvin sources, whereas the latter utilised a linear Rankine source method. The continuous black line illustrates the wave-making resistance predictions of Kim and Lucas (1990) that are obtained using a nonlinear Rankine source method. And finally the black dots are the results of the present study. For all the results presented in figure 8.27, the resistance of the ship hull is computed by pressure integration over the hull surface.

What strikes the eye at a first glance in figure 8.27 is the almost constant distribution of the wave resistance coefficient predictions of the current study. Roughly speaking, the

wave resistance of a ship hull is proportional to the square of the ship velocity at low speeds, whereas at high speeds this proportion may increase up to the sixth power of the ship speed (Lewis (1988)). Since the wave resistance coefficient C_w is non-dimensionalised by the square of the ship speed, the relation between the wave resistance coefficient and the ship speed can increase up to $C_w \alpha U^4$ at high Froude numbers. To get a clear view of the situation, numerical predictions of the present study are plotted in figure 8.28 on their own. Now it is observed that the predictions in fact follow the correct trend as far as the basic qualitative relation between the wave resistance and the ship speed is concerned. However, the predictions are too high at low Froude numbers and slightly low at higher Froude numbers. The discrepancies with the experiments cannot be attributed to discretisation errors since the numerical predictions converge to a similar value for different grid sizes (see figures 8.12 to 8.18).

There already exists more accurate methods that can be used to calculate calm water resistance of ship hulls (see Raven (1998)). However, these methods require considerably higher computational time, which restricts their use as a practical design tool. More importantly, they cannot be extended for the solution of the unsteady problem.

Whilst the present numerical algorithm, which utilises horizontally-fixed free surface points that have not been applied to simulate the fluid flow around three-dimensional geometries with forward motion before, shows promise for Wigley hull and some aspects of Series 60 hull a more detailed analysis would be needed to find the precise reasons for its failure to reach a quantitative agreement with the experimental measurements. These may well include some of the distinct properties of the present numerical algorithm such as the horizontally-fixed free surface points or the use of point sources. Therefore, if one wants to extend the present method to the solution of the unsteady problem in a future study, a comprehensive analysis regarding stability, damping and dispersion of the three-dimensional formulation should be carried out.

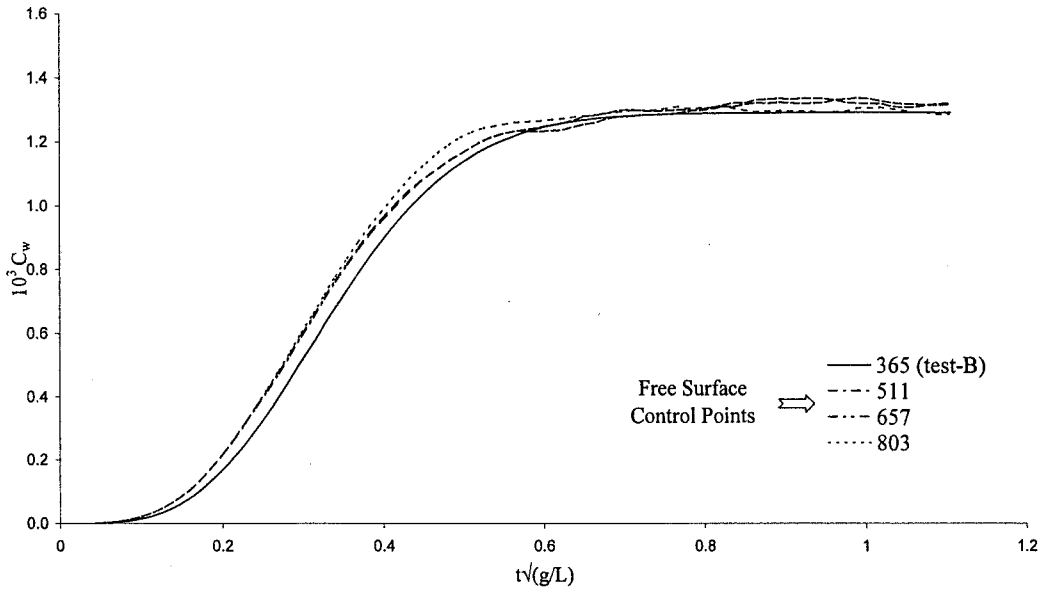

Figure 8.12: Time history of the wave resistance coefficient for different free surface meshes - $F_n = 0.25$.

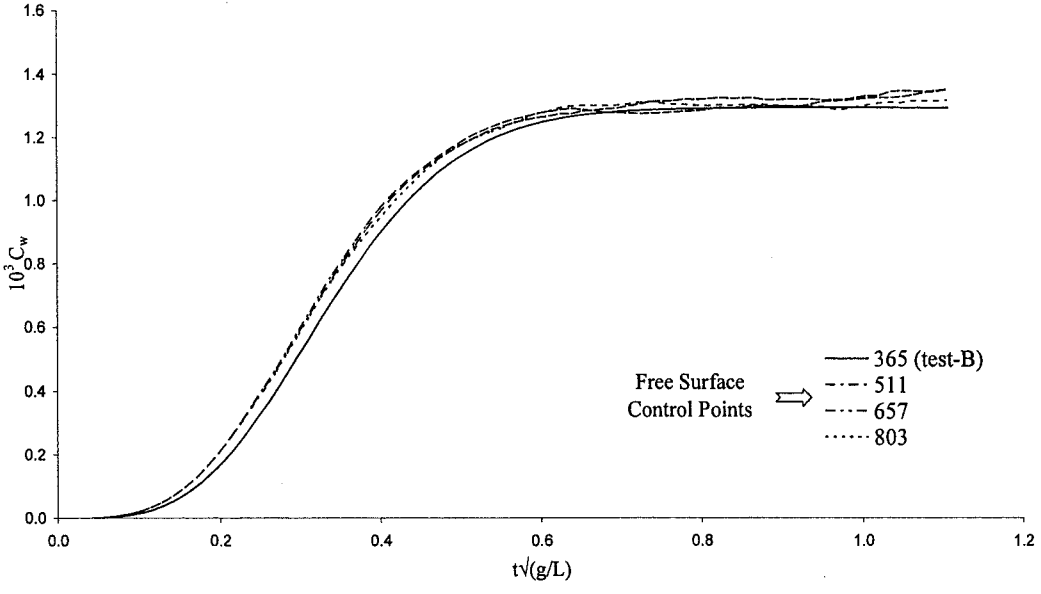

Figure 8.13: Time history of the wave resistance coefficient for different free surface meshes - $F_n = 0.28$.

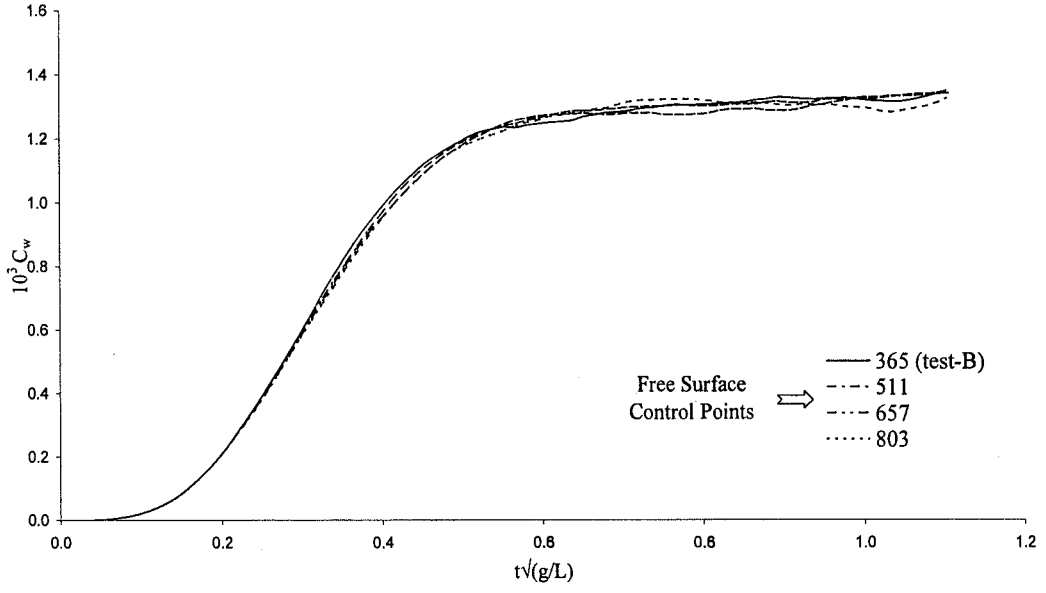

Figure 8.14: Time history of the wave resistance coefficient for different free surface meshes - $F_n = 0.30$.

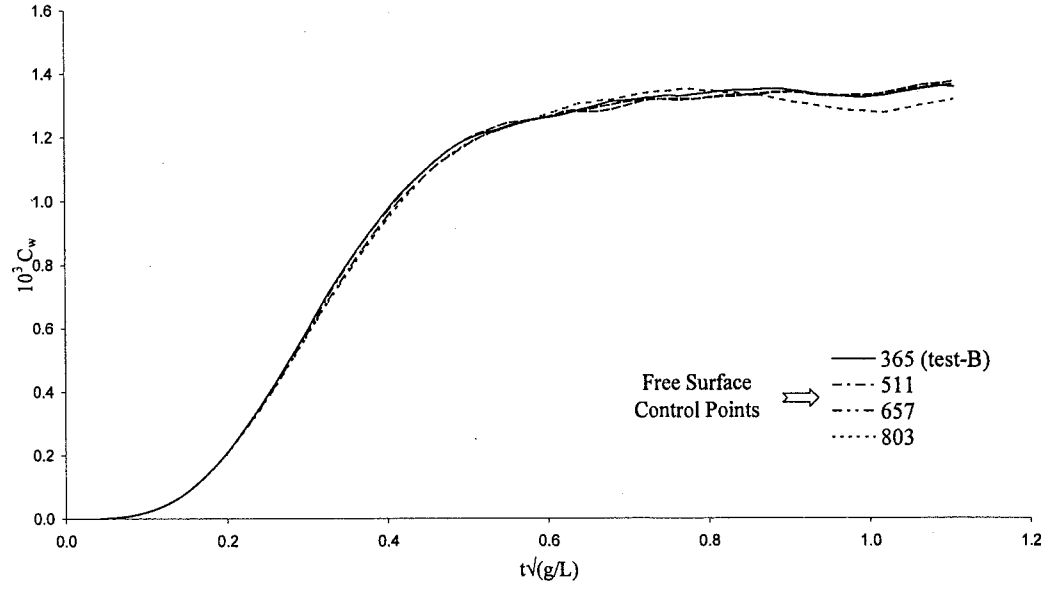

Figure 8.15: Time history of the wave resistance coefficient for different free surface meshes - $F_n = 0.316$.

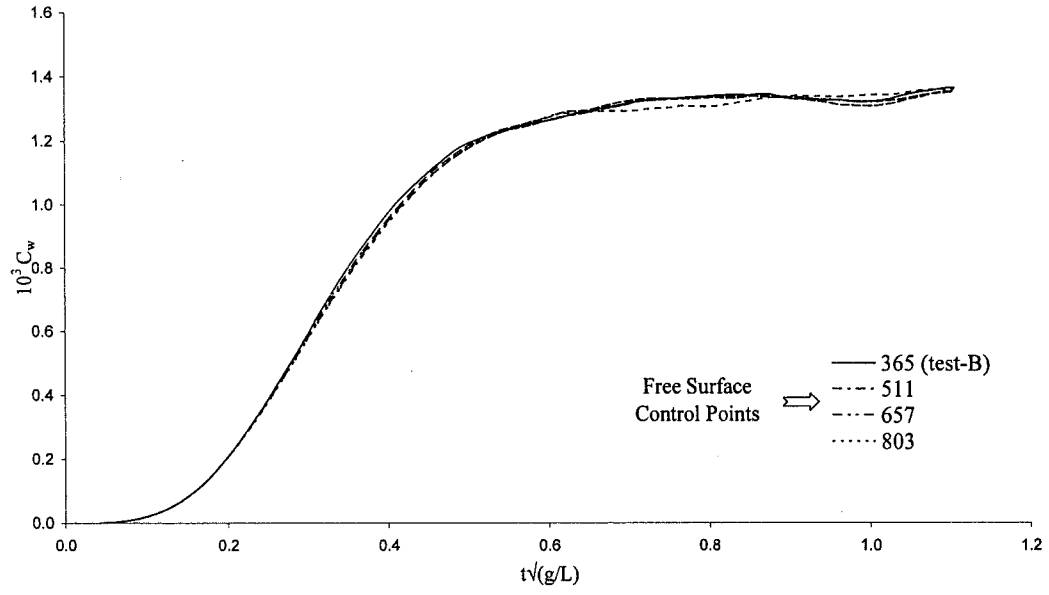

Figure 8.16: Time history of the wave resistance coefficient for different free surface meshes - $F_n = 0.32$.

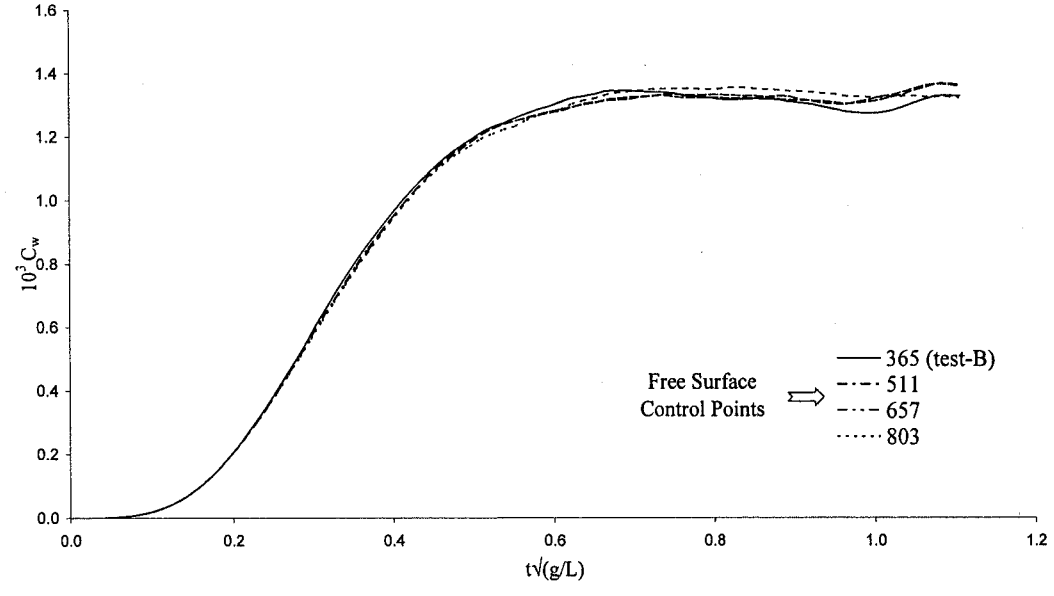

Figure 8.17: Time history of the wave resistance coefficient for different free surface meshes - $F_n = 0.34$.

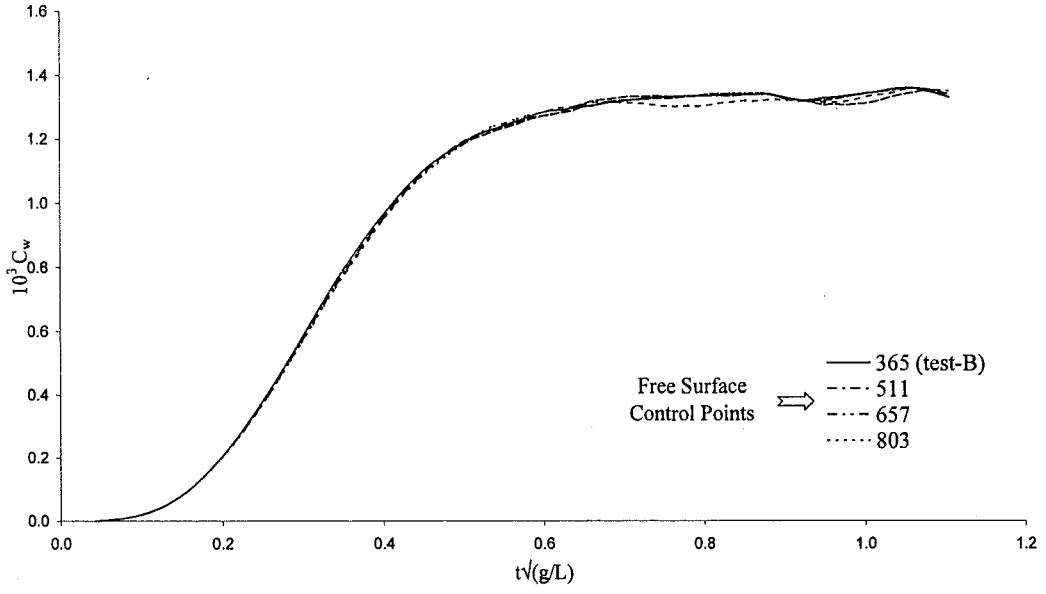

Figure 8.18: Time history of the wave resistance coefficient for different free surface meshes - $F_n = 0.35$.

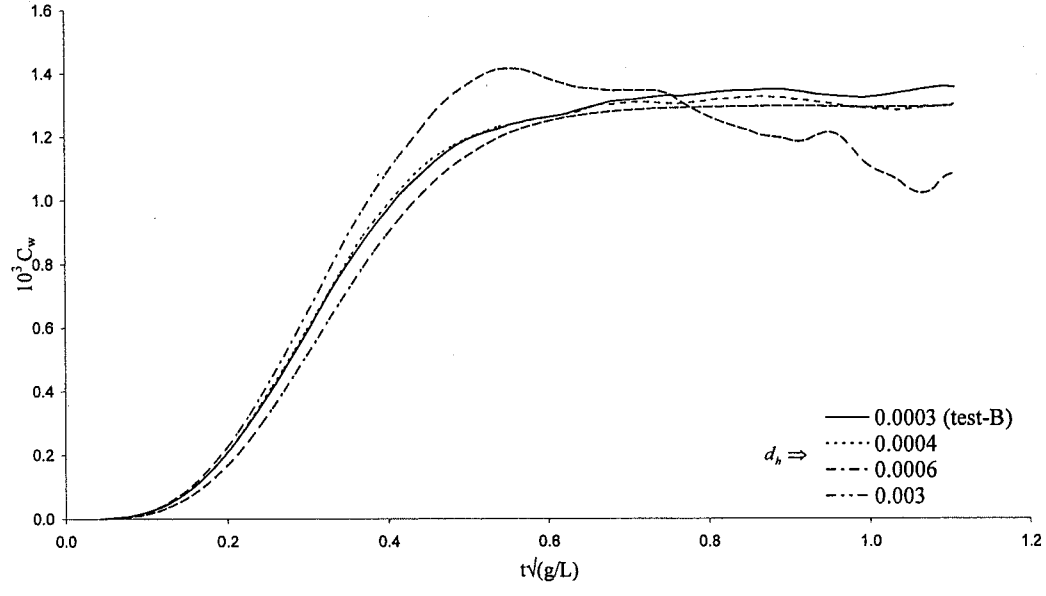

Figure 8.19: Time history of the wave resistance coefficient for varying hull desingularisation distance - $F_n = 0.316$.

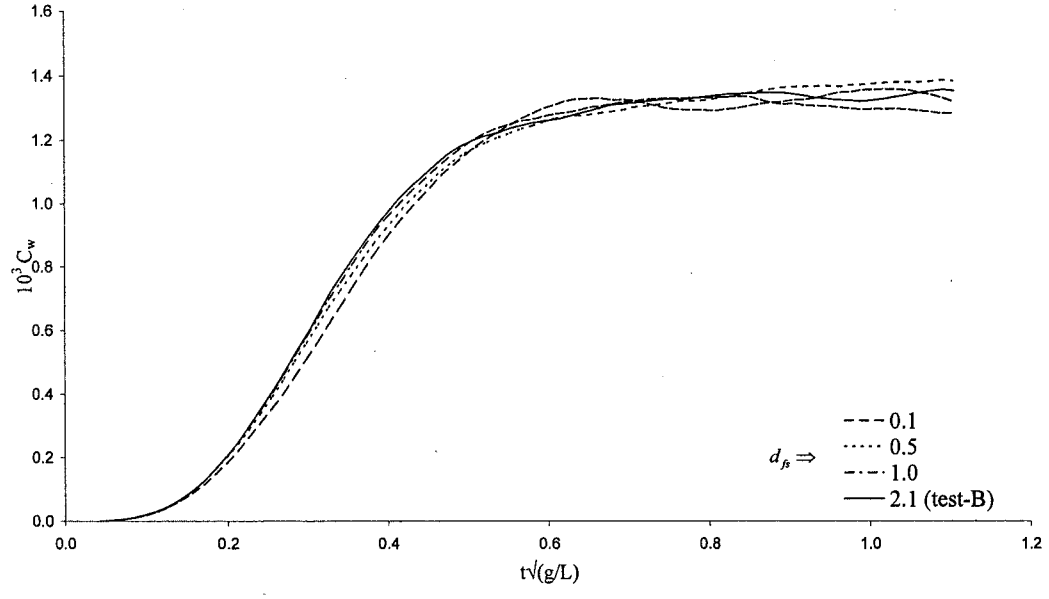

Figure 8.20: Time history of the wave resistance coefficient for varying free surface desingularisation distance - $F_n = 0.316$.

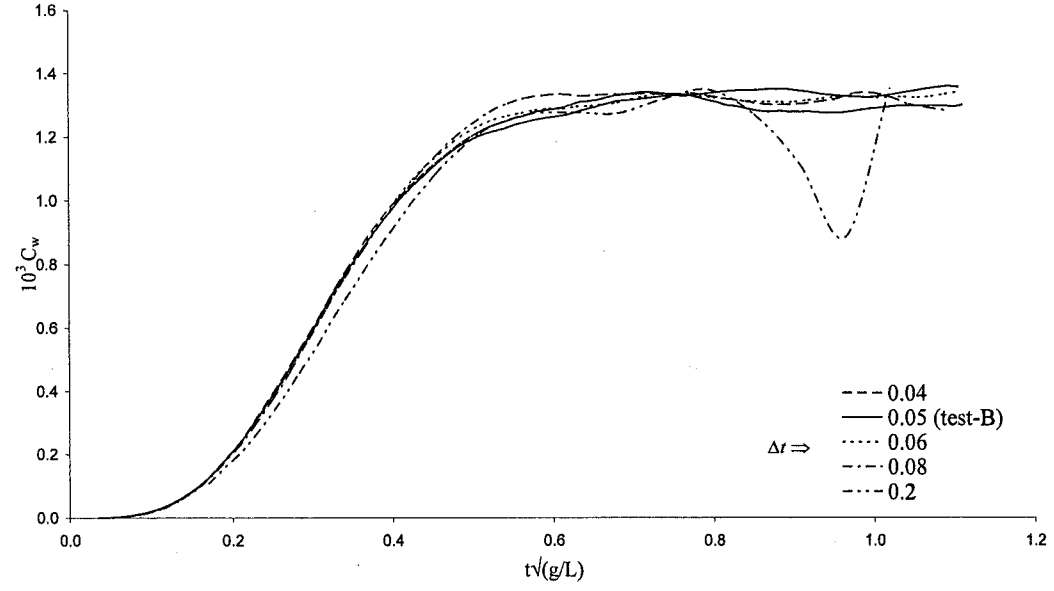

Figure 8.21: Time history of the wave resistance coefficient for varying time-step size - $F_n = 0.316$.

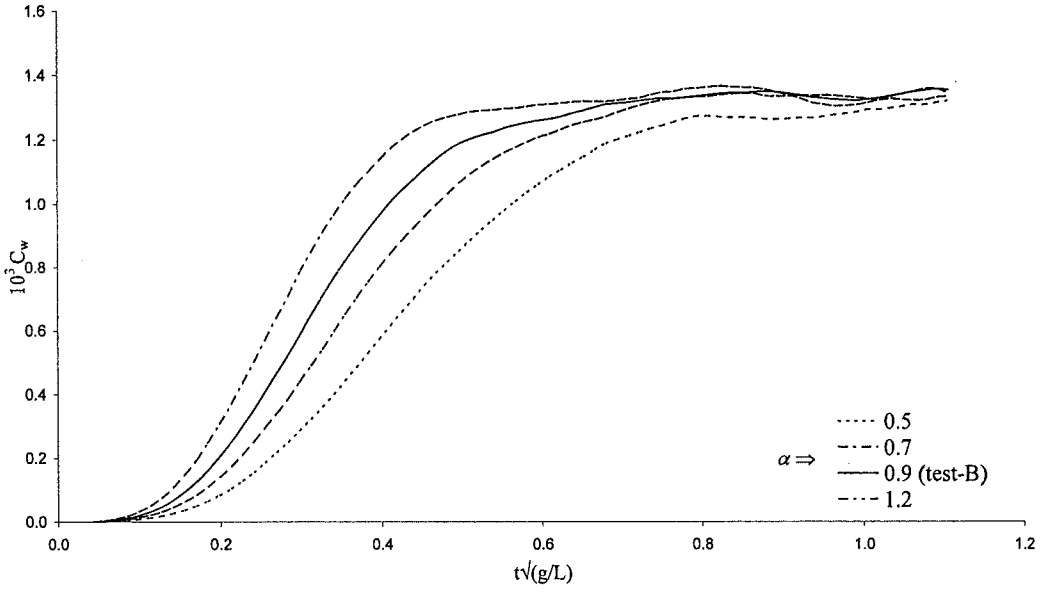

Figure 8.22: Time history of the wave resistance coefficient for varying hull acceleration parameter - $F_n = 0.316$.

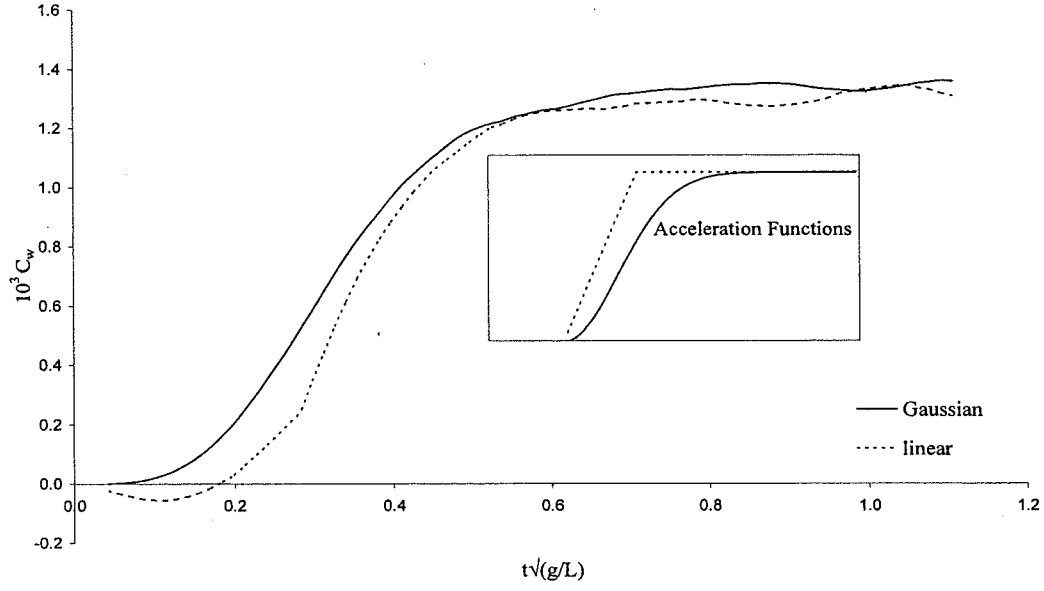

Figure 8.23: Time history of the wave resistance coefficient for different hull acceleration functions - $F_n = 0.316$.

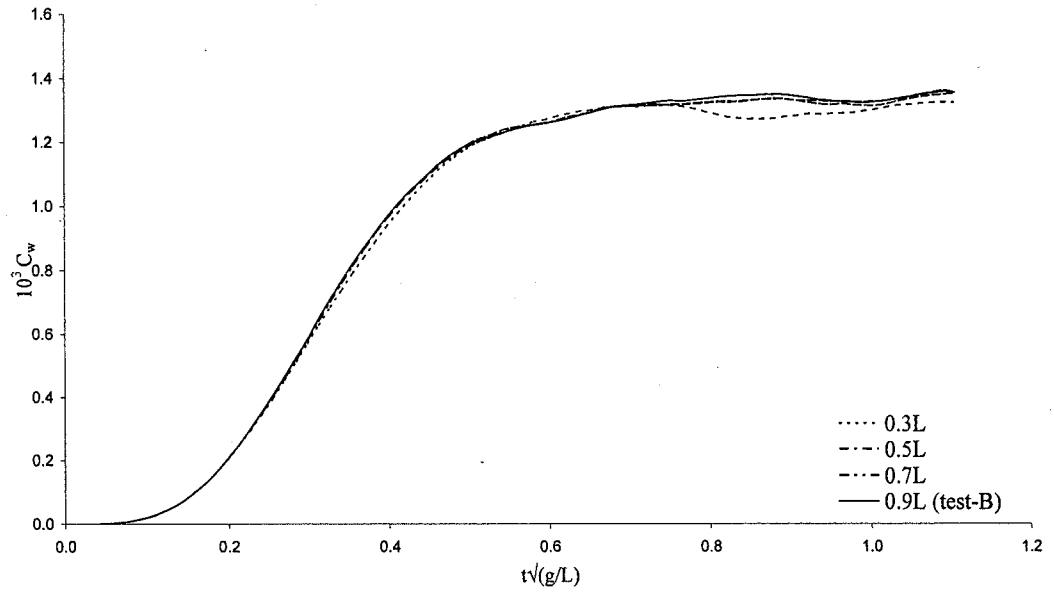

Figure 8.24: Time history of the wave resistance coefficient for varying side boundary position - $F_n = 0.316$.

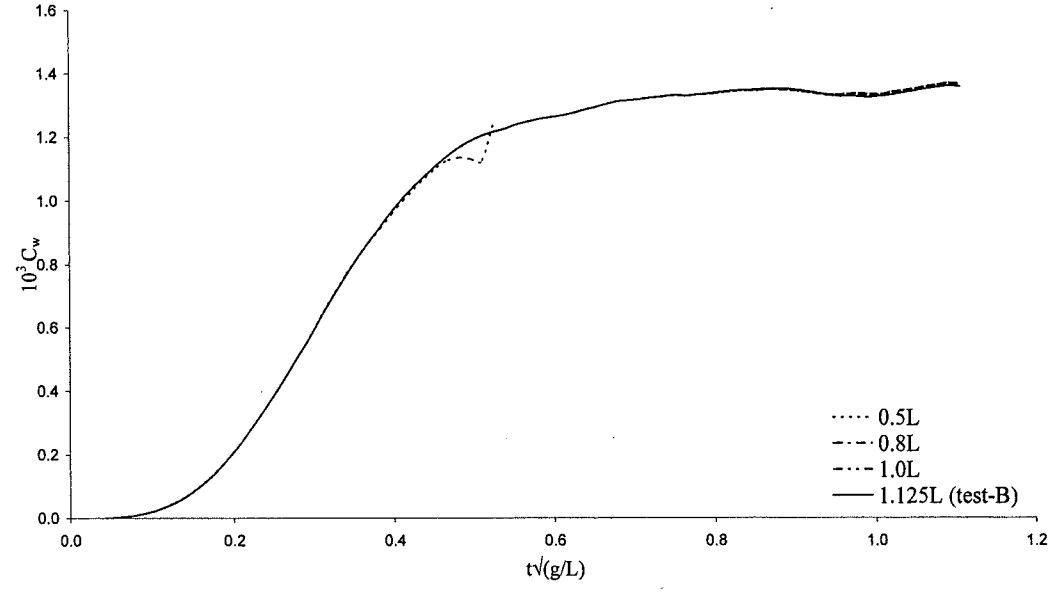

Figure 8.25: Time history of the wave resistance coefficient for varying downstream boundary position - $F_n = 0.316$.

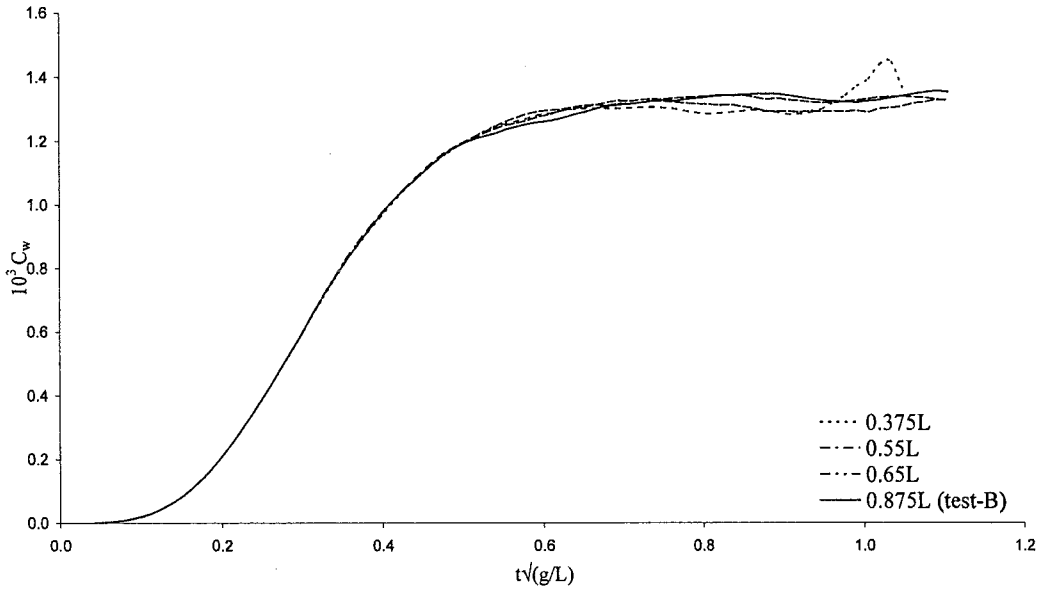

Figure 8.26: Time history of the wave resistance coefficient for varying upstream boundary position - $F_n = 0.316$.

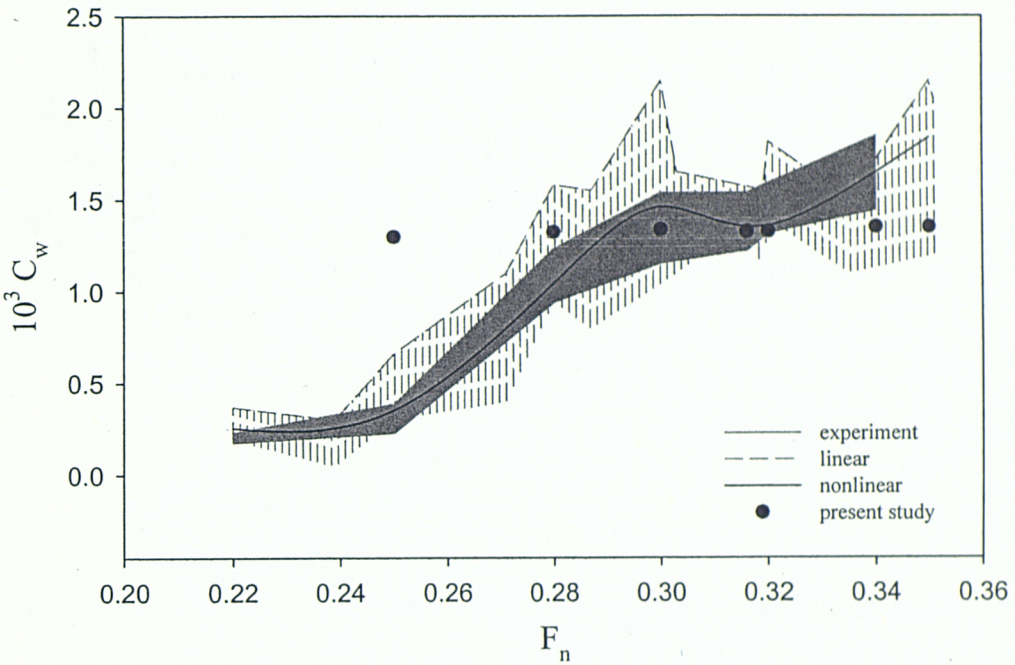

Figure 8.27: Comparison of computed and measured wave resistance coefficients for Series 60 hull with $C_B = 0.60$.

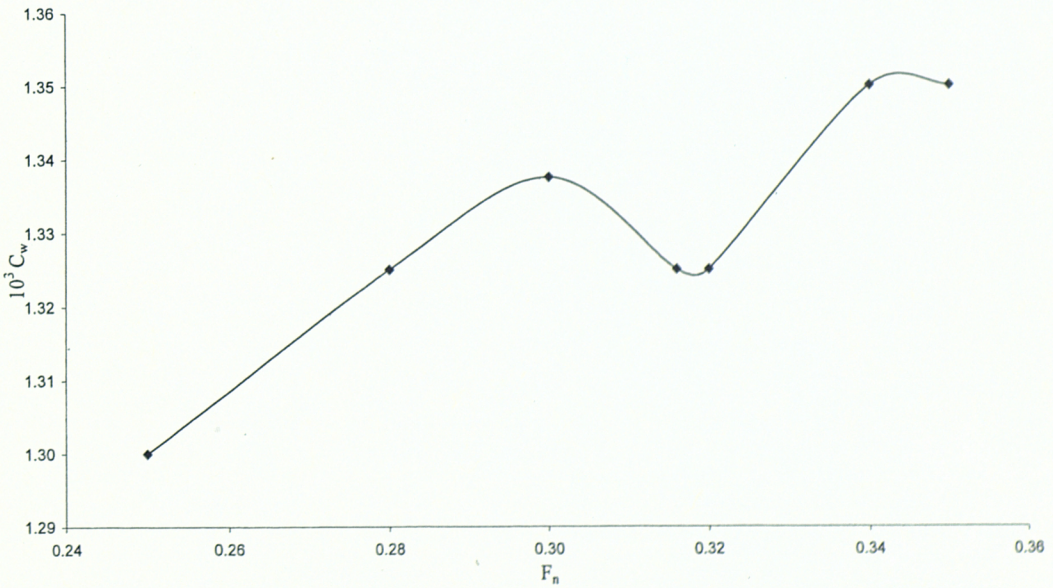

Figure 8.28: Wave resistance predictions for the Series 60 hull - $C_B = 0.60$.

8.6 Data Smoothing

All of the results presented up to now are obtained without using any kind of digital filtering or artificial damping. The numerical algorithm that is implemented to simulate fluid flow around two- and three-dimensional geometries does not incorporate such schemes to eliminate the oscillatory behaviour observed in the results (see sections 7.5, 7.6, 7.7, 8.4 and 8.5).

Although this oscillatory behaviour affects the accuracy of the results to some extent, it does not pose a serious problem for the steady-state ship wave pattern computations presented in the preceding sections. On the other hand, for a successful extension of the present method to the unsteady flow problem, a remedy must be sought that deals with this numerical instability issue.

A simple and an effective way of dealing with this problem is to use a data smoothing filter such as

$$\phi_{f_i} = \sum_{j=-n_b}^{n_b} \frac{1}{2n_b+1} \phi_{i+j} \,. \tag{8.1}$$

Equation 8.1 (see, for example, Press et al. (1986)) replaces each ϕ_i by a linear combination ϕ_{f_i} of itself and some number of nearby data points. ϕ_{f_i} corresponds to the filtered velocity potential on the free surface and n_b is the number of points used to the left and right of the original velocity potential value ϕ_i.

The smoothing procedure is first applied to the case shown previously in figure 8.7. As can easily be seen from the figure, there are some oscillations present in the results when the free surface desingularisation distance is set to 0.1. When the data smoothing method is applied to this particular case, the oscillations are damped almost completely

as shown in figure 8.29. n_b is set to 1, 2 and 4 in order to obtain the results plotted in figure 8.29.

Figure 8.29 proves that the data smoothing procedure works successfully. However, those results are just for two control points on the free surface. In order to illustrate the effect of the smoothing procedure on the global flow simulation, the wave-making resistance predictions that correspond to this particular case are plotted in figure 8.30. It is clear that the smoothing procedure decreases the oscillations present in the results without introducing excessive numerical damping which could affect the accuracy of the predictions.

To further investigate the capabilities of the data smoothing procedure, equation 8.1 is applied to a case where the oscillations are more severe. The original unfiltered results for this case are shown in figures 8.6 and 8.19. The oscillations in figure 8.6 for $d_h = 0.003$ are so large that the corresponding wave resistance coefficient computations (see figure 8.19) failed to produce an acceptable result for this desingularisation distance. However, when the data smoothing procedure is applied, the large oscillations observed in the results for individual free surface control points are damped out (see figure 8.31) and consequently wave resistance predictions yield acceptable results as shown in figure 8.32.

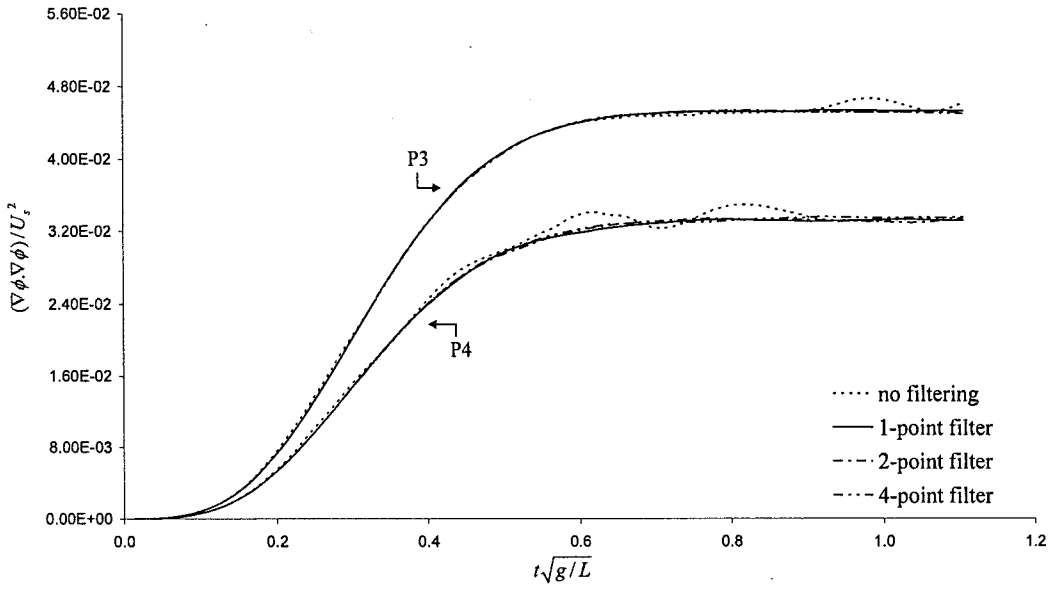

Figure 8.29: The effect of the data smoothing procedure on individual control points - $d_{fs} = 0.1$.

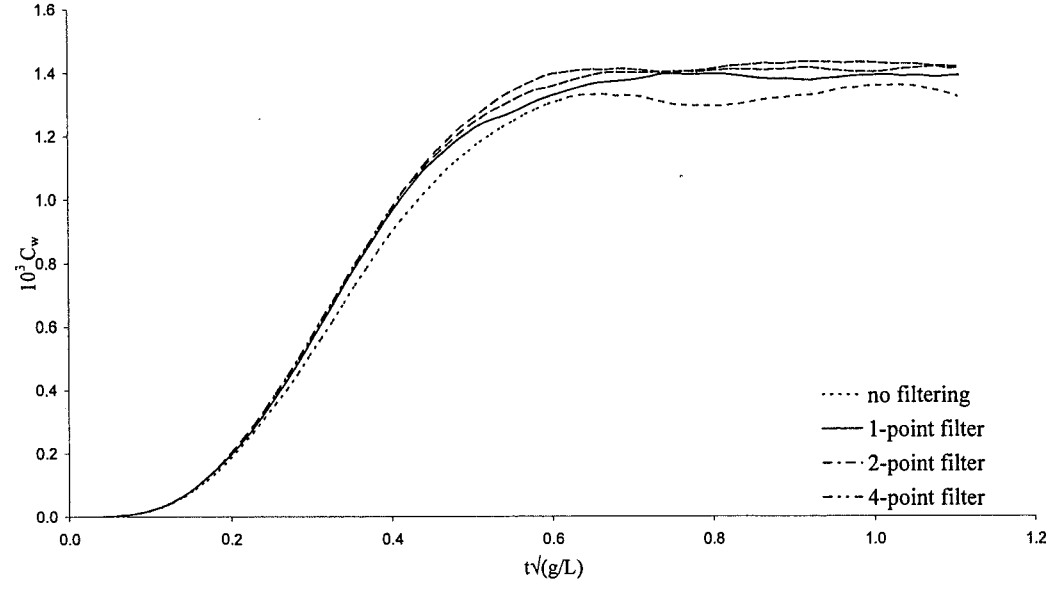

Figure 8.30: The effect of the data smoothing procedure on the wave resistance coefficient predictions - $d_{fs} = 0.1$.

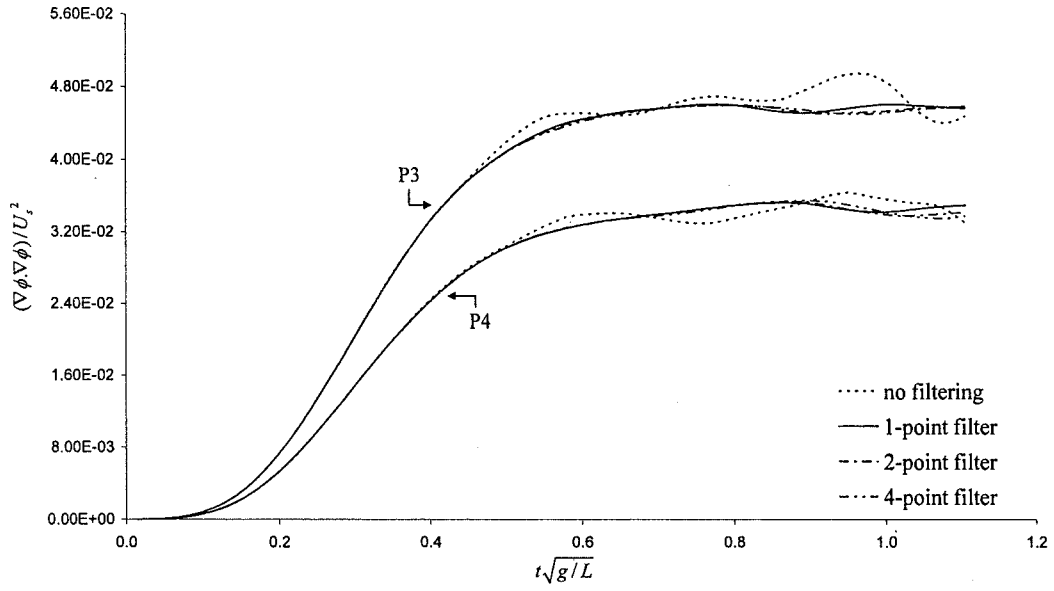

Figure 8.31: The effect of the data smoothing procedure on individual control points - $d_h = 0.003$.

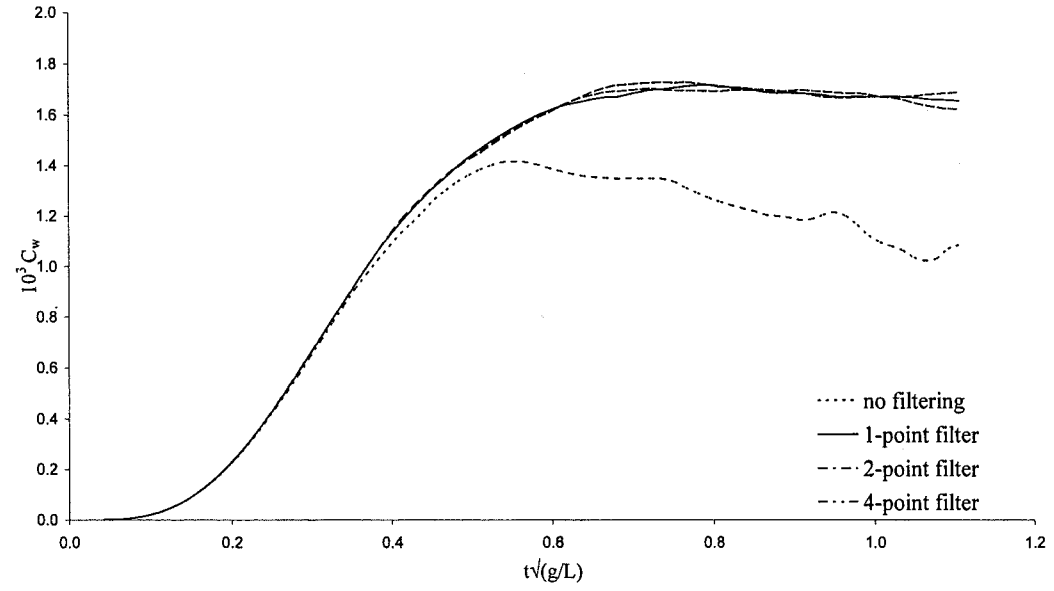

Figure 8.32: The effect of the data smoothing procedure on the wave resistance coefficient predictions - $d_h = 0.003$.

9. CONCLUSIONS AND FUTURE WORK

A general time-domain method is introduced in order to solve the nonlinear steady flow around submerged and surface-piercing bodies. Once the mathematical model that represents the physical problem is established in chapter 3, a numerical algorithm is developed based on a singularity-distribution method (chapter 4). Desingularised Rankine point sources are chosen as the fundamental singularities after a careful review of the related literature (see chapter 2).

The desingularised Rankine source method is first adopted, in chapter 6, for the simulation of the two-dimensional flow around a submerged cylinder. After that, it is extended to the solution of the nonlinear free surface flow past a Wigley hull advancing with constant forward velocity in calm water (chapter 7). In chapter 5, a hull discretisation study is undertaken for the mathematical representation of realistic hull forms. The resulting discretisation algorithm is incorporated into the main algorithm and computations are performed for a Series 60 hull (see chapter 8).

The desingularised approach results in robust and fast computation of the influence matrix and the use of point sources reduces the computational effort considerably since the necessity to evaluate surface integrals is eliminated. The source-only formulation leads to an additional simplicity in the numerical algorithm by aiding in the direct evaluation of the derivatives of the velocity potential.

While the stability of the numerical scheme depends mostly on the integration of the free surface boundary conditions (i.e. the Lagrange phase), the solution of the initial-boundary value problem (i.e. the Euler phase) takes up to sixty percent of the overall CPU time. The storage requirements are also dominated by the Euler phase. Although this is an expected outcome of a nonlinear time-domain formulation, it might be possible to reduce the computational time, albeit not the storage requirements, by using

a more efficient solver than the one currently adopted for the solution of the system of linear equations. For instance, an iterative solver, ideally one that employs preconditioning (see, for example, Payer and Mang (1997), Saad and Schultz (1986)), can be incorporated into the present algorithm without any major difficulty.

Another alternative to reduce the computational time is to prescribe the movements of the free surface nodes which has already been implemented in the present study. The intention in prescribing the movements of the free surface nodes is to eliminate the need to discretise the free surface at every time step, thereby reducing the required CPU time. It is decided that a suitable approach to achieve this goal is to fix the free surface nodes on the xy plane and allow them to move in the vertical direction with wave elevation. This procedure has not been applied for the simulation of the fluid flow around three-dimensional geometries with forward motion before. Constraining the horizontal movements of the free surface nodes gave rise to a computationally less intensive numerical algorithm and helped to lower the computational time considerably which is the most cumbersome aspect of a time-domain formulation. For instance, in a recent study by Sung and Grilli (2005) the fluid flow around a Wigley hull at a Froude number of 0.25 is computed using a Rankine panel method in 100 hours of CPU time on a PC with a Pentium 4 processor. Whereas for the present numerical algorithm the required computational time is much lower than this value even for a realistic hull form such as the Series 60. For example, just over an hour of CPU time is spent in order to obtain the time history for the finest mesh presented in figure 8.12.

It is not easy to find in the literature a complete analysis of the effects of variations in numerical parameters on the accuracy of the solution other than the mesh size. In this study, a detailed sensitivity analysis is undertaken to investigate the effects of the numerical parameters, which do not appear in the mathematical formulation but exist in the numerical algorithm due to the discrete representation of the mathematical model.

Using a time-domain formulation just for solving the ship wave resistance problem may at first seem unnecessarily expensive and inefficient. However, as discussed previously in chapters 1 and 2, the main objectives here were to simulate the transient development of the flow characteristics due to the interaction of fluid and structure and to establish a unified method in order to solve the ship wave resistance problem which then can be extended, through proper adjustments, for the solution of the unsteady flow problem in a future study.

To further this study, one can either modify the numerical algorithm to increase the computational efficiency (e.g. by using a more efficient solver for the system of linear equations) or can solve the unsteady problem directly without any major modifications. However, the most sound approach will be to solve the unsteady problem once it is made clear, by extensive numerical tests and carrying out any necessary changes in the formulation, that the numerical scheme is efficient and stable enough to be adapted for the seakeeping problem (see, for example, Beck et al. (1996), Ohkusu (1998) for investigations into verification and validation of numerical hydrodynamics algorithms). Any form of numerical instability observed in the steady flow problem may magnify due to the unsteady nature of the seakeeping problem.

For an unsteady flow simulation, first of all, a wave system must be introduced into the computational domain. In a nonlinear flow simulation, where the steady and unsteady flow cannot be uncoupled, the incident wave field should also be fully nonlinear. However, in many numerical codes higher order Stokes' waves are used to simplify the process (e.g. Koo and Kim (2004)).

In a time-domain formulation the steady flow solution can be used to obtain the initial conditions for the unsteady phase (see, for example, Ferrant (1996)). Likewise the incident wave field can be used to impose the upstream boundary condition, i.e. the incident wave model may be utilised to prescribe the velocity potential and wave

elevation at the upstream boundary. In this manner the wave system can easily be introduced into the computational domain.

Just as in a wave tank, a numerical wave-maker may be installed at the upstream boundary to generate appropriate wave records (see, for example, Maskew (1992)). Scorpio et al. (1996), on the other hand, implemented a method that preprocesses the incident wave system in a two-dimensional wave tank. The wave records obtained from this two-dimensional wave tank are then used in the main three-dimensional computational domain where the unsteady computations are performed. A similar approach is to generate wave records that correspond to a given sea spectrum (see Diken (1999)) independent of the computation of the fluid/structure interaction.

The current numerical algorithm already incorporates separate grid generation routines for the body and the free surface. If desired, different types of prescribed velocity schemes may be used in the free surface boundary conditions with the cost of an increase in CPU time. Therefore, another recommendation to further this study is to implement several prescribed velocity schemes and analyse the effects of these different schemes in detail.

As quoted in ITTC (2005) "*The Rankine panel method is versatile in that it can deal with different kinds of free surface conditions that may include nonlinear terms. However, this method is generally time-consuming and hence unlikely to be routinely used at least in the near future by industry*". Nevertheless, the current study can be seen as a step towards establishing a practical design tool by means of a Rankine source method. Undoubtedly, the ultimate role of numerical hydrodynamics, and in a sense of this study, should be to replace traditional model tests. Yet, current computational power and the accuracy obtained does not (and probably will not in the near future) allow this to happen. The results presented here are generally in good qualitative agreement with the experimental measurements for the Wigley hull; however, the discrepancies with the measurements are larger for the Series 60 hull. As mentioned in

the introduction, tank-testing is a costly process and the overall cost obviously increases when testing is repeated several times as a result of the hull form optimisation process. The present study might at least be useful to reduce the number of iterations that are required to reach the final hull form. In other words, it can be used to optimise a design before model tests are performed, allow a naval architect to explore new hull shapes in a comparative sense and help to visualise the changes in the flow characteristics due to hull form modifications. Then, just one or two tank-testing might be enough to decide on the final hull form.

BIBLIOGRAPHY

Aanesland, V. (1989). A hybrid model for calculating wave-making resistance. In *Proceedings of the 5th International Conference on Numerical Ship Hydrodynamics*, Hiroshima, Japan, 657-666.

Acheson, D. J. (2000). Elementary Fluid Dynamics. *Oxford University Press.*

Anderson, J. D. (1991). Fundamentals of Aerodynamics, second edition. *McGraw-Hill, Inc.*

Baar, J. J. M. (1987). A Three-Dimensional Linear Analysis of Steady Ship Motion in Deep Water. *PhD Thesis*, Brunel University, Uxbridge.

Baar, J. J. M. and Price, W. G. (1988). Developments in the calculation of the wavemaking resistance of ships. *Proceedings of the Royal Society of London*, A. 416:115-147.

Bartels, R. H., Beatty, J. C. and Barsky, B. A. (1986). An Introduction to Splines for Use in Computer Graphics and Geometric Modeling. *Morgan Kauffman Publishers.*

Beck, R. F., Cao, Y. and Lee, T. H. (1993). Fully nonlinear water wave computations using the desingularized method. In *Proceedings of the 6th International Conference on Numerical Ship Hydrodynamics*, Iowa City, USA, 3-20.

Beck, R. F., Cao, Y., Scorpio, S. and Schultz, W. (1994). Nonlinear ship motion computations using the desingularized method. In *Proceedings of the 20th Symposium on Naval Hydrodynamics*, Santa Barbara, California, USA, 227-247.

Beck, R. F. and Reed, A. M. (2000). Modern seakeeping computations for ships. In *Proceedings of the 23rd Symposium on Naval Hydrodynamics*, Val de Reuil, France, 1-45.

Beck, R. F., Reed, A. M. and Rood, E. P. (1996). Application of modern numerical methods in marine hydrodynamics. *Trans. SNAME*, 104:519-537.

Bertram, V. (2000). Practical Ship Hydrodynamics. *Butterworth-Heinemann.*

Brizzolara, S., Bruzzone, D., Cassella, P., Scamardella, A. and Zotti, I. (1998). Wave resistance and wave patterns for high-speed crafts; validation of numerical results by model test. In *Proceedings of the 22nd Symposium on Naval Hydrodynamics*, Washington D.C., USA, 69-83.

Buchmann, B. (2001). Theory and applications in stability of free-surface time-domain boundary element models. *International Journal for Numerical Methods in Fluids*, 37:321-339.

Bulgarelli, U. P., Lugni, C. and Landrini, M. (2003). Numerical modelling of free-surface flows in ship hydrodynamics. *International Journal for Numerical Methods in Fluids*, 43:465-481.

Cao, Y., Schultz, W. and Beck, R. F. (1991). Three-dimensional desingularized boundary integral methods for potential problems. *International Journal for Numerical Methods in Fluids*, 12:785-803.

Celebi, M. S. (2000). Computation of transient nonlinear ship waves using an adaptive algorithm. *Journal of Fluids and Structures*, 14:281-301.

Celebi, M. S. and Beck, R. F. (1997). Geometric modeling for fully nonlinear ship-wave interactions. *Journal of Ship Research*, 41(1):17-25.

Chen, C. Y. and Noblesse, F. (1983). Comparison between theoretical predictions of wave resistance and experimental data for the Wigley hull. *Journal of Ship Research*, 27(4):215-226.

Cheng, B. H. (1989). Computations of 3D transom stern flows. In *Proceedings of the 5th International Conference on Numerical Ship Hydrodynamics*, Hiroshima, Japan, 581-591.

Dawson, C. W. (1977). A practical computer method for solving ship-wave problems. In *Proceedings of the 2nd International Conference on Numerical Ship Hydrodynamics*, Berkeley, USA, 30-38.

Diken, Ö. (1999). Rasgele Dalgaların Hızlı Fourier Transformu ile Üretilmesi (Spectral Analysis by Fast Fourier Transform). *Final Year Project (In Turkish)*, Faculty of Naval Architecture and Ocean Engineering, Technical University of Istanbul.

Diken, Ö., Du, S. X., Hudson, D. A. and Temarel, P. (2004). Calculation of steady-state ship wave patterns using a general Rankine source method. In *Proceedings of the 14th International Offshore and Polar Engineering Conference*, Toulon, France, 447-454.

Dommermuth, D., Innis, G., Luth, T., Novikov, E., Schlageter, E. and Talcott, J. (1998). Numerical simulation of bow waves. In *Proceedings of the 22nd Symposium on Naval Hydrodynamics*, Washington D.C., USA, 508-521.

Eggers, K. (1981). Non-Kelvin dispersive waves around non-slender ships. *Schiffstechnik*, Bd. 28.

Eggers, K., Sharma, S. D. and Ward, L. W. (1967). An assessment of some experimental methods for determining the wavemaking characteristics of a ship form. *Trans. SNAME*, 75:112-157.

Faltinsen, O. M. and Zhao, R. (1991). Numerical predictions of ship motions at high forward speed. *Philosophical Transactions of the Royal Society of London*, A. 334:241-252.

Ferrant, P. (1996). Simulation of strongly nonlinear wave generation and wave-body interactions using a 3-D MEL model. In *Proceedings of the 21st Symposium on Naval Hydrodynamics*, Trondheim, Norway, 93-109.

Ferziger, J. H. and Peric, M. (2002). Computational Methods for Fluid Dynamics, third edition. *Springer.*

Froude, W. (1868). Observations and suggestions on the subject of determining by experiment the resistance of ships. *Memo. to E. J. Reed, Chief Constructor of the Navy.*

Gadd, G. E. (1968). On understanding ship resistance mathematically. *Journal of the Institute of Mathematics and its Applications*, 4:43-57.

Gadd, G. E. (1976). A method for computing the flow and surface wave pattern around full forms. *Trans. RINA*, 118:207-216.

Gerritsma, J. and Beukelman, W. (1967). Analysis of the modified strip theory for the calculation of ship motions and wave bending moments. *International Shipbuilding Progress*, 14:319-337.

Greenberg, M. D. (1998). Advanced Engineering Mathematics, second edition. *Prentice Hall.*

Guilloton, R. (1951). Potential theory of wave resistance of ships with tables for its calculation. *Trans. SNAME*, 59:86-128.

Havelock, T. H. (1925). Studies in wave resistance: the effect of parallel middle body. *Proceedings of the Royal Society of London*, A. 108:77-92.

Havelock, T. H. (1932). The theory of wave resistance. *Proceedings of the Royal Society of London*, A. 138:339-348.

Havelock, T. H. (1934). Wave patterns and wave resistance. *Trans. INA*, 76:430-446.

Hess, J. L. and Smith, A. M. O. (1964). Calculation of non-lifting potential flow about arbitrary three-dimensional bodies. *Journal of Ship Research*, 8(2):22-44.

Hsin, C. Y. and Chou, S. K. (1998). Applications of a hybrid boundary element method to the analysis of free-surface flow around lifting and nonlifting bodies. In *Proceedings of the 22nd Symposium on Naval Hydrodynamics*, Washington D.C., USA, 848-859.

Huang, Y. (1997). Nonlinear Ship Motions by a Rankine Panel Method. *PhD Thesis*, Department of Ocean Engineering, Massachusetts Institute of Technology.

Huang, Y. and Sclavounos, P. D. (1998). Nonlinear ship motions. *Journal of Ship Research*, 42(2):120-130.

Inui, T. (1962). Wave-making resistance of ships. *Trans. SNAME*, 70:283-353.

ITTC (2005). Final Report and Recommendations of the Seakeeping Committee. *Proceedings of the 24th International Towing Tank Conference*, volume I, Edinburgh, Scotland, UK.

Janson, C. E. (2000). Linear and non-linear potential-flow calculations of free-surface waves with lift and induced drag. *Proceedings of the Institution of Mechanical Engineers Part C*, 214:801-812.

Janson, C. E. and Larsson, L. (1996). A method for the optimization of ship hulls from a resistance point of view. In *Proceedings of the 21st Symposium on Naval Hydrodynamics*, Trondheim, Norway, 680-696.

Jensen, G., Bertram, V. and Soding, H. (1989). Ship wave-resistance computations. In *Proceedings of the 5th International Conference on Numerical Ship Hydrodynamics*, Hiroshima, Japan, 593-606.

Jensen, G., Mi, Z. X. and Soding, H. (1986). Rankine source methods for numerical solutions of the steady wave resistance problem. In *Proceedings of the 16th Symposium on Naval Hydrodynamics*, Berkeley, USA, 575-582.

Kang, C. G. and Gong, I. Y. (1990). A numerical solution method for three-dimensional nonlinear free surface problems. In *Proceedings of the 18th Symposium on Naval Hydrodynamics*, Ann Arbor, Michigan, USA, 427-438.

Kara, F. and Vassalos, D. (2005). Time domain computation of the wave-making resistance of ships. *Journal of Ship Research*, 49(2):144-158.

Kelvin, Lord (Sir W. Thomson) (1887). On ship waves. *Proceedings of the Institution of Mechanical Engineers*, 3:409-434.

Kim, Y. H. and Jenkins, D. (1981). Trim and sinkage effects on wave resistance with Series 60, $C_B = 0.60$. *DTNSRDC Report*, SPD-1013-01.

Kim, Y. H. and Lucas, T. (1990). Nonlinear ship waves. In *Proceedings of the 18th Symposium on Naval Hydrodynamics*, Ann Arbor, Michigan, USA, 439-452.

Koo, W. and Kim, M. H. (2004). Freely floating-body simulation by a 2D fully nonlinear numerical wave tank. *Ocean Engineering*, 31:2011-2046.

Korvin-Kroukovsky, B. V. (1955). Investigation of ship motions in regular waves. *Trans. SNAME*, 63:386-435.

Korvin-Kroukovsky, B. V. and Jacobs, W. R. (1957). Pitching and heaving motions of a ship in regular waves. *Trans. SNAME*, 65:590-632.

Kring, D. C. (1994). Time Domain Ship Motions by a Three-Dimensional Rankine Panel Method. *PhD Thesis*, Department of Ocean Engineering, Massachusetts Institute of Technology.

Kring, D. C., Huang, Y., Sclavounos, P. D., Vada, T. and Braathen, A. (1996). Nonlinear ship motions and wave-induced loads by a Rankine method. In *Proceedings of the 21st Symposium on Naval Hydrodynamics*, Trondheim, Norway, 45-63.

Kring, D. C. and Sclavounos, P. D. (1991). A new method for analyzing the seakeeping of multi-hull ships. In *FAST'91: Proceedings of the 1st International Conference on Fast Sea Transportation*, Norway, 429-444.

Lalli, F. (1997). On the accuracy of the desingularized boundary integral method in free surface flow problems. *International Journal for Numerical Methods in Fluids*, 25:1163-1184.

Larsson, L., Broberg, L., Kim, K. J. and Zhang, D. H. (1989). New viscous and inviscid CFD techniques for ship flows. In *Proceedings of the 5th International Conference on Numerical Ship Hydrodynamics*, Hiroshima, Japan, 185-210.

Larsson, L., Regnstrom, B., Broberg, L., Li, D. Q. and Janson, C. E. (1998). Failures, fantasies, and feats in the theoretical/numerical prediction of ship performance. In *Proceedings of the 22nd Symposium on Naval Hydrodynamics*, Washington D.C., USA, 11-32.

Lewis, E. V., Ed. (1988). Principles of Naval Architecture. Volume II: Resistance, Propulsion and Vibration, *Society of Naval Architects and Marine Engineers*, Jersey City, New Jersey.

Lin, W. C. and Yue, D. K. P. (1990). Numerical solutions for large amplitude ship motions in the time domain. In *Proceedings of the 18th Symposium on Naval Hydrodynamics*, Ann Arbor, Michigan, USA, 41-66.

Liu, Y., Xue, M. and Yue, D. K. P. (2001). Computations of fully nonlinear three-dimensional wave-wave and wave-body interactions. Part 2. Nonlinear waves and forces on a body. *Journal of Fluid Mechanics*, 438:41-66.

Lloyd, A. R. J. M. (1998). Seakeeping: Ship Behaviour in Rough Weather, revised edition, *ARJM Lloyd*, Hampshire, United Kingdom.

Longo, J. and Stern, F. (1996). Technical note: evaluation of surface-ship resistance and propulsion model-scale database for CFD validation. *Journal of Ship Research*, 40(2):112-116.

Longo, J., Stern, F. and Toda, Y. (1993). Mean-flow measurements in the boundary layer and wake and wave field of a Series 60 $C_B = 0.6$ ship model – part 2: scale effects on near-field wave patterns and comparisons with inviscid theory. *Journal of Ship Research*, 37(1):16-24.

Longuet-Higgins, M. S. and Cokelet, E. D. (1976). The deformation of steep surface waves on water I. a numerical method of computation. *Proceedings of the Royal Society of London*, A. 350:1-26.

Lunde, J. K. (1951). On the linearized theory of wave resistance for displacement ships in steady and accelerated motion. *Trans. SNAME*, 59:25-85.

Marr, G. and Jackson, P. S. (1999). Some improvements and comparisons in the solution of the Neumann-Kelvin problem. *Journal of Ship Research*, 43(3):170-179.

Maruo, H. and Ogiwara, S. (1985). A method of computation for steady ship-waves with non-linear free surface conditions. In *Proceedings of the 4th International Conference on Numerical Ship Hydrodynamics*, Washington, USA, 218-233.

Maskew, B. (1992). Prediction of nonlinear wave/hull interactions on complex vessels. In *Proceedings of the 19th Symposium on Naval Hydrodynamics*, Seoul, South Korea, 1-20.

McCormick, B. W. (1979). Aerodynamics, Aeronautics, and Flight Mechanics. *John Wiley & Sons, Inc.*

Michell, J. H. (1898). The wave resistance of a ship. *Philosophical Magazine*, 5(45):106-123.

Miyata, H. (1996). Time-marching CFD simulation for moving boundary problems. In *Proceedings of the 21st Symposium on Naval Hydrodynamics*, Trondheim, Norway, 291-311.

Musker, A. J. (1988). A panel method for predicting ship wave resistance. In *Proceedings of the 17th Symposium on Naval Hydrodynamics*, The Hague, Netherlands.

Musker, A. J. (1989). Stability and accuracy of a non-linear model for the wave resistance problem. In *Proceedings of the 5th International Conference on Numerical Ship Hydrodynamics*, Hiroshima, Japan, 629-642.

Nakos, D. E. (1990). Ship Wave Patterns and Motions by a Three Dimensional Rankine Panel Method. *PhD Thesis*, Department of Ocean Engineering, Massachusetts Institute of Technology.

Nakos, D. E. and Sclavounos, P. D. (1990a). On steady and unsteady ship wave patterns. *Journal of Fluid Mechanics*, 215:263-288.

Nakos, D. E. and Sclavounos, P. D. (1990b). Ship motions by a three-dimensional Rankine panel method. In *Proceedings of the 18th Symposium on Naval Hydrodynamics*, Ann Arbor, Michigan, USA, 21-40.

Nakos, D. E. and Sclavounos, P. D. (1994). Kelvin wakes and wave resistance of cruiser- and transom-stern ships. *Journal of Ship Research*, 38(1):9-29.

Newman, J. N. (1976). Linearized wave resistance theory. In *Proceedings of the International Seminar on Wave Resistance*, Tokyo, Japan, 31-43.

Noblesse, F. (1981). Alternative integral representations for the Green function of the theory of ship wave resistance. *Journal of Engineering Mathematics*, 15(4):241-265.

Noblesse, F. (1983). A slender-ship theory of wave resistance. *Journal of Ship Research*, 27(1):13-33.

Noblesse, F. and McCarthy, J. H. (1983). Ship wave-resistance computations. In *Proceedings of the 2nd DTNSRDC Workshop.*

Norrbin, N. H., Ed. (1984). *Proceedings of the 17th International Towing Tank Conference*, Goteborg, Sweden.

Ogilvie, T. F. (1977). Singular-perturbation problems in ship hydrodynamics. *Advances in Applied Mechanics*, 17:91-188.

Ohkusu, M. (1998). Validation of theoretical methods for ship motions by means of experiment. In *Proceedings of the 22nd Symposium on Naval Hydrodynamics*, Washington D.C., USA, 341-358.

Pawlowski, J. (1992). A nonlinear theory of ship motion in waves. In *Proceedings of the 19th Symposium on Naval Hydrodynamics*, Seoul, South Korea, 33-58.

Payer, H. J. and Mang, H. A. (1997). Iterative strategies for solving systems of linear, algebraic equations arising in 3D BE-FE analyses of tunnel drivings. *Numerical Linear Algebra with Applications*, 4(3):239-268.

Peters, A. S. and Stoker, J. J. (1957). The motion of a ship, as a floating rigid body, in a seaway. *Communications on Pure and Applied Mathematics*, 10:399-490.

Press, W. H., Flannery, B. P., Teukolsky, S. A. and Vetterling, W. T. (1986). Numerical Recipes. *Cambridge University Press.*

Raven, H. C. (1990). Adequacy of free-surface conditions for the wave-resistance problem. In *Proceedings of the 18th Symposium on Naval Hydrodynamics*, Ann Arbor, Michigan, USA, 375-395.

Raven, H. C. (1992). A practical nonlinear method for calculating ship wavemaking and wave resistance. In *Proceedings of the 19th Symposium on Naval Hydrodynamics*, Seoul, South Korea.

Raven, H. C. (1993). Nonlinear ship wave calculations using the RAPID method. In *Proceedings of the 6th International Conference on Numerical Ship Hydrodynamics*, Iowa City, USA, 95-118.

Raven, H. C. (1996). A Solution Method for the Nonlinear Ship Wave Resistance Problem. *Doctor's Thesis*, Delft University of Technology, Delft, Netherlands.

Raven, H. C. (1998). Inviscid calculations of ship wave making – capabilities, limitations, and prospects. In *Proceedings of the 22nd Symposium on Naval Hydrodynamics*, Washington D.C., USA, 738-754.

Raven, H. C. and Prins, H. J. (1998). Wave pattern analysis applied to nonlinear ship wave calculations. In *Proceedings of the 13th International Workshop on Water Waves and Floating Bodies*, Alphen aan den Rijn, Netherlands.

Reed, A. M., Telste, J. G. and Scragg, C. (1990). Analysis of transom stern flows. In *Proceedings of the 18th Symposium on Naval Hydrodynamics*, Ann Arbor, Michigan, USA, 207-219.

Rogers, F. D. and Adams, J. A. (1990). Mathematical Elements for Computer Graphics, second edition. *McGraw-Hill, Inc.*

Saad, Y. and Schultz, M. H. (1986). GMRES: A generalized minimal residual algorithm for solving nonsymmetric linear systems. *SIAM Journal on Scientific and Statistical Computing*, 7(3):856-869.

Salvesen, N., Tuck, E. O. and Faltinsen, O. M. (1970). Ship motions and sea loads. *Trans. SNAME*, 78:250-287.

Scorpio, S. (1997). Fully Nonlinear Ship-Wave Computations Using a Multipole Accelerated Desingularized Method. *PhD Thesis*, Department of Naval Architecture and Marine Engineering, University of Michigan.

Scorpio, S., Beck, R. F. and Korsmeyer, F. (1996). Nonlinear water wave computations using a multipole accelerated, desingularized method. In *Proceedings of the 21st Symposium on Naval Hydrodynamics*, Trondheim, Norway, 64-74.

Stern, F., Longo, J., Zhang, Z. J. and Subramani, A. K. (1996). Detailed bow-flow data and CFD for a Series 60 $C_B = 0.6$ ship model for Froude number 0.316. *Journal of Ship Research*, 40(3):193-199.

Subramani, A. K., Beck, R. F. and Scorpio, S. (1998). Fully nonlinear free-surface computations for arbitrary and complex hull forms. In *Proceedings of the 22nd Symposium on Naval Hydrodynamics*, Washington D.C., USA, 390-402.

Subramani, A. K., Paterson, E. G. and Stern, F. (2000). CFD calculation of sinkage and trim. *Journal of Ship Research*, 44(1):59-82.

Sung, H. G. and Grilli, S. T. (2005). Numerical modeling of nonlinear surface waves caused by surface effect ships dynamics and kinematics. In *Proceedings of the 15th International Offshore and Polar Engineering Conference*, Seoul, Korea, 124-131.

Takaki, M. and Iwashita, H. (2000). Comparative study on seakeeping computation methods of high speed vessels. In *the Fourth Osaka Colloquium on Seakeeping Performance of Ships*, Osaka, Japan, 79-88.

Telste, J. G. and Reed, A. M. (1993). Calculation of transom stern flows. In *Proceedings of the 6th International Conference on Numerical Ship Hydrodynamics*, Iowa City, USA, 79-92.

Toda, Y., Stern, F. and Longo, J. (1992). Mean-flow measurements in the boundary layer and wake and wave field of a Series 60 $C_B = 0.6$ ship model – part 1: Froude numbers 0.16 and 0.316. *Journal of Ship Research*, 36(4):360-377.

Todd, F. H. (1953). Some further experiments on single-screw merchant ship forms – Series 60. *Trans. SNAME*, 61:516-589.

Tuck, E. O. (1975). Low-aspect-ratio flat-ship theory. *Journal of Hydronautics*, 9(1):3-12.

van't Veer, R. V. (1997). Analysis of motions and loads on a catamaran vessel in waves. In *FAST'97: Proceedings of the 4th International Conference on Fast Sea Transportation*, Sydney, Australia, 439-446.

Wehausen, J. V. (1973). The wave resistance of ships. *Advances in Applied Mechanics*, 13:93-145.

Wigley, W. C. S. (1934). A comparison of experiment and calculated wave-profiles and wave-resistances for a form having parabolic waterlines. *Proceedings of the Royal Society of London*, A. 144:144-159.

Wyatt, D. C. (2000). Development and assessment of a nonlinear wave prediction methodology for surface vessels. *Journal of Ship Research*, 44(2):96-107.

Xue, M., Xu, H., Liu, Y. and Yue, D. K. P. (2001). Computations of fully nonlinear three-dimensional wave-wave and wave-body interactions. Part 1. Dynamics of steep three-dimensional waves. *Journal of Fluid Mechanics*, 438:11-39.

Yasukawa, H. (1989). Calculation of free-surface flow around a ship in shallow water by Rankine source method. In *Proceedings of the 5th International Conference on Numerical Ship Hydrodynamics*, Hiroshima, Japan, 643-655.

APPENDIX – CALCULATION OF STEADY-STATE SHIP WAVE PATTERNS USING A GENERAL RANKINE SOURCE METHOD

by Özgür Diken, Shuang-Xing Du, Dominic A. Hudson, Pandeli Temarel

Proceedings of the 14th International Offshore and Polar Engineering Conference, Toulon, France, May 2004.

The following published paper was included in the bound thesis. This has not been digitised due to copyright restrictions, but the reference is provided.

Diken Ö, Du S, Hudson D, Temarel P. (2004) Calculation of steady-state ship wave patterns using a general rankine source method. *Proceedings of the Fourteenth (2004) International Offshore and Polar Engineering Conference [serial online* - ISOPE 2004), pp 447-454.